

F201 924 (2)
AD-A279 406



PL-TR-93-2201

**TOMOGRAPHIC ANALYSIS OF THE THREE-DIMENSIONAL
VARIATION OF THE SEISMIC VELOCITY STRUCTURE OF THE
SHALLOW CRUST UNDERLYING SOUTHERN NEW ENGLAND**

**Allyn K. Bowers
Alan L. Kafka**

**Weston Observatory
Department of Geology and Geophysics
Boston College
Weston, MA 02193**

30 September 1993

**DTIC
ELECTE
APR 21 1994
S G D**

Scientific Report No. 3

Approved for public release; distribution unlimited



**PHILLIPS LABORATORY
Directorate of Geophysics
AIR FORCE MATERIEL COMMAND
HANSCOM AIR FORCE BASE, MA 01731-3010**


94-12141





94 4 20 158

The views and conclusions contained in this document are those of the authors and should not be interpreted as representing the official policies, either expressed or implied, of the Air Force or the U.S. Government.

This technical report has been reviewed and is approved for publication.


JAMES F. LEWKOWICZ
Contract Manager
Solid Earth Geophysics Branch
Earth Sciences Division


JAMES F. LEWKOWICZ
Branch Chief
Solid Earth Geophysics Branch
Earth Sciences Division


DONALD H. ECKHARDT, Director
Earth Sciences Division

This document has been reviewed by the ESD Public Affairs Office (PA) and is releasable to the National Technical Information Service (NTIS).

Qualified requestors may obtain additional copies from the Defense Technical Information Center. All others should apply to the National Technical Information Service.

If your address has changed, or if you wish to be removed from the mailing list, or if the addressee is no longer employed by your organization, please notify PL/IMA, 29 Randolph Road, Hanscom AFB MA 01731-3010. This will assist us in maintaining a current mailing list.

Do not return copies of this report unless contractual obligations or notices on a specific document require that it be returned.

REPORT DOCUMENTATION PAGE			Form Approved OMB No 0704-0188	
<small>Public reporting burden for this collection of information is estimated to average 1 hour per response, including the time for reviewing instructions, searching existing data sources, gathering and maintaining the data needed, and completing and reviewing the collection of information. Send comments regarding this burden estimate or any other aspect of this collection of information, including suggestions for reducing this burden, to Washington Headquarters Services, Directorate for Information Operations and Reports, 1215 Jefferson Davis Highway, Suite 1204, Arlington, VA 22202-4302, and to the Office of Management and Budget, Paperwork Reduction Project (0704-0188), Washington, DC 20503.</small>				
1. AGENCY USE ONLY (Leave blank)		2. REPORT DATE 30 September 1993		3. REPORT TYPE AND DATES COVERED Scientific No. 3
4. TITLE AND SUBTITLE Tomographic Analysis of the Three-Dimensional Variation of the Seismic Velocity Structure of the Shallow Crust Underlying Southern New England			5. FUNDING NUMBERS PE 62101F PR 7600 TA 09 WU AL Contract F19628-90-K-0035	
6. AUTHOR(S) A.K. Bowers and A.L. Kafka				
7. PERFORMING ORGANIZATION NAME(S) AND ADDRESS(ES) Weston Observatory Department of Geology and Geophysics Boston College Weston, MA 02193			8. PERFORMING ORGANIZATION REPORT NUMBER	
9. SPONSORING / MONITORING AGENCY NAME(S) AND ADDRESS(ES) Phillips Laboratory 29 Randolph Rd. Hanscom AFB, MA 01731-3010 Contract Manager: James Lewkowicz/GPEH			10. SPONSORING / MONITORING AGENCY REPORT NUMBER PL-TR-93-2201	
11. SUPPLEMENTARY NOTES				
12a. DISTRIBUTION / AVAILABILITY STATEMENT Approved for public release; distribution unlimited			12b. DISTRIBUTION CODE	
13 ABSTRACT (Maximum 200 words) This is one of five scientific reports describing specific research projects conducted at Weston Observatory under Contract No. F19628-90-K-0035. The research conducted under this contract covers a range of topics related to seismology in general and to nuclear test monitoring in particular. In this report, we describe a study in which we used tomographic inversion to investigate the three-dimensional variation of the seismic velocity structure of the shallow crust underlying southern New England (SNE). Group velocity dispersion curves for Rg waves with periods between 0.5 and 2.0 sec have been published for SNE. Dispersion curves from these studies and from our own analyses were converted to travel time data. Two dimensional tomography was then used to estimate group velocities for blocks into which study areas in SNE were divided. Lateral variation in group velocity across SNE is estimated from these results. A combination of the maximum likelihood inverse and forward modelling is used to determine the vertical velocity structure beneath some of these blocks and for other subregions of SNE.				
14 SUBJECT TERMS Shallow crustal structure, Rg wave dispersion, tomographic inversion			15. NUMBER OF PAGES 156	
			16. PRICE CODE	
17 SECURITY CLASSIFICATION OF REPORT Unclassified	18 SECURITY CLASSIFICATION OF THIS PAGE Unclassified	19 SECURITY CLASSIFICATION OF ABSTRACT Unclassified	20. LIMITATION OF ABSTRACT SAR	

CONTENTS

1. INTRODUCTION	1
2. BACKGROUND	5
2.1 A Review of Surface Waves	5
2.2 Tomography and Lateral Variation in Group Velocity of Rg Waves	6
2.3 Dispersion of Rg Waves and Vertical Velocity Structure	13
3. PREVIOUS STUDIES OF THE SEISMIC VELOCITY STRUCTURE OF THE SHALLOW CRUST BENEATH SOUTHERN NEW ENGLAND	14
4. GEOLOGY OF SOUTHERN NEW ENGLAND	28
5. LATERAL VARIATION IN GROUP VELOCITY	34
5.1 Determining Lateral Velocity Variation Using Tomography	34
5.2 Inverse theory	36
5.2.1 The Generalized Inverse	38
5.3 The Solution Obtained from a Tomographic Inversion	51
5.3.1 Errors Mapped from the Data to the Solution	51
5.3.2 Resolution of the Solution	53
5.4 Program Development	54
6. VERTICAL VARIATION IN GROUP VELOCITY	57
7. DATA ANALYSIS	59
7.1 The Determination of Lateral Variation in Group Velocity	59
7.1.1 Preparation of Observed Rg Travel Times for Tomographic Inversion	60
7.1.2 The Analysis of Lateral Variation in Group Velocity	81
7.2 The Determination of Vertical Variation in Shear Wave Velocity	86
7.2.1 Preparation of Dispersion Data for the Analysis of Vertical Variation	86
7.2.2 The Analysis of Vertical Variation in Shear Wave Velocity	93
8. RESULTS	94
8.1 Study Area A	95

8.1.1 Dispersion Across Study Area A	95
8.1.2 Shear Wave Velocity Models for Study Area A	109
8.2 Study Area B	109
8.2.1 Dispersion Across Study Area B	109
8.2.2 Shear Wave Velocity Models for Study Area B	122
9. CONCLUSIONS	123
9.1 Study Area A	123
9.1.1 Lateral Variation Across Study Area A	123
9.1.2 Three-Dimensional Variation in Shear Wave Velocity within Study Area A	126
9.2 Study Area B	128
9.2.1 Lateral Variation Across Study Area B	128
9.2.2 Three-Dimensional Variation in Shear Wave Velocity within Study Area B	131
9.3 Effectiveness of Tomographic Analyses and Inversion Methods in the Determination of Three-Dimensional Velocity Variation	131
10. FUTURE WORK	132
10.1 Modifications to the Tomographic Inversion Program SURFTOMO	132
10.2 Modifications to the Interpretation of Velocity Results from the Analysis	133
10.3 Modifications to the Analysis of Lateral Variation of Group Velocity	134
REFERENCES	136
ADDENDUM	139

Accession For	
NTIS	<input checked="" type="checkbox"/>
CRA&I	<input type="checkbox"/>
DTIC	<input type="checkbox"/>
TAB	<input type="checkbox"/>
Unannounced	<input type="checkbox"/>
Justification	
By	
Distribution /	
Availability Codes	
Dist	Avail and / or Special
A-1	

Illustrations

Figure 1 (A) A hypothetical tomographic problem, and (B) hypothetical group velocities obtained from the tomographic inversion of Rg waves.

Figure 2 A hypothetical example of how tomography is used in this study.

Figure 3 (A) 37 paths superimposed over the study area, (B) this study area divided into two blocks, and (C) this study area divided into thirty blocks.

Figure 4 Paths used in previous studies [Figure 1(b) taken from Kafka and Skehan (1990)].

Figure 5 Dispersion regions identified by previous studies [Figure 4 taken from Kafka and Skehan(1990)].

Figure 6 Dispersion regions modified after the error in the location of BCT was found by Kafka and Bowers (1991). The entire area on both sides of the Hartford Rift basin that has group velocities similar to those of the BADR will, in the remainder of this thesis, be referred to as the Southern New England Crystalline Basement (SNECB). [Figure 1.1.1 taken from D'Annolfo (1992)].

Figure 7 Station locations and paths used by D'Annolfo (1992) [Figure 1.2.1 taken from D'Annolfo (1992)].

Figure 8 Group Velocity curves in D'Annolfo (1992) [Figure 5.1 taken from D'Annolfo (1992)].

Figure 9 Dispersion curves for the BADR observed by 1) studies prior to D'Annolfo (1992) and 2) D'Annolfo (1992). The dispersion region labelled BADR is referred to as the SNECB in this study [Figure 5.2 taken from D'Annolfo (1992)].

Figure 10 A plot of group velocity at a period of 0.7 sec versus distance [Figure 5.6(b) taken from D'Annolfo (1992)].

Figure 11 A plot of group velocity ($T = 0.7$ sec) as a three dimensional surface [Figure 5.7(b) taken from D'Annolfo (1992)].

Figure 12 Shear wave velocity models [Figure 2.1 taken from Tu (1990)].

Figure 13 Shear wave velocity models [Kafka and Skehan (1990)]. The dispersion regions labelled the BADR is referred to as the SNECB in this study [Figure 5a taken from Kafka and Skehan (1990)].

Figure 14 Study areas A and B in SNE.

Figure 15 Lithotectonic terranes for New England. [Figure 5a taken from Spotila (1992)].

Figure 16 A synthetic example with a known solution and a simple 2x1 block structure.

Figure 17 Flow chart of the computer program used for tomographic inversion.

Figure 18 The synthetic example using only one data value, d_4 .

Figure 19 The synthetic example using only three data values, d_1 , d_2 , and d_3 .

Figure 20 The synthetic example using seven data values.

Figure 21 Path information (unevenly distributed) at a period of 0.7 sec for (a) study area A and (B) study area B.

Figure 22 Paths in study area A represented by the R_g observed travel times at (A) $T=0.5$, (B) $T=0.7$, (C) $T=0.9$, (D) $T=1.1$, (E) $T=1.3$, and (F) $T=1.5$.

Figure 23 Paths in study area B represented by the R_g observed travel times at (A) $T=0.5$, (B) $T=0.7$, (C) $T=0.9$, and (D) $T=1.1$.

Figure 24 Typical dispersion curve for a path within the BADR.

Figure 25 Dispersion data for the SNECB (Kafka, 1988; D'Annolfo, 1992), and along the path from the San-Vel/Lonestar Quarry (LTMA) to the NESN station WES.

Figure 26 Dispersion data for the SNECB (Kafka, 1988; D'Annolfo, 1992), and dispersion data recorded at the Sterling, MA (STMA) array (D'Annolfo, 1992).

Figure 27 (A) Group velocity results from a tomographic inversion, (B) "stacking" group velocity results for several periods, and (C) a dispersion curve for each block. An inversion of each curve yields a shear wave velocity structure for each block.

Figure 28 (A) (Top) A 3x2 block structure divides study area A into six blocks.

(Bottom) A 5x6 block structure divides study area A into thirty blocks. (B) Paths represented by R_g observed travel times at $T=0.7$ are superimposed over the 3x2 block structure (top) and the 5x6 block structure (bottom). Curvature of the earth is not taken into account.

Figure 29 Study area A: Group velocity results at periods 0.5, 0.7, 0.9, 1.1, 1.3, and 1.5 sec using (top) a 3x2 block structure and (bottom) a 5x6 block structure (a * indicates the absence of path segments in a block).

Figure 30 Study area A: Dispersion results using (top) a 3x2 block structure and (bottom) a 5x6 block structure (only blocks containing path segments are shaded).

Figure 31 Study area A: Variance of each group velocity at $T=0.7$ sec.

Figure 32 Study area A: Dispersion results using (top) a 3x2 block structure and (bottom) a 5x6 block structure (shaded blocks exhibit "high quality" dispersion).

Figure 33 Study area A: Dispersion curves for the SNECB and for blocks exhibiting "high quality" dispersion of (A) the 3x2 block structure and (B) the 5x6 block structure.

Figure 34 Study area A: The resolution of the group velocity at $T=0.7$ sec for blocks 10, 15, and 20 respectively, where each plot is representative of rows 10, 15, and 20 respectively of the model resolution matrix R .

Figure 35 Study area A: Dispersion curves for block 13 and the SNECB (D'Annolfo, 1992) inverted by RGINV, and for block 13 and the SNECB as predicted by the shear wave velocity models in Figure 36.

Figure 36 Study area A: Shear wave velocity models obtained from the inversion of the original dispersion data in Figure 35 for block 13 and the SNECB (D'Annolfo, 1992).

Figure 37 Study area B: (Top) Divided into 81 blocks (* = location of the San-Vel/Lonestar Quarry), and (bottom) paths at $T=0.7$ superimposed over the 9x9 block structure. Curvature of the earth is not taken into account.

Figure 38 Study area B: Group velocity results.

Figure 39 Study area B: Dispersion results.

Figure 40 Study area B: Dispersion curves for blocks exhibiting "high quality" normal dispersion.

Figure 41 Study area B: Dispersion results (shaded blocks exhibit "high quality" normal dispersion).

Figure 42 Study area B: Three dispersion curves predicted by the shear wave velocity models in Figure 43.

Figure 43 Study area B: Shear wave velocity models corresponding to the dispersion curves shown in Figure 42.

Figure 44 Study area A: Dispersion results from previous studies (e.g. kafka and Skehan, 1990) superimposed over (A) the 3x2 block structure and (B) the 5x6 block structure.

Figure 45 Study area A: Regional geology superimposed over (A) the 3x2 block structure, and (B) the 5x6 block structure.

Figure 46 Study area B: Dispersion results from D'Annolfo (1992) superimposed over the 9x9 block structure.

Figure 47 Study area B: Regional geology superimposed over the 9x9 block structure.

Tables

Table 1 Dispersion observed for southern New England by various authors.

Table 2 Lithotectonic terranes mapped in Figure 15.

Table 3 Data values for a synthetic example.

Table 4 Data values for the synthetic example with errors that one might expect in a practical case.

Table 5 Study area A: Stations of the New England Seismic Network (NESN).

Table 6 Study area A: Event information (A) recorded over the GDAS array, (B) Event information recorded at the NESN station WES, (C) taken from Kafka (1990), and (D) taken from Dollin (1984), Saikia et al. (1986), and Gnewuch (1987).

Table 7 Study area B: (A) Locations of stations used by D'Annolfo (1992), and (B) Event information recorded by D'Annolfo (1992).

Table 8 (A) Study area A: Variance for each data set, and (B) Study area B: Variance for each data set.

Table 9 Resolution of group velocities for study area A for a 5x6 block structure.

Table 10 Variance of group velocities for study area A using a 5x6 block structure.

Table 11 The resolution and variance for the shear wave velocity models obtained for study area A.

Table 12 Resolution of group velocities for study area B using a 9x9 block structure.

Table 13 Variance of group velocities for study area B using a 9x9 block structure.

PREFACE

This is one of five scientific reports describing specific research projects conducted at Weston Observatory under Contract No. F19628-90-K-0035. The research conducted under this contract covers a range of topics related to seismology in general and to nuclear test monitoring in particular.

This report consists of an M.S. thesis written by Allyn K. Bowers under the supervision of Professor Alan L. Kafka. In this study, we used tomographic inversion to investigate the three-dimensional variation of the seismic velocity structure of the shallow crust underlying southern New England (SNE). Group velocity dispersion curves for Rg waves with periods between 0.5 and 2.0 sec have been published for SNE. Dispersion curves from these studies and from our own analyses were converted to travel time data. Two dimensional tomography was then used to estimate group velocities for blocks into which study areas in SNE were divided. Lateral variation in group velocity across SNE is estimated from these results. A combination of the maximum likelihood inverse and forward modelling is used to determine the vertical velocity structure beneath some of these blocks and for other subregions of SNE. The results suggest that three dimensional variation exists within the shallow crust underlying SNE, both within areas where the crystalline basement is at or near the surface and within the Hartford Rift basin, which is covered by layers of sediments and sedimentary rocks.

There are two appendices to this M.S. thesis that are not published as part of this report. Appendix A is an extensive list of travel time data for all paths in this study, and Appendix B shows graphs of all dispersion curves from this study. Those appendices are available from the authors.

1. Introduction

The seismic velocity structure of the crust beneath southern New England (SNE) has been extensively studied using both body wave and surface wave data (e.g. Chiburis et al., 1977; Taylor and Toksöz, 1979, 1982; Witek, 1984, 1987; Kafka and Dollin, 1985; Saikia et al., 1990). A number of studies have used the dispersive properties of surface waves, specifically short-period Rayleigh waves (Rg), to study the velocity structure of the upper few kilometers of the crust beneath New England (e.g. Kafka and Dollin, 1985; McTigue, 1986; Saikia et al., 1990; Gnewuch, 1987; Kafka and Skehan, 1990; Tu, 1990; Kafka and Bowers, 1991; D'Annolfo, 1992).

Quarry blasts and shallow focus earthquakes occur at shallow depths and, as a result, produce strong Rg waves. Therefore seismograms generated by these two kinds of sources were used in this and other Rg dispersion studies. In all of these previous Rg dispersion studies, group velocity was measured for each source-receiver path at a range of periods to determine lateral variation in group velocity dispersion. In several of these studies, the dispersion curves for specific paths and/or the average dispersion curve for a specific area were inverted to yield an estimate of the seismic velocity structure of the shallow crust beneath some part of SNE. These results were then used to assess the extent of vertical variation in the seismic structure of the shallow crust from the shear wave velocity structure.

The resulting models of the seismic velocity structure of the shallow crust beneath SNE have suggested that lateral and vertical variation in seismic velocity exists across

SNE. However, a more complete picture of what can and cannot be said about the three-dimensional variation of the velocity structure based on the observed Rg data from all of these previous Rg dispersion studies can be obtained by systematically analyzing the data using computer tomography. Furthermore, a tomographic study that isolates dispersion for segments of paths rather than depending on dispersion for the entire length of each path may effectively isolate dispersion data for subregions within SNE that have not been identified in previous studies. This thesis is intended to be such a systematic tomographic study.

One of the problems encountered in addressing this topic is that the group velocity data from all of the Rg studies in SNE exhibit a very large amount of scatter. Nonetheless, there does appear to be a systematic "signal" buried within this "noise".

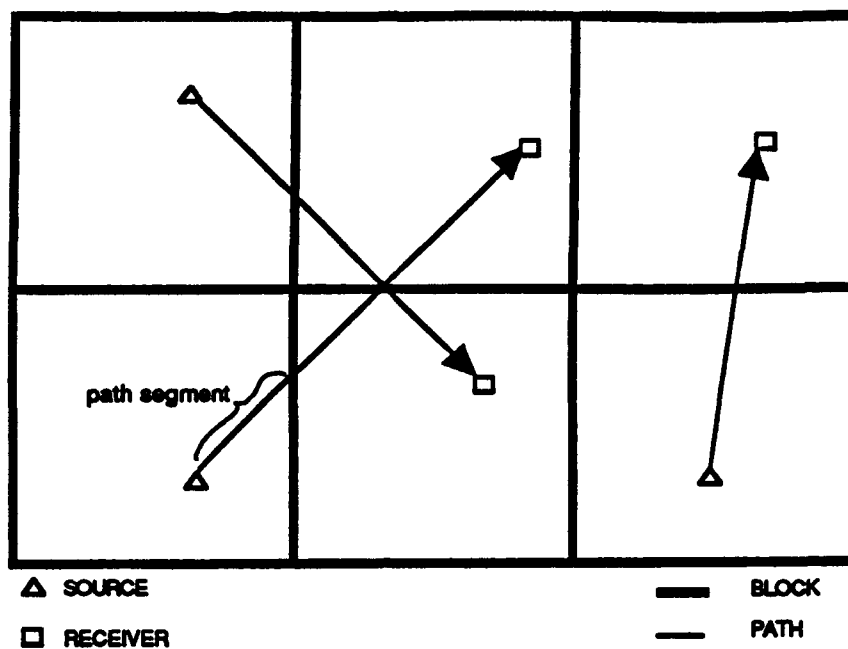
The following fundamental questions provide the underlying framework for this study:

- 1) In spite of the very large amount of scatter in the group velocity data, to what extent can a tomographic analysis of that data delineate lateral variation in Rg dispersion across SNE?
- 2) Once the dispersive characteristics have been estimated for a given sub-region of the study area, how accurately can one estimate the vertical variation of the shear wave velocity structure beneath that sub-region?

To address the first question, a systematic analysis was done on the lateral variation of Rg group velocities obtained from the studies published since 1985. This systematic analysis involves the use of computer tomography to estimate the lateral variation in group velocity across SNE. First, the study area is divided into equally-sized

blocks. Paths whose source and receiver are contained within the study area are superimposed over the study area and divided into segments by the boundaries of each block [Figure 1(A)]. For each frequency, tomography is then used to estimate the group velocity within each block [Figure 1(B)]. This estimation is based on the group velocities corresponding to the path segments that cross each block. Finally, group velocities are compared between adjacent blocks. A judgement is made as to whether the differences in group velocity are due to 1) actual velocity variation within the earth's crust, or 2) errors introduced into the analysis because of the way the problem is formulated, or errors mapped from the observed data.

To address the second question, inversion theory is used to estimate the vertical variation in shear wave velocity. For a given sub-region of the study area, the observed group velocity at a specific frequency is indicative of shear wave velocities at some range of depths. Once the tomographic analysis is successfully carried out, group velocities are estimated at a range of frequencies for specific blocks, which yields a dispersion curve for each of those blocks. Using inverse theory, a shear wave velocity model is then estimated for each block based on the dispersion curve corresponding to that block. By combining the results for all of the blocks, a three-dimensional model can be obtained for the study area.



(A)

$U = 2.5 \text{ KM/SEC}$	$U = 2.2 \text{ KM/SEC}$	$U = 2.6 \text{ KM/SEC}$
$U = 2.4 \text{ KM/SEC}$	$U = 2.3 \text{ KM/SEC}$	$U = 2.6 \text{ KM/SEC}$

(B)

Figure 1 (A) A hypothetical tomographic problem, and (B) hypothetical group velocities obtained from the tomographic inversion of Rg waves.

2. Background

2.1 A Review of Surface Waves

Surface waves propagate along the free surface of the earth and are affected by the earth structure beneath the surface. Like other surface waves propagating in a medium with depth dependent properties, Rg waves are dispersive. As the wavetrain propagates from source to receiver, the shape of the wavetrain changes. In general, each frequency component arrives at a different time than the other frequency components.

In the case of normal dispersion, lower frequency components arrive earlier than higher frequency components. This normal dispersion is the result of a layered earth structure where velocities generally increase with depth. The velocities of frequency components of Rg waves are affected by the properties of the earth's crust in some subset of the layers. Lower frequency components of the wavetrain are affected by the properties of the earth's crust at a greater depth and, hence, travel with a greater velocity. Dispersion in the period range of 0.5 to 1.5 sec is indicative of the earth structure at depths ranging from very near the surface down to about 1 to 2 km (e.g. Kafka and Reiter, 1987).

Since Rg waves are dispersive, two kinds of velocity can be measured from an Rg signal, phase velocity and group velocity. Phase velocity is the velocity with which a particular point of phase, for example a peak or trough, propagates. Group velocity, on the other hand, is the velocity with which a specific frequency component of an Rg signal propagates. This frequency component can be isolated from the Rg signal by

applying a narrow band pass filter to the Rg signal. A small range of frequencies are passed through the filter, and the center frequency is an estimate of the frequency that is isolated by this process. The relationship between group velocity, U , and phase velocity, c , can be expressed as

$$U = c - \lambda \frac{\delta c}{\delta \omega} = c + \omega \frac{\delta c}{\delta \omega} \quad (2.1)$$

where λ is the wavelength and ω is the frequency.

2.2 Tomography and Lateral Variation in Group Velocity of Rg Waves

Tomography

In this study, tomography is used to determine lateral variation of Rg group velocities. The study area is divided into a number (M) of equally-sized blocks, and a tomographic analysis is used to estimate the group velocity for each block. In a tomographic analysis, the group velocity within each block is estimated from observed travel times of Rg waves propagating across many paths traversing the study area. The observed travel times are taken from paths whose source and receiver are both within SNE. For simplicity in the mathematical formulation of the problem, the group velocity (U) within each block, is expressed as a slowness m (a model parameter) where

$$m = \frac{1}{U} \quad (2.2)$$

The slowness within each block is converted to a group velocity at the end of the tomographic inversion.

A tomographic problem is outlined in the following way. The study area is divided into a grid of M blocks. For example, a 3×2 block structure is constructed from 3 blocks in the longitudinal direction and by 2 blocks in the latitudinal direction [Figure 2]. The slowness for each block is characterized by a model parameter m_j , where $j=1, \dots, M$. Thus for example, a 3×2 block structure has six model parameters (i.e. $M=6$).

The travel time(s) for each path are the data values, d_i , where $i=1, \dots, N$. All paths are superimposed over the block structure and divided by its boundaries into a number of smaller path segments of length g_{ij} . In the example shown in Figure 2, there are four data values d_1 , d_2 , d_3 , and d_4 . Data values d_3 and d_4 are observed travel times for the same path. Paths 1 and 2 have three path segments. The path for data values 3 and 4 has two path segments each [Figure 2].

The travel time for each path segment associated with data value i in block j , d_{ij} , can be expressed as

$$d_{ij} = g_{ij} * m_j \quad (2.3)$$

The travel time for data value i , d_i , is equal to the sum of the travel times for all of its segments.

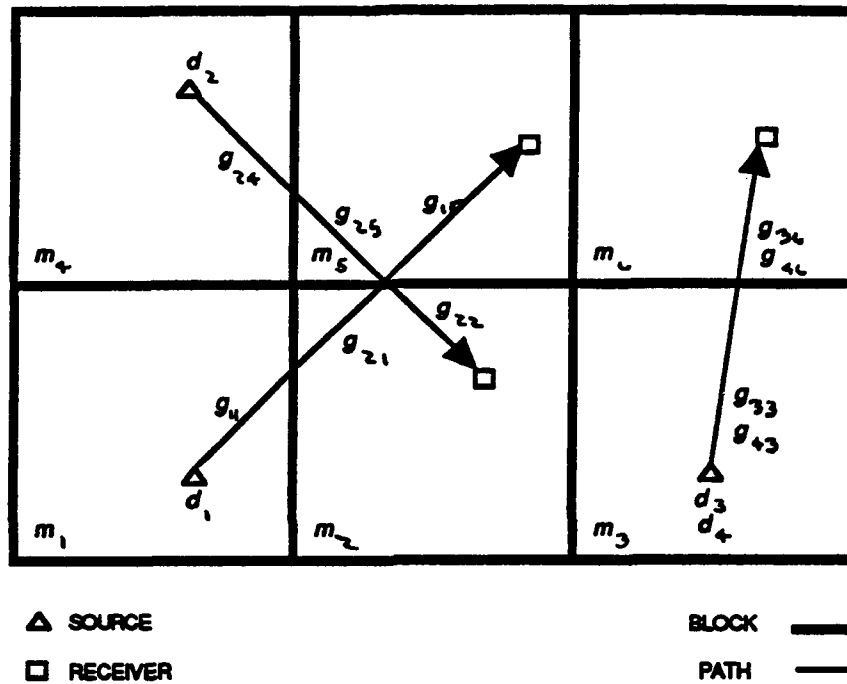


Figure 2 A hypothetical example of how tomography is used in this study.

It can be expressed as

$$d_i = g_{i1} * m_1 + g_{i2} * m_2 + \dots + g_{iM} * m_M \quad (2.4)$$

Rewriting equation 2.4 for the example shown in Figure 2, we have

$$\begin{aligned} d_1 &= g_{11} * m_1 + g_{12} * m_2 + g_{13} * m_3 + g_{14} * m_4 + g_{15} * m_5 + g_{16} * m_6 \\ d_2 &= g_{21} * m_1 + g_{22} * m_2 + g_{23} * m_3 + g_{24} * m_4 + g_{25} * m_5 + g_{26} * m_6 \\ d_3 &= g_{31} * m_1 + g_{32} * m_2 + g_{33} * m_3 + g_{34} * m_4 + g_{35} * m_5 + g_{36} * m_6 \\ d_4 &= g_{41} * m_1 + g_{42} * m_2 + g_{43} * m_3 + g_{44} * m_4 + g_{45} * m_5 + g_{46} * m_6 \\ d_5 &= g_{51} * m_1 + g_{52} * m_2 + g_{53} * m_3 + g_{54} * m_4 + g_{55} * m_5 + g_{56} * m_6 \\ d_6 &= g_{61} * m_1 + g_{62} * m_2 + g_{63} * m_3 + g_{64} * m_4 + g_{65} * m_5 + g_{66} * m_6 \end{aligned} \quad (2.5)$$

Where a path associated with a data value i does not pass through block j , g_{ij} is equal to zero. For example, in the case shown in Figure 2, path 1 passes through blocks 1, 2, and 5. The path segments g_{13} , g_{14} , and g_{16} are therefore zero. Path 2 passes through blocks 2, 4, and 5, and the path segments g_{21} , g_{23} , and g_{26} are therefore also zero. Eliminating all of the zero terms, equation 2.5 can be rewritten for this example as

$$\begin{aligned} d_1 &= g_{11} * m_1 + g_{12} * m_2 + g_{15} * m_5 \\ d_2 &= g_{22} * m_2 + g_{24} * m_4 + g_{25} * m_5 \\ d_3 &= g_{33} * m_3 + g_{36} * m_6 \\ d_4 &= g_{43} * m_3 + g_{46} * m_6 \end{aligned} \quad (2.6)$$

For all data values, one can propose a set of model parameters that solves the following matrix equation:

$$\begin{bmatrix} d_1 \\ \cdot \\ \cdot \\ d_N \end{bmatrix} = \begin{bmatrix} g_{11} & g_{12} & \cdot & \cdot & g_{1M} \\ \cdot & \cdot & \cdot & \cdot & \cdot \\ \cdot & \cdot & \cdot & \cdot & \cdot \\ g_{N1} & g_{N2} & \cdot & \cdot & g_{NM} \end{bmatrix} \begin{bmatrix} m_1 \\ \cdot \\ \cdot \\ m_M \end{bmatrix} \quad (2.7)$$

or

$$d = G m \quad (2.8)$$

The vector $[m_1, \dots, m_M]^T$ is the model vector; the vector $[d_1, \dots, d_N]^T$ is the data vector. Thus, tomographic inversion involves a system of methods for solving equation 2.8 for the model parameter vector m .

Lateral Variation in Group Velocity of Rg Waves

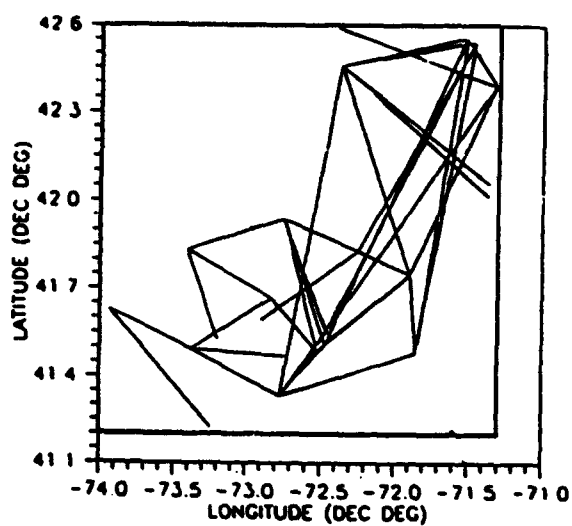
To investigate lateral variation of Rg velocities, the group velocities within adjacent blocks are compared. A judgement is made based on certain criteria as to whether the difference between these group velocities is due to 1) actual velocity variation within the earth's crust, 2) errors introduced into the analysis because of the way the problem is formulated, or 3) errors carried over from the observed data.

The extent to which lateral variation can be investigated for a study area depends on the number of blocks into which the study area is divided. If the study area is divided into only a few blocks, the investigation of lateral variation would be fairly limited, whereas a more extensive investigation would be possible with a larger number of blocks. Furthermore, the maximum number of blocks into which a study area can be divided must be less than or equal to the number of paths represented by the data values. Statistically speaking, the number of data values must be equal or greater than the number of model parameters (group velocities) for a tomographic problem to be well designed.

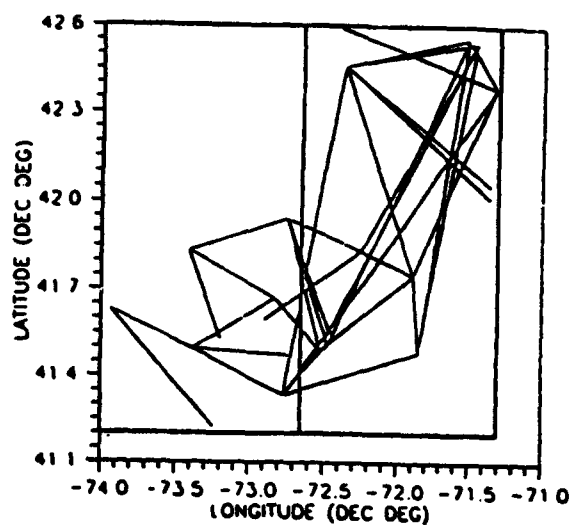
Consider one of the study areas analyzed in this study. Data values representing 37 paths have been collected. These paths are superimposed over the study area as shown in Figure 3(A).

Suppose this study area is divided into two blocks as shown in Figure 3(B). Since there are many more paths than blocks, each block contains more than enough path information to uniquely determine the group velocity within each block. However, discussions about lateral variation in group velocity would be limited to variation between the western and eastern parts of SNE. Much more group velocity information could be provided by the data values by dividing the study area into a greater number of blocks. Lateral variation could then be investigated more extensively.

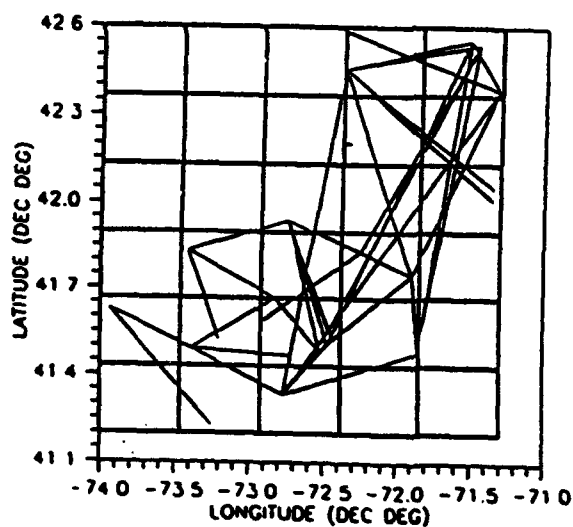
Now suppose this study area is divided into 30 blocks as shown in Figure 3(C). Since the number of paths is nearly equal to the number of blocks, the likelihood that all 30 blocks contain enough path information to determine the group velocity within these



(A)



(B)



(C)

Figure 3 (A) 37 paths superimposed over the study area, (B) this study area divided into two blocks, and (C) this study area divided into thirty blocks.

blocks is small. A tomographic inversion of this problem is possible, and if there is sufficient path coverage for at least some subset of the blocks, then discussions about lateral variation are not as limited as in the previous case.

Suppose that the study area is divided into 100 blocks. The number of paths is now much greater than the number of blocks. The likelihood that all 100 blocks contain enough path information to determine the group velocity within each of these blocks is even smaller. Furthermore, many of the blocks will probably contain extremely short path segments. A tomographic inversion using this block structure would not yield group velocities that would provide a basis for any extensive discussion about lateral variation.

2.3 Dispersion of Rg Waves and Vertical Velocity Structure

Once the tomographic analysis is successfully carried out, estimates of group velocities are obtained at a range of frequencies for specific blocks. This procedure yields a dispersion curve for each of those blocks. In addition, dispersion curves can be obtained for specific paths (by averaging many curves for that path), and for specific areas (by averaging many curves for that area). These Rg dispersion curves can then be inverted to obtain seismic velocity models of the shallow crust underlying the blocks (or paths) in question.

In this study, the Rg group velocity dispersion curves were inverted using the maximum likelihood inverse (e.g. Menke, 1984; Reiter et al., 1988). This method involves solving an equation of the form $\Delta d = G \Delta m$, using a method similar to the methods that are used for the tomographic inversion. In this case, however, the data vector Δd consists of the difference between the observed group velocities and the

theoretical dispersion calculated for a starting model. The matrix G consists of partial derivatives of group velocities with respect to the starting model parameters (S-wave velocities in the different layers), and the vector Δm is the correction to the previous solution, estimated in an iterative manner. Once the solution for Δm is calculated (using the maximum likelihood inverse), the starting solution is updated, and theoretical group velocities are recalculated for the revised model. These theoretical group velocities are compared with the observed data, and the inversion is repeated iteratively until there is no further convergence.

3. Previous Studies of the Seismic Velocity Structure of the Shallow Crust Beneath Southern New England

Several studies of the crustal velocity structure in southern New England have been carried out using data from body waves and surface waves (e.g. Chiburis et al., 1977; Taylor and Toksöz, 1979, 1982; Wenk, 1984, 1987). More recently, studies have used the dispersive properties of Rg waves to investigate the velocity structure of the upper few kilometers of the crust (e.g. Kafka and Dollin, 1985; McTigue, 1986; Saikia et al., 1990; Gnewuch, 1987; Kafka, 1988; Kafka and Skehan, 1990; Tu, 1990; Kafka and Bowers, 1991; D'Annolfo, 1992).

Studies by Kafka and Dollin (1985), McTigue (1986), Gnewuch (1987), and Kafka and Skehan (1990) have investigated lateral variation in group velocity across southern New England (SNE). The range of group velocities and the periods at which they were measured for some of these studies are listed in Table 1. The paths along

Table 1 Dispersion observed for southern New England by various authors.

AUTHORS	PERIOD (sec)	GROUP VELOCITY (km/sec)	STUDY AREA
Kafka & Dollin(1985)	0.50-2.00	2.00-3.30	Southern New England
Gnewuch(1985)	0.50-2.00	1.87-3.23	Southern New England
McTigue(1986)	0.50-2.00	2.10-2.90	MA and RI
Tu (1990)	0.30-2.00	2.30-2.90	NH and Vermont
D'Annolfo (1992)	0.20-2.20	2.00-3.29	MA and Southern NH

which Rg waves have been recorded for these studies are shown in Figure 4. The seismic sources used in these studies were either quarry blasts or shallow focus earthquakes and the receivers were stations of the New England Seismic Network (NESN).

These studies identified five areas (called dispersion regions) that were interpreted as indicating systematic lateral variation in group velocity [Figure 5]. They were the Bronson-Avalon Dispersion Region (BADR), the Hartford Dispersion Region (HDR), the New Haven Dispersion Region (NHDR), the Waterbury Dispersion Region (WDR), and the Torrington Dispersion Region (TDR). The BADR and TDR had Rg group velocities between 2.5 and 2.75 km/sec at a period of 1 sec. The HDR had group velocities between 2.0 and 2.25 km/sec at the same period. The NHDR had group velocities between 2.25 and 2.5 km/sec at a period of 1 sec (Kafka and Skehan, 1990).

The Waterbury Dispersion Region (WDR) was thought to have group velocities greater than 2.75 km/sec at a period of 1 sec. However, Kafka and Bowers (1991) discovered an error in the location of the NESN station BCT in a computer input file. This erroneous location was used by a computer program at Weston Observatory to calculate distances from several sources to BCT. These distances were then used to estimate the group velocities within the WDR. In most cases, the distances were greater than they should have been. As a result the group velocities appeared to be higher than they actually are. Using the correct distances from the sources to BCT, the group velocities in the WDR turned out to be similar to those of the BADR and the TDR (Kafka and Bowers, 1991). Therefore, it appears that all of the areas in SNE where

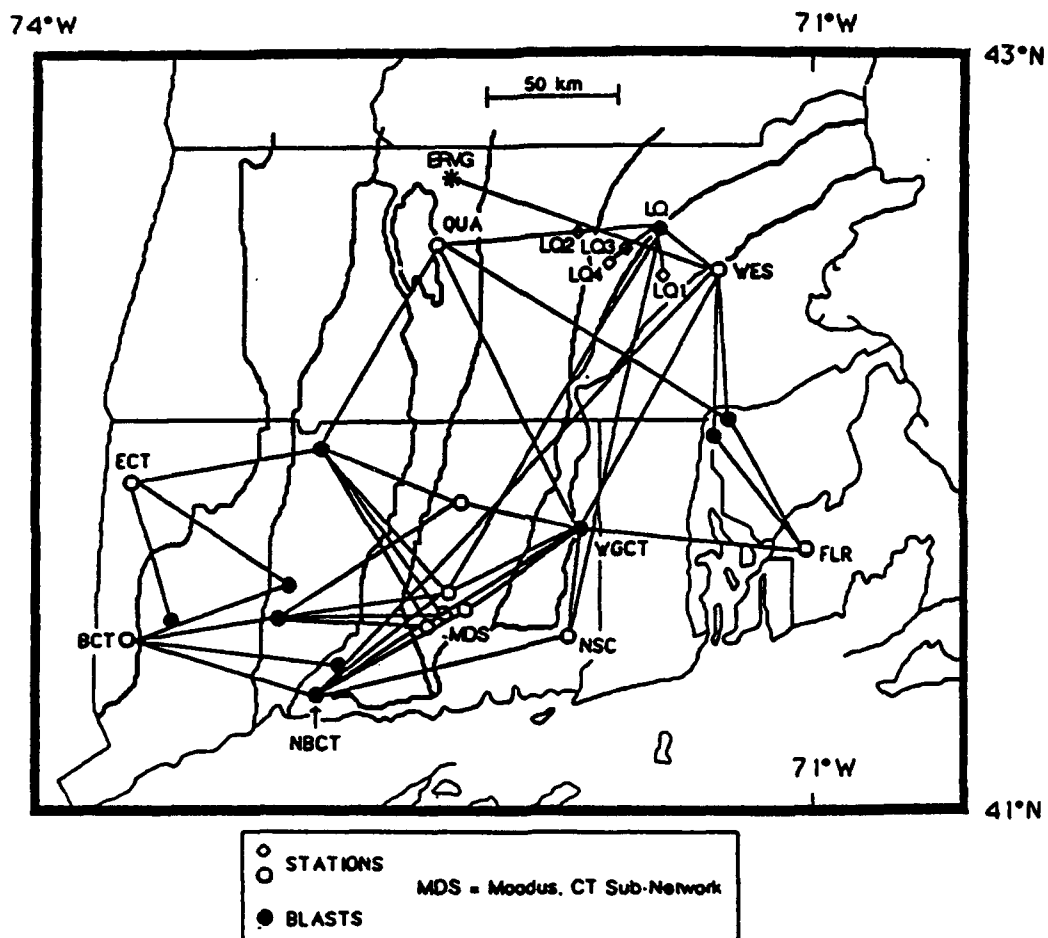


Figure 4 Paths used in previous studies [Figure 1(b) taken from Kafka and Skehan (1990)].

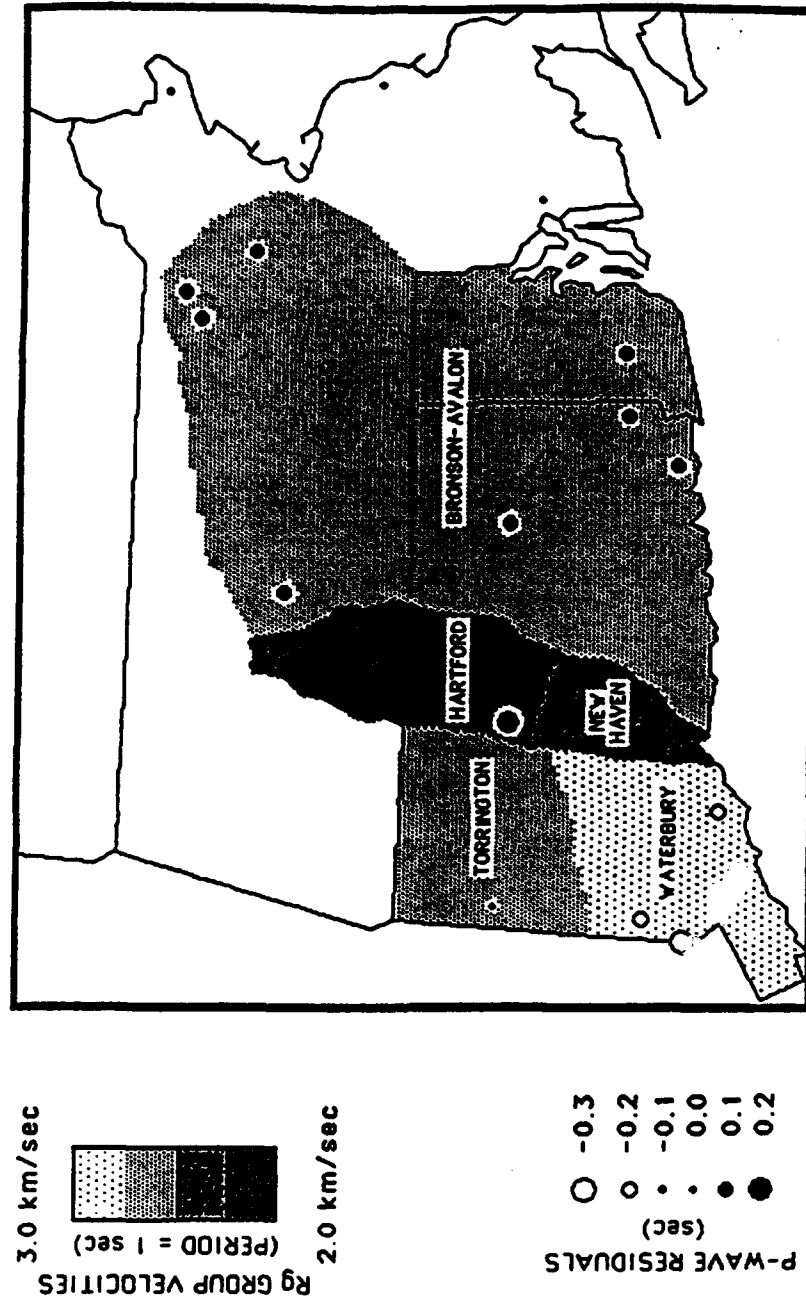


Figure 5 Dispersion regions identified by previous studies [Figure 4 taken from Kafka and Skehan(1990)].

crystalline basement is near the surface have (at least on average) group velocities similar to those of the BADR. In the remainder of this thesis I, therefore, refer to the parts of SNE on both sides of the Hartford Rift Basin (HRB) as the Southern New England Crystalline Basement (SNECB). The map showing dispersion regions [Figure 5] has been modified to reflect this change [Figure 6].

D'Annolfo (1992) investigated lateral variation in the seismic velocity structure of the shallow crust beneath eastern Massachusetts and southern New Hampshire. The paths she used are shown in Figure 7. All of the events used in her study were quarry blasts at the San-Vel/Lonestar Quarry in Littleton, Massachusetts. The receivers included field stations and NESN stations as well as stations operated by Massachusetts Institute of Technology. Her results suggested that there is systematic lateral variation in these areas. The dispersion curves for all paths from her study are plotted in Figure 8. The average dispersion curve for her data and the data published previously for the SNECB was plotted along with the dispersion curve previously published for the SNECB [Figure 9]. As noted by D'Annolfo (1992), the two curves are very similar.

D'Annolfo (1992) also plotted group velocities as a function of distance from the San-Vel/Lonestar quarry for periods of 0.5, 0.7, and 0.9 sec. Group velocities at a period of 0.7 sec are plotted as a function of station location in Figure 10. In Figure 11, group velocities at a period of 0.7 sec are plotted as a three dimensional surface over the area analyzed in her study. As noted by D'Annolfo (1992), the group velocities appear to be slower just around the quarry and increase slightly with distance from the quarry.

Prior to 1985, several P-wave velocity models were published for New England

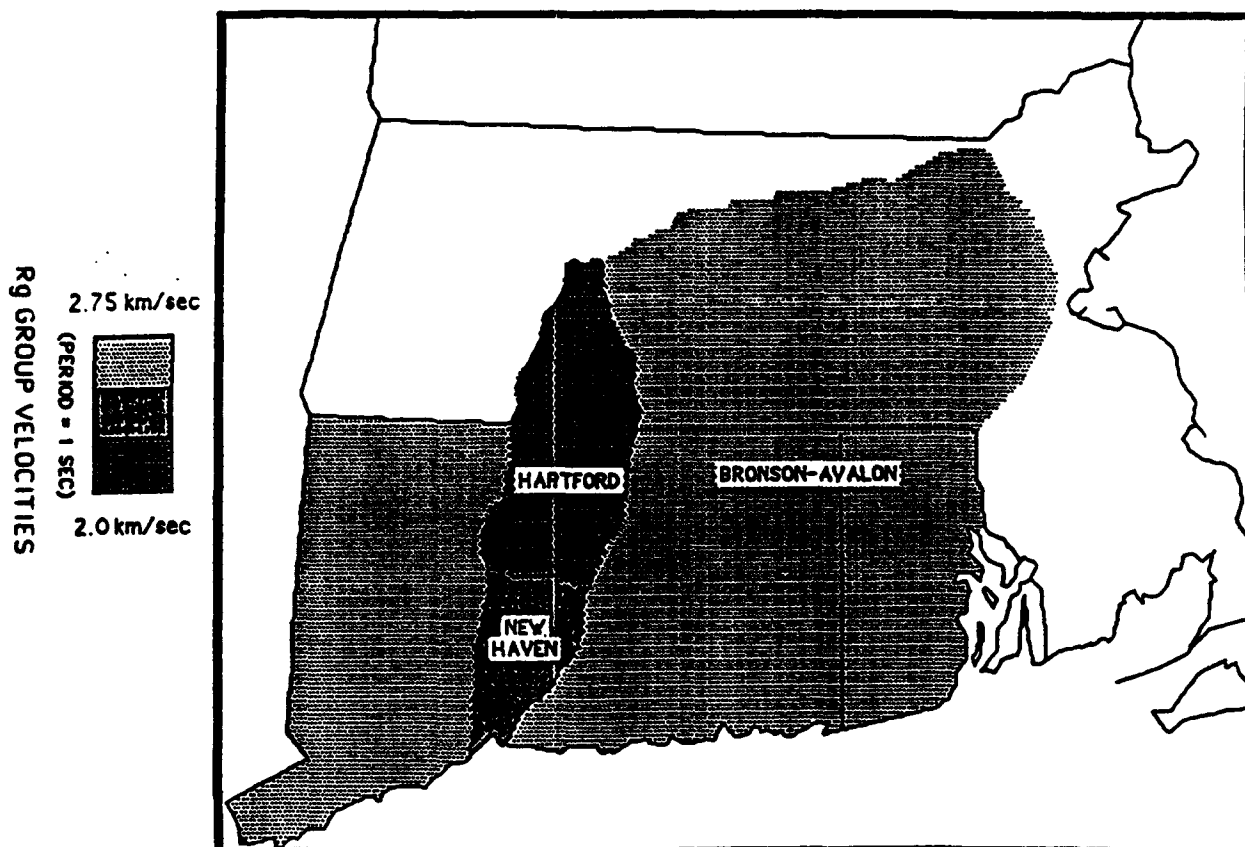
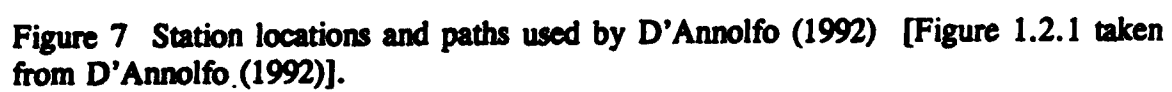


Figure 6 Dispersion regions modified after the error in the location of BCT was found by Kafka and Bowers (1991). The entire area on both sides of the Hartford Rift basin that has group velocities similar to those of the BADR will, in the remainder of this thesis, be referred to as the Southern New England Crystalline Basement (SNECB). [Figure 1.1.1 taken from D'Annolfo (1992)].



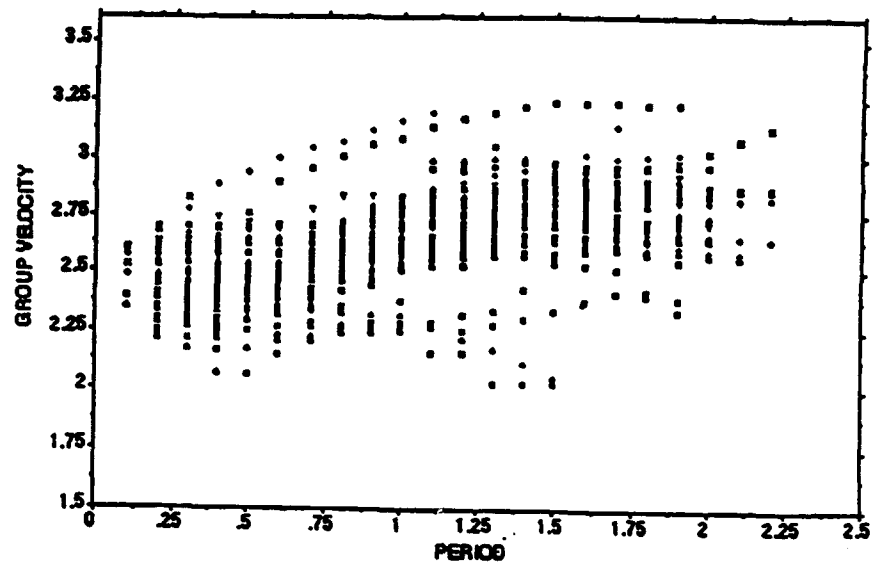


Figure 8 Group Velocity curves in D'Annolfo (1992) [Figure 5.1 taken from D'Annolfo (1992)].

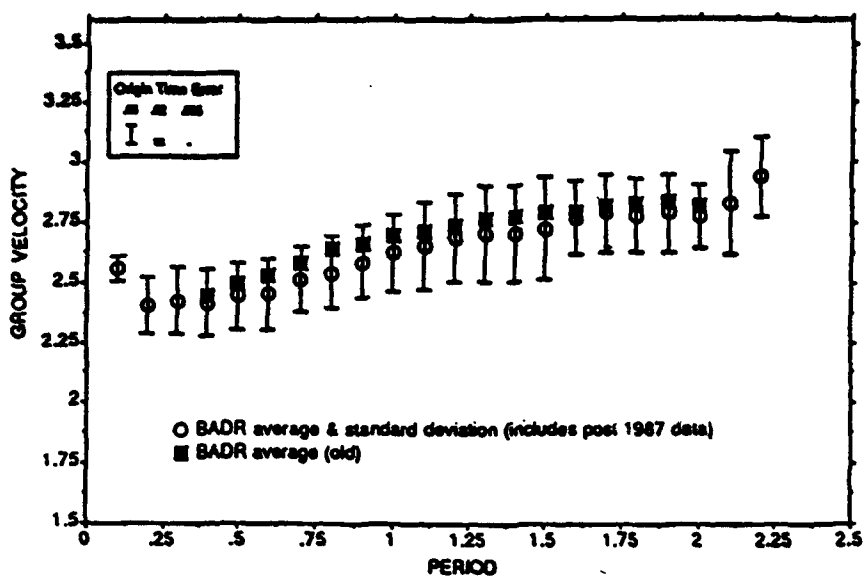


Figure 9 Dispersion curves for the BADR observed by 1) studies prior to D'Annolfo (1992) and 2) D'Annolfo (1992). The dispersion region labelled BADR is referred to as the SNECB in this study [Figure 5.2 taken from D'Annolfo (1992)].

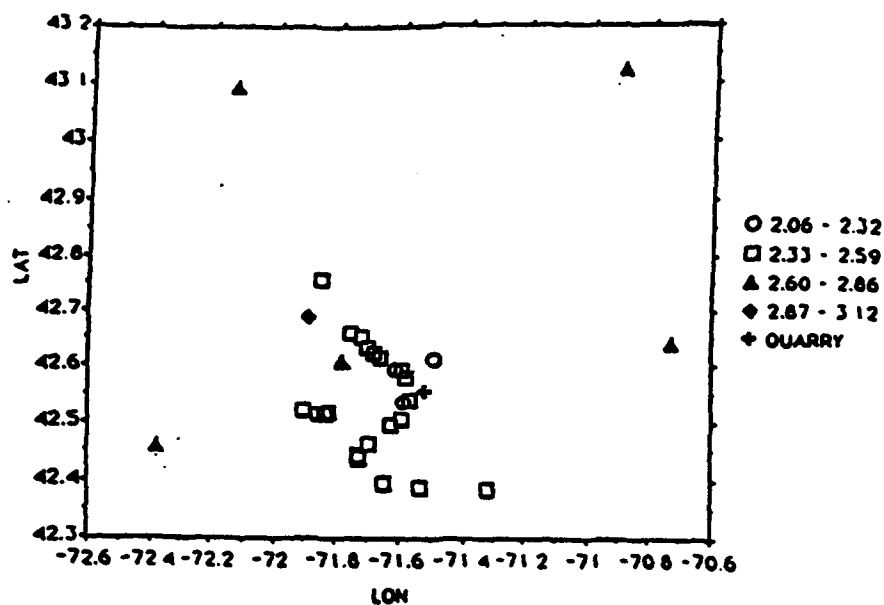


Figure 10 A plot of group velocity at a period of 0.7 sec versus distance [Figure 5.6(b) taken from D'Annolfo (1992)].

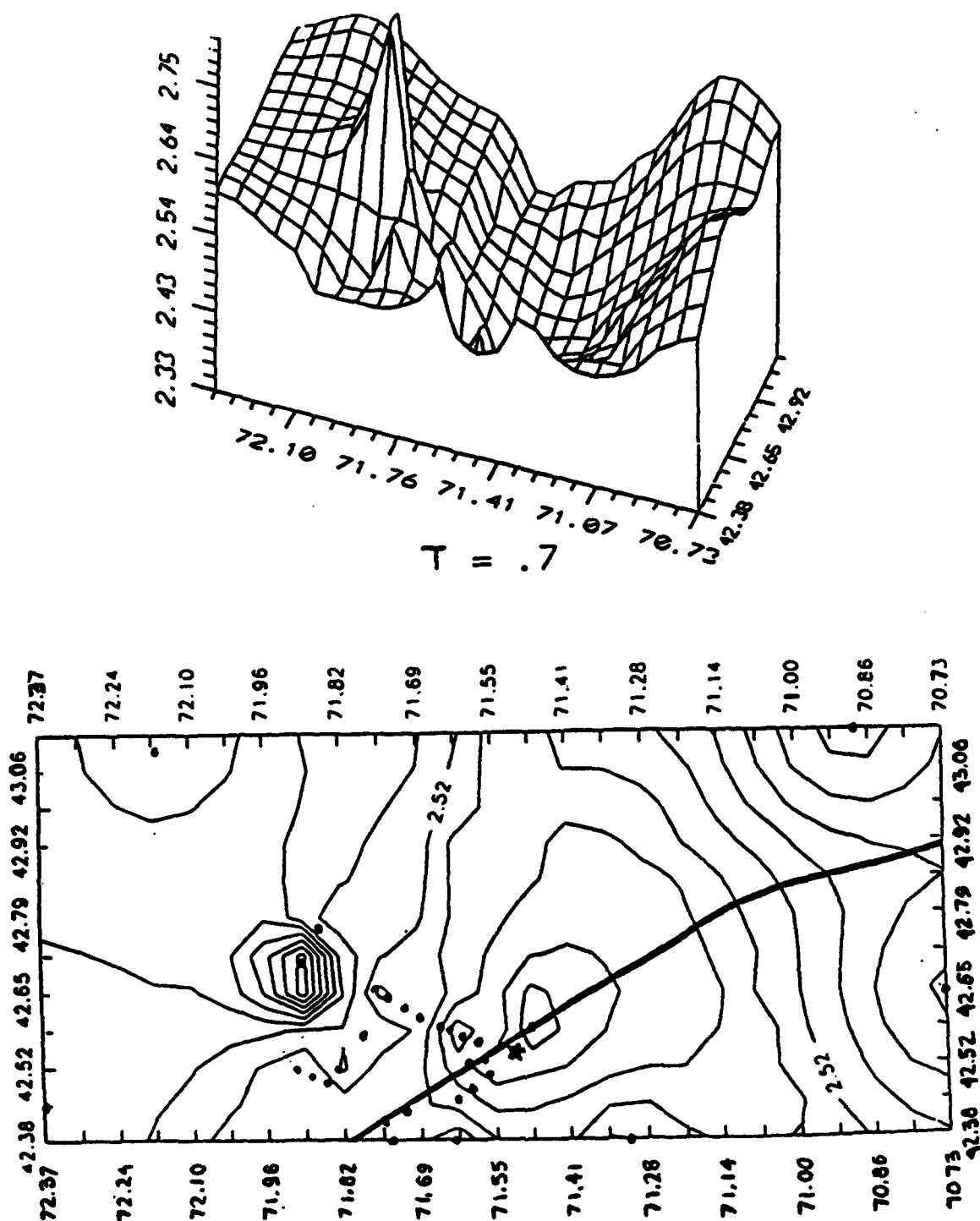


Figure 11. A plot of group velocity ($T = 0.7$ sec) as a three dimensional surface [Figure 5.7(b) taken from D'Annolfo (1992)].

based on body wave refraction studies [Figure 12]. More recent publications since 1985, such as Kafka and Dollin (1985), McTigue (1986), Saikia et al. (1990), and Kafka and Skehan (1990), have described vertical variations in shear wave velocities of the upper few kilometers of the crust. Kafka and Dollin (1985) concluded that normal dispersion between the periods 0.5-1.5 sec indicated the existence of a low velocity layer near the surface approximately 0.5 to 1.0 km in thickness. McTigue (1986) also observed normal dispersion between the periods 0.5-1.5 sec. Using the group velocity information for each dispersion region, he estimated the shear wave velocity structure of the shallow crust beneath southern New England.

Kafka and Skehan (1990) summarized the velocity structure of the shallow crust for the BADR and the HDR [Figure 13]. Since the WDR and the TDR have R_g group velocities similar to those of the BADR, one would expect the velocity structure for the SNECB to be similar to that shown in Figure 13 for the BADR.

Taylor and Toksöz (1979) and Peseckis and Sykes (1979) studied teleseismic P-wave residuals for SNE [Figure 5]. The P-wave residuals within the HDR were the slowest (0.2 sec). Those within the BADR were slightly faster at 0.1 sec. The residuals that were observed in what used to be called the WDR were the fastest at -0.3 sec. The fast residuals in the WDR were previously accredited to the (presumably) high velocity layers close to the surface (e.g. Kafka, 1988; Kafka and Skehan, 1990). Since those high velocity layers are no longer thought to exist, it was suggested by Kafka and Bowers (1991) that this high velocity material is at a greater depth than previously thought (Kafka and Bowers, 1991).

model vel. (km/s)	Model 1	Model 2	Model 6
depth (km)			
0.88	5.31		6.1
1.0		5.7	
4.0			
4.5			
5.5	6.06		
7.3			
13.09			
21.0		6.3	6.6
26.0	6.59		
26.1			
33.0			
34.6		7.3	
35.0			
37.0			
39.0	8.1		8.1
		8.13	

Model 1. Southern and Central New England, New Hampshire,
and Vermont (Chiburis, 1979)

Model 2. Central New Hampshire (Taylor-Toksoz)

Model 6. Adirondacks (Lamont-Doherty)

Figure 12 Shear wave velocity models [Figure 2.1 taken from Tu (1990)].

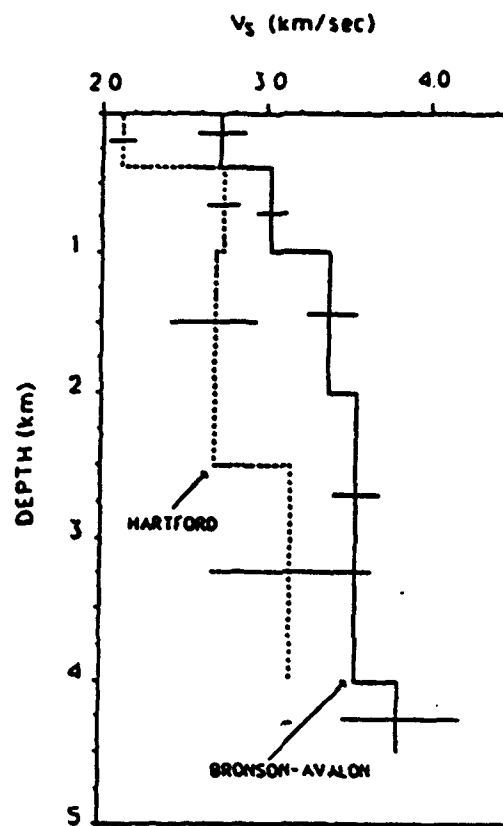


Figure 13 Shear wave velocity models [Kafka and Skehan (1990)]. The dispersion regions labelled the BADR is referred to as the SNECB in this study [Figure 5a taken from Kafka and Skehan (1990)].

4. Geology of Southern New England

Two areas are investigated in this study. The first, study area A, includes the part of SNE lying between -74.0° and -71.3° longitude and 41.2° and 42.6° latitude [Figure 14]. This region includes part of Massachusetts, Connecticut, and Rhode Island. Rg data for study area A are taken from the previous studies of that area described in Section 3 (e.g. Kafka and Dollin, 1985; Saikia et al., 1990; Gnewuch, 1987). The second, study area B, includes the part of SNE lying between -72.3739° and -70.7271° longitude and 42.3846° and 43.1226° latitude [Figure 4.1]. This area includes part of Massachusetts and New Hampshire. The Rg data from this area were acquired and analyzed by D'Annolfo (1992). Based on these studies, SNE appears to be laterally isotropic and, therefore, all assumptions about laterally isotropic media are assumed to be valid for the purposes of this study.

Figure 15, taken from Spotila (1992), shows the exposed lithotectonic terranes of SNE. Table 2 lists the names of each terrane. The region is geologically complex. This complex structure is considered to be the result of massive plate collisions in the Northern Appalachians during the Middle Proterozoic through the Mesozoic (e.g. Kafka and Skehan, 1990).

The part of the SNECB, that lies on the western side of the HDR, is associated with three terranes [Figure 15]. From west to east, they are the Taconic allochthons (3), the allochthonous Grenville Massifs (6), and Medial New England (1) (Table 2). The Taconic allochthons (3) form a sequence of slices transported during complex thrust faulting. The rocks at the lower end of the sequence are from late Proterozoic to middle

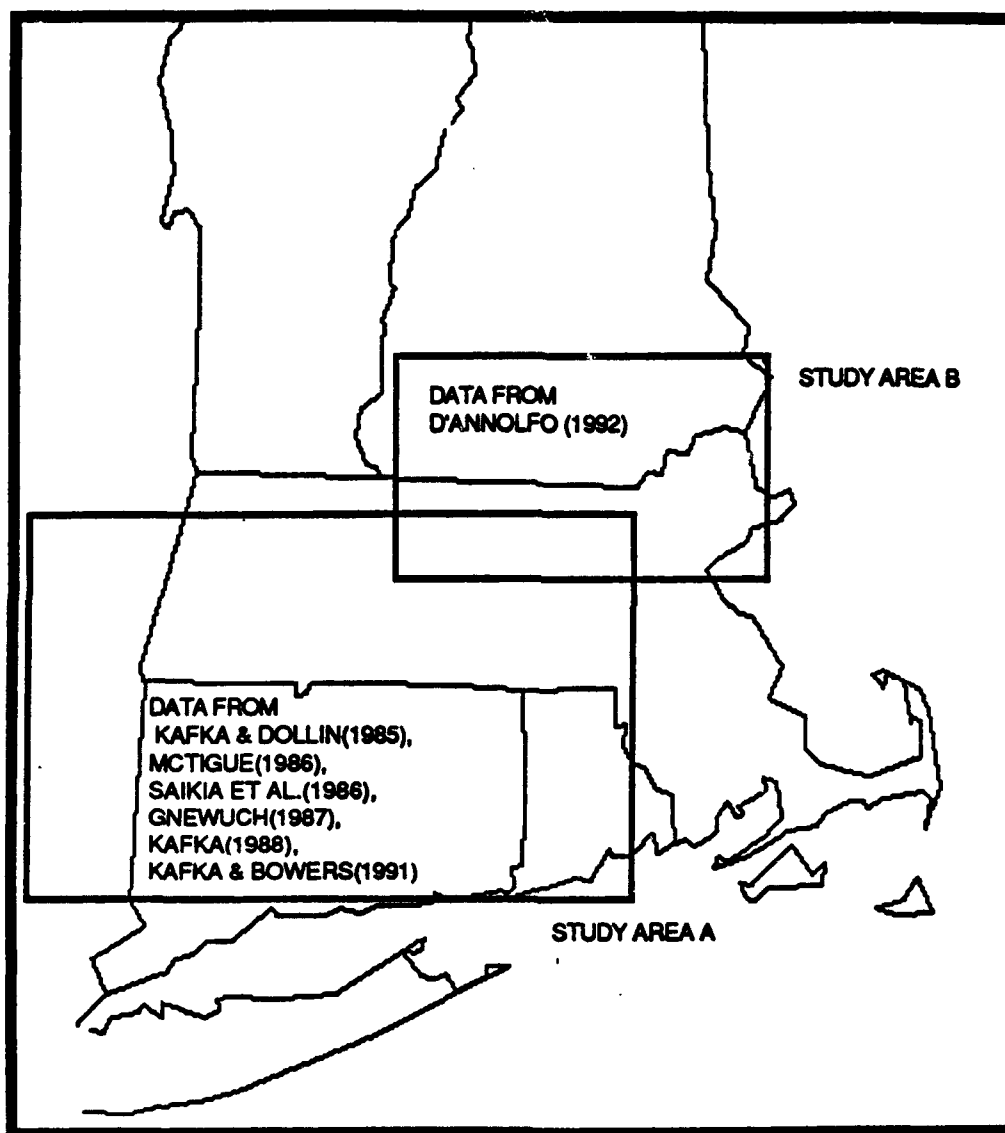


Figure 14 Study areas A and B in SNE.

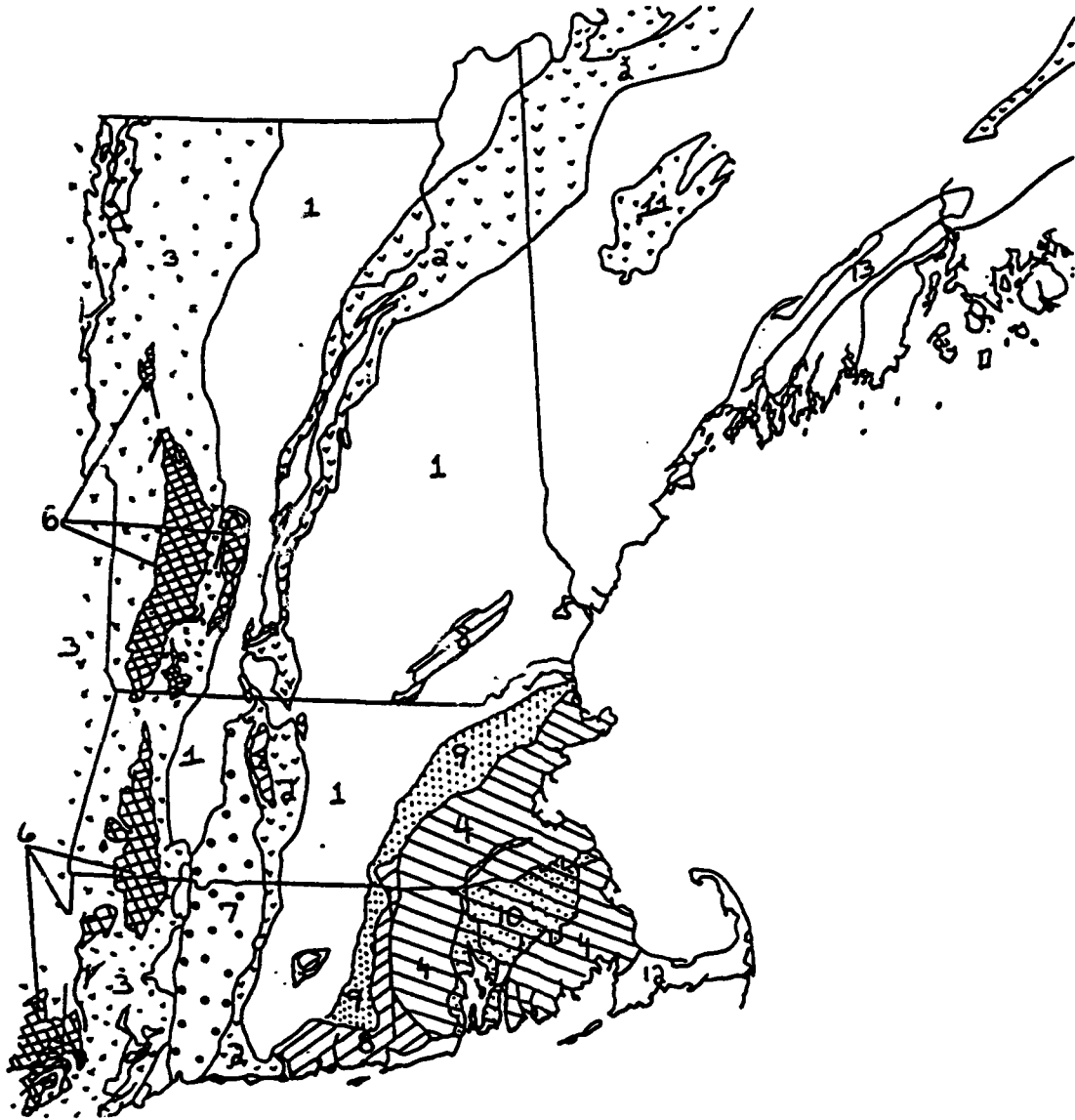


Figure 15 Lithotectonic terranes for New England. [Figure 5a taken from Spotila (1992)].

Table 2 Lithotectonic terranes mapped in Figure 15

1. **Medial New England:** contains Acadian accreted rock of the oceanic basins and volcanic arc, now exists as the CT Valley - Gaspé Synclinorium, the Kearsage - Central ME Synclinorium (Merrimack), the Northern ME Anticlinorium, the Miramichi anticlinorium, and the Fredericton Trough.
2. **Bronson Hill:** contains Taconic accreted rock of the Iapetus volcanic arc island, now exists as an anticlinorium.
3. **Taconic Allochthons:** includes only the Taconic accreted strata from the Laurentian continental margin, that now exists as the Taconic klippe.
4. **Esmond - Dedham Avalon:** eastern most Avalon of the Alleghanian collision.
5. **ME Coastal Volcanic:** volcanic belt of Alleghanian (?) age.
6. **Allochthonous Grenville Massifs:** part of the Grenville continent ripped up into the klippe of the Taconic event.
7. **Hartford Basin:** Triassic sedimentary basin formed in a half-graben.
8. **Hope Valley Avalon:** Avalon of the Acadian collision.
9. **Putnam-Nashoba Avalon:** considered to be part of the Acadian collision of Avalon and North America, but may have collided on its own as a separate terrane.
10. **Narragansett Basin:** Permian basin formed in transcurrent Alleghanian fault block.
11. **Rumford Allochthon:** either an Acadian underthrust sheet or a pre-Acadian slump in semi-lithified sediments.
12. **Meguma:** large terrane or plate that collided with Avalon and North America in the Alleghanian.
13. **Misc. ME Allochthonous Basement:** unknown.

Ordovician in age, and overlay tectonized sedimentary melange. These rocks consist partly of green laminated slate, grit, graywacke, and quartzite. The upper part of the lower Taconic sequence contain slivers of carbonate and siliclastic rocks. The higher part of the Taconic sequence lies to the east of the lower sequence and is a clastic sequence similar to that which is seen in Medial New England (1) (Hatcher, Thomas, and Viele; 1989).

The allochthonous Grenville Massifs (6) were part of the Grenville basement. During the Taconic orogen, these Massifs were brought onto the Taconic klippe. These crystalline rocks are middle Proterozoic in age. The Massifs in southern New England include, from north to south, the Berkshire Massif, the Housatonic Massif, and the Eastern Hudson Highlands. The Berkshire Massif has been studied extensively. These rocks have a "distinctive fold thrust fabric" (Hatcher, Thomas, and Viele; 1989), having recumbent folds and foliation. The deformation in this massif is considerably more ductile than that in the other two (Hatcher, Thomas, and Viele; 1989).

Medial New England (1) includes the Connecticut Valley - Gaspé Synclinorium. This terrane was accreted during the Acadian Orogeny. Cambrian and Ordovician portions along its western border are composed of schists, metamorphosed mafic volcanics, and ultramafics. The basement of Medial New England contains quartzofeldspathic gneisses. The Cambrian sequence within this terrane, with the exception of the ultramafics, contains wackes and phyllites. The Ordovician sequence contains volcanic, phyllites/schists, and wacke (Hatcher, Thomas, and Viele; 1989).

Both the HDR and the NHDR are associated with the Hartford Rift Basin (7), a

sedimentary basin formed in a half-graben. Bordered by normal faults to the east and west, this terrane contains Mesozoic red bed sediments and igneous rocks covered by Pleistocene glacial sediments. The composition of the HRB is distinct from the composition of the other lithotectonic terranes in SNE. These Mesozoic and Pleistocene sediments are relatively thick in the northern part of the HRB, and are thinner on average in the southern part of the HRB (e.g. Kafka and Skehan, 1989). Refraction profiles by Wenk (1984) indicate that higher velocities are found at greater depths in the northern part of the HRB than in the southern part. This result supports the geological interpretation.

The part of the SNECB, that lies on the eastern side of the HDR and the NHDR, is associated with three terranes. From west to east, they are the Bronson-Hill Anticlinorium(2), Medial New England(1), and the Putnam-Nashoba Avalon(9). The Bronson Hill Anticlinorium (2) contains rocks of the Iapetus volcanic arc. These rocks are distorted by domes and basins. The western border of this terrane is defined by Late Paleozoic and Mesozoic faults (e.g. D'Annolfo, 1992). The Putnam-Nashoba Avalon terrane (9) contains Late Ordovician through Silurian granitic and dioritic plutons. On the west, it is bounded by the Clinton-Newbury fault zone. On the east, it is bounded by the Honey Hill-Lake Char-Bloody Bluff fault zone (Hatcher, Thomas, and Viele; 1989).

5. Lateral Variation in Group Velocity

5.1 Determining Lateral Velocity Variation Using Tomography

In this study, tomography is used to determine lateral variation of R_g group velocities. To illustrate how tomography works, I have constructed a simple tomographic problem with a known solution and a simple block structure. The known solution and block structure are shown in Figure 16. There are two blocks (or two model parameters), so $M=2$. The study area is bounded by -0.0018° and 0° longitude and by 0° and 0.0018° latitude. This area was chosen to be near the equator because, at this latitude, the distances along the longitudinal and latitudinal lines are nearly equal. At greater latitudes, the curvature of the longitudinal lines distorts the study area so that it is no longer rectangular. There are four "observed" data values, so $N=4$. The "observed" data value(s) for each path is synthesized from the known solution and the calculated distances of the path segments in each block. The source and receiver locations, and the observed data value(s) for each path are listed in Table 3.

The source-receiver paths in Table 3 are superimposed over the simple block structure [Figure 16]. Each path is divided into path segments marked by the boundaries of each block. Paths 1, 2, and 3 are divided into two path segments. Path 4 lies entirely in block 2. Block 1 has three path segments. Block 2 has four path segments. The path segments g_{11} , g_{12} , g_{21} , g_{22} , g_{31} , g_{32} , and g_{42} are nonzero [Figure 16].

The observed travel times for paths 1 through 4, d_i , can now be expressed in

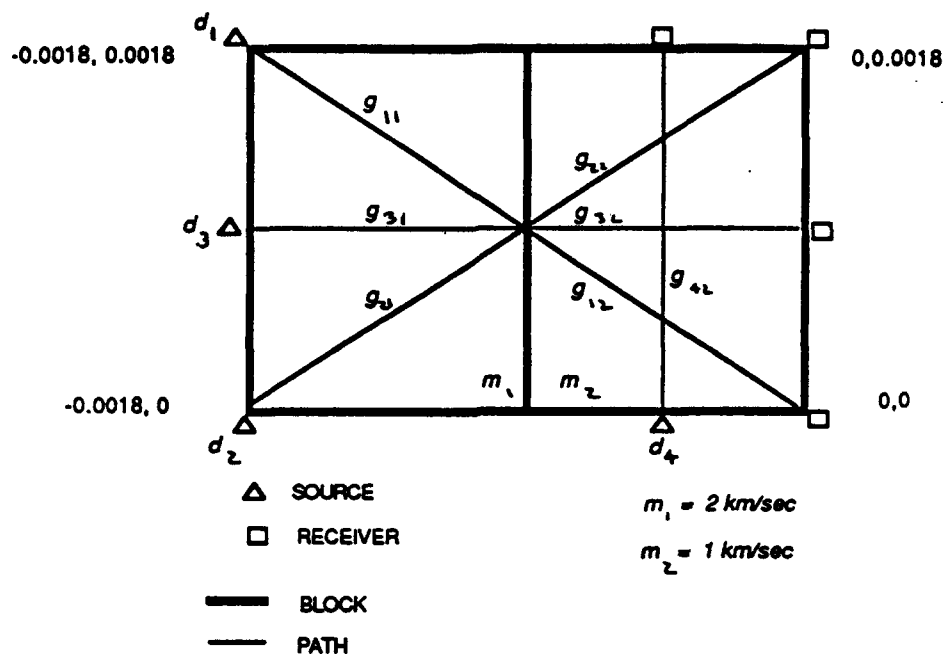


Figure 16 A synthetic example with a known solution and a simple 2x1 block structure.

Path	Data Value	Source (in decimal degrees)		Receiver (in decimal degrees)		"Observed" Travel Time (in seconds)
		Longitude	Latitude	Longitude	Latitude	
1	1	0.0001	0.0001	0.0179	0.0179	2.092
2	2	0.0001	0.0179	0.0179	0.0001	2.092
3	3	0.0001	0.0090	0.0179	0.0090	1.485
4	4	0.0030	0.0001	0.0030	0.0179	1.966

Table 3 Data values for a synthetic example.

vector notation as

$$\begin{bmatrix} d_1 \\ d_2 \\ d_3 \\ d_4 \end{bmatrix} = \begin{bmatrix} g_{11} & g_{12} \\ g_{21} & g_{22} \\ g_{31} & g_{32} \\ g_{41} & g_{42} \end{bmatrix} \begin{bmatrix} m_1 \\ m_2 \end{bmatrix} \quad (5.1)$$

The model parameters, $m_1=2.0$ km/sec and $m_2=1.0$ km/sec, are an exact solution to equation 5.1. Because of the way in which this example was set up, the data values, d_1 , d_2 , d_3 , and d_4 predicted by these model parameters are equal to those that are "observed".

5.2 Inverse Theory

Equation 2.8 is

$$\mathbf{d} = \mathbf{G} \mathbf{m} \quad (5.2)$$

where

\mathbf{d} = data vector
 \mathbf{m} = model parameter vector, and
 \mathbf{G} = kernel matrix.

Inverse theory is used to estimate the model vector that satisfies this equation. The data values are inverted and the model parameters are estimated in the following way:

$$\mathbf{m} = \mathbf{G}^{-*} \mathbf{d}, \quad (5.3)$$

where \mathbf{G}^{-*} is called the generalized inverse.

Inversion is an iterative procedure [Figure 17]. Each block is assigned the same initial slowness, m_i , and the observed data are read into the vector d . An initial prediction of the travel times, d' , is determined from $d' = Gm$. The difference between the predicted data and the observed data, Δd , is determined from the equation

$$\Delta d = d - d'. \quad (5.4)$$

The "natural generalized inverse" or the "weighted damped least squares" inverse, $G^{\#}$, is calculated. The change in the initial model, Δm , is the difference between the initial model m , and the new model, m' . This difference is expressed as

$$\Delta m = m - m' \quad (5.5)$$

where

$$\begin{aligned} m &= G^{\#} d \\ m' &= G^{\#} d' \end{aligned} \quad (5.6)$$

It follows that Δm can be expressed as

$$\begin{aligned} \Delta m &= G^{\#} d - G^{\#} d' \\ \Delta m &= G^{\#} (d - d') \\ \Delta m &= G^{\#} \Delta d \end{aligned} \quad (5.7)$$

In the final iteration, the model vector should appropriately predict the observed data

vector and should be a solution of $d=Gm$.

Ideally, the model vector in the final iteration is an exact solution, and the data vector predicted by $d=Gm$ is exactly what is observed. This condition is called "zero prediction error". However, in the actual application of inverse theory, the predicted data vector is close to but, of course, not exactly what is observed. The model parameters are estimated and the prediction error is nonzero.

5.2.1 The Generalized Inverse

The method chosen to find the generalized inverse depends on the kind of tomographic problem that is being solved. A tomographic problem is described as overdetermined, underdetermined, even-determined, or mix-determined. This description is based on the density and distribution of paths, generally termed the path information. If there is not enough path information within the study area to uniquely determine all of the model parameters, the problem is underdetermined. Where there is more than enough path information to exactly determine all model parameters, the problem is overdetermined. Where there is just enough path information to determine an exact solution for every model parameter, the problem is even-determined. Often, one model parameter is constrained by too little information while another is constrained by too much information. Yet another model parameter may be constrained by just enough information. In this situation, the problem is mix-determined.

A problem is underdetermined when either the path information is distributed sparsely and unevenly or when each block in the block structure shares identical path information. In the first case, one or more blocks do not contain any path segments or

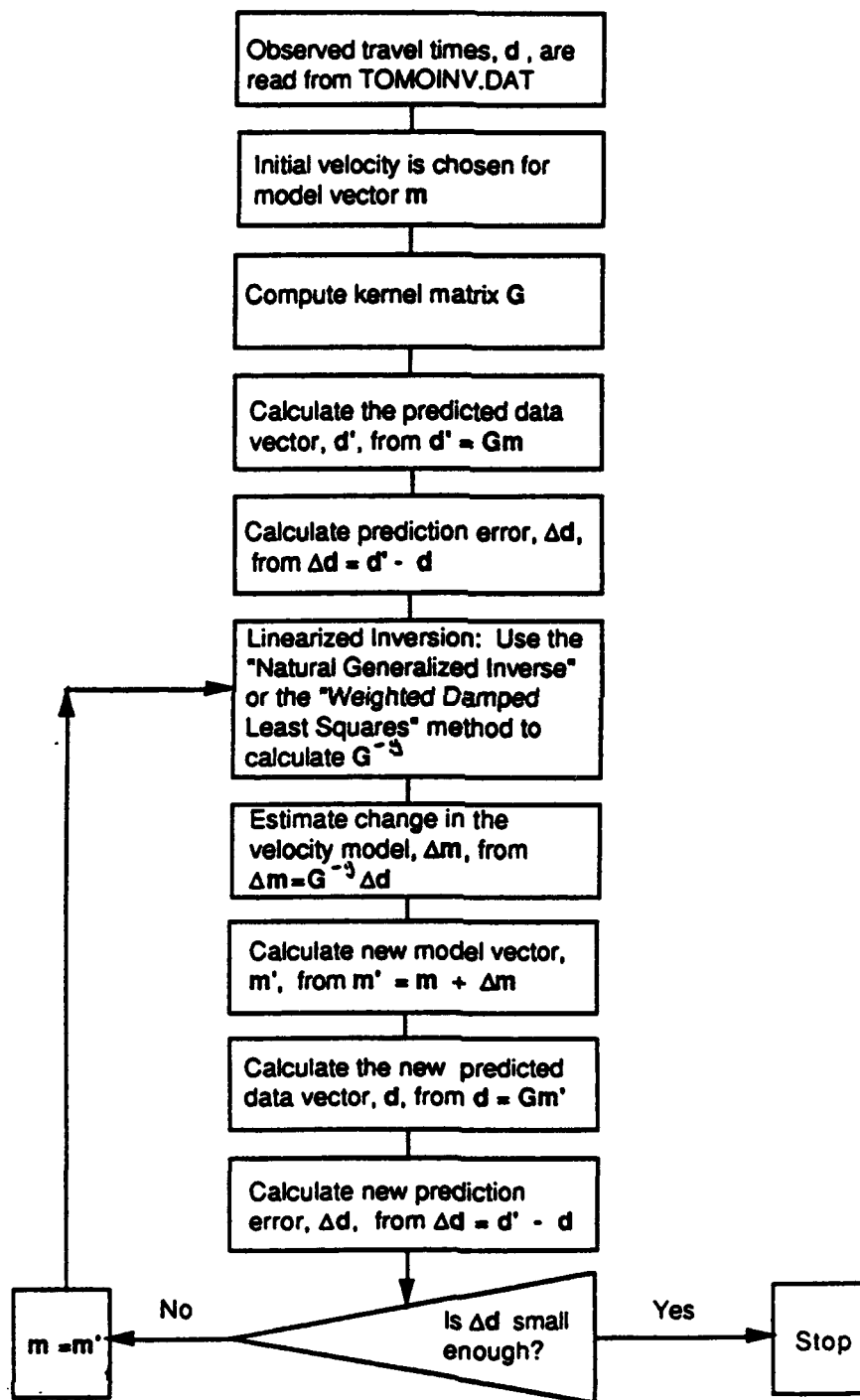


Figure 17 Flow chart of the computer program used for tomographic inversion.

the lengths of the segments are relatively small compared to the longest possible path segment in a block. As a result, the model parameters for these blocks are completely unconstrained by the path information

The two block example of a 1 km by 1 km study area illustrates how the equation $\mathbf{d}=\mathbf{Gm}$ is affected by little or no path information in at least one block. Suppose that the data vector consists of only the travel time for the fourth data value in Table 3, i.e. the one-dimensional "vector" $[d_4]$. The path is superimposed over the simple block structure [Figure 18]. The equation $\mathbf{d}=\mathbf{Gm}$ is written as

$$d_4 = g_{41} * m_1 + g_{42} * m_2, \quad (5.8)$$

where $g_{42}=0$. In this case, m_1 is not uniquely determined. In fact it is completely unconstrained by the data.

In the second case where every block shares identical path information, the group velocities are constrained to some extent, but are not unique. The two block example illustrates how $\mathbf{d}=\mathbf{Gm}$ is affected by identical path information. Suppose that the data vector consists of the travel times for the first three data values in Table 3, i.e. the three-dimensional vector $[d_1, d_2, d_3]$. The paths are superimposed over the simple block structure [Figure 19]. The equation $\mathbf{d}=\mathbf{Gm}$ is written as

$$\begin{aligned} d_1 &= g_{11} * m_1 + g_{12} * m_2 \\ d_2 &= g_{21} * m_1 + g_{22} * m_2 \\ d_3 &= g_{31} * m_1 + g_{32} * m_2 \end{aligned} \quad (5.9)$$

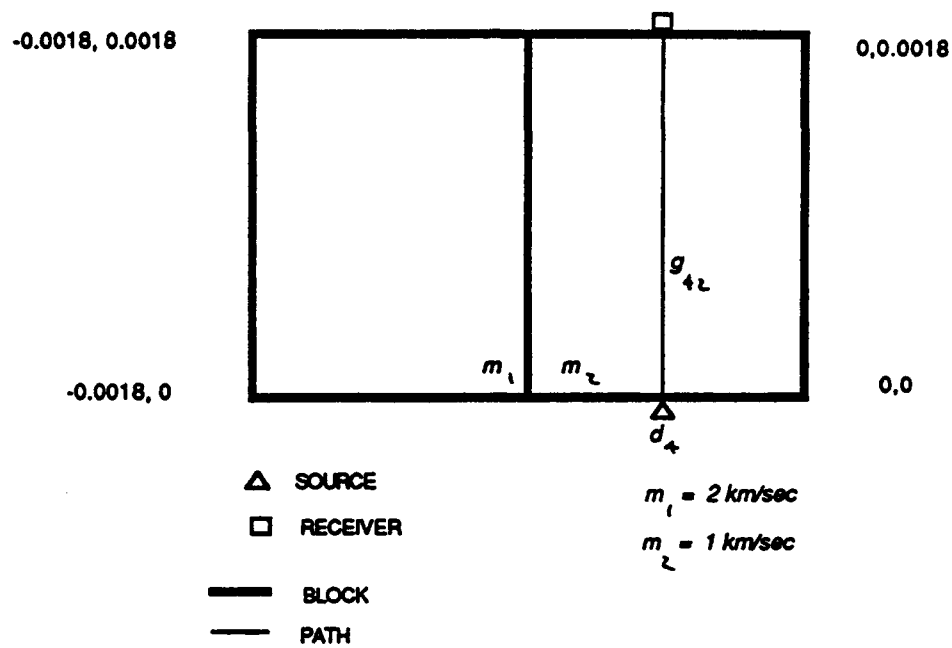


Figure 18 The synthetic example using only one data value, d_4 .

where

$$\begin{aligned}g_{11} &= g_{12} \\g_{21} &= g_{22} \\g_{31} &= g_{32}.\end{aligned}$$

Each block contains the same path information. Since there is no information to distinguish one model parameter from the other, the model parameters are merely the average of the known model parameters and equal to 1.5 km/sec.

A tomographic problem is overdetermined when the density and distribution of path segments are high in every block. In this case, there is more than enough information to determine the slowness for each block. The two block example illustrates how $d=Gm$ is affected by too much path information. Suppose that there are seven data values. Figure 20 shows these paths superimposed over the block structure. The equation $d=Gm$ is rewritten as

$$\begin{aligned}d_1 &= g_{11} * m_1 + g_{12} * m_2 \\d_2 &= g_{21} * m_1 + g_{22} * m_2 \\d_3 &= g_{31} * m_1 + g_{32} * m_2 \\d_4 &= g_{41} * m_1 + g_{42} * m_2 \\d_5 &= g_{51} * m_1 + g_{52} * m_2 \\d_6 &= g_{61} * m_1 + g_{62} * m_2 \\d_7 &= g_{71} * m_1 + g_{72} * m_2\end{aligned}\tag{5.10}$$

Clearly each block is defined by more than enough path segments. A problem can also be overdetermined in the sense that path segments within a block provide conflicting information. If the observed data values are all synthesized to be an exact solution, the prediction error is zero. In the actual application of this method, the observed data

values will, of course, have been measured with some error. In this case, one solution cannot possibly satisfy every equation exactly, and the resulting solution has a nonzero prediction error for at least one data value.

The most common type of tomographic problem considered in this study is the mix-determined problem. The data vector used for study area A of SNE contains approximately 130 observed data values for the paths shown in Figure 21(A). The data vector used for study area B of SNE contains approximately 50 observed data values for the paths shown in Figure 5.6(B). The paths for both study areas are unevenly distributed. The block structures chosen for these study areas define a tomographic problem where some blocks are overdetermined and others are underdetermined.

Two approaches that are used to find the generalized inverse (and in turn the solution for the model parameters) are to calculate the "natural generalized inverse" and to calculate the "weighted damped least squares inverse". In the case of the natural generalized inverse, the underdeterminacy and overdeterminacy of the problem are dealt with separately. In the case of the least squares inverse, the underdeterminacy and overdeterminacy are dealt with simultaneously.

The Natural Generalized Inverse

The natural generalized inverse is calculated using the singular value decomposition (SVD) method. Using the vector space formulation of the inversion problem and the notation of Menke (1984), the kernel matrix G can be written as

$$G = U \Lambda V^T \quad (5.11)$$

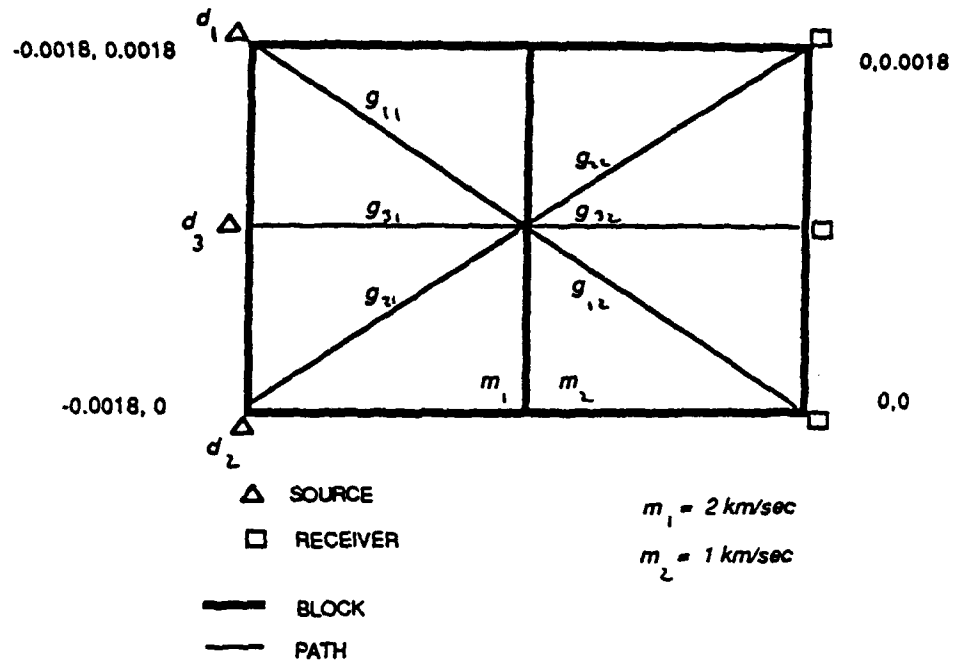


Figure 19 The synthetic example using only three data values, d_1 , d_2 , and d_3 .

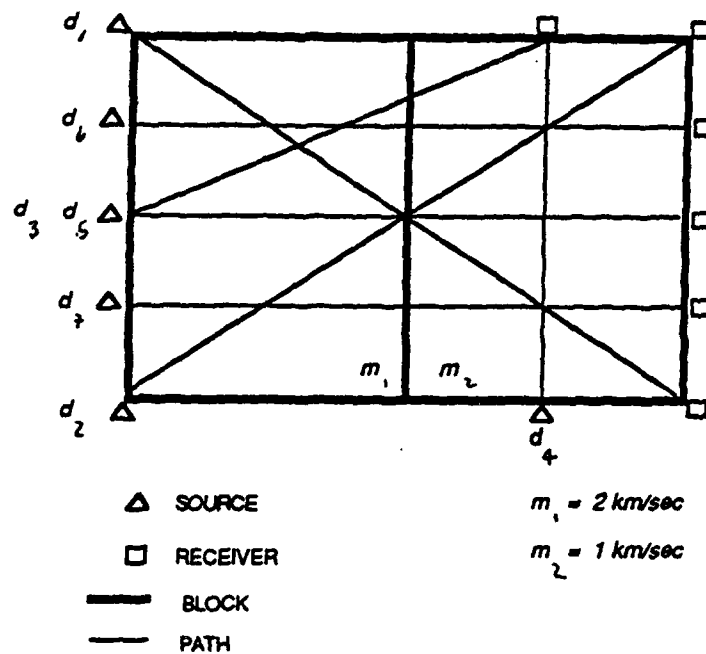
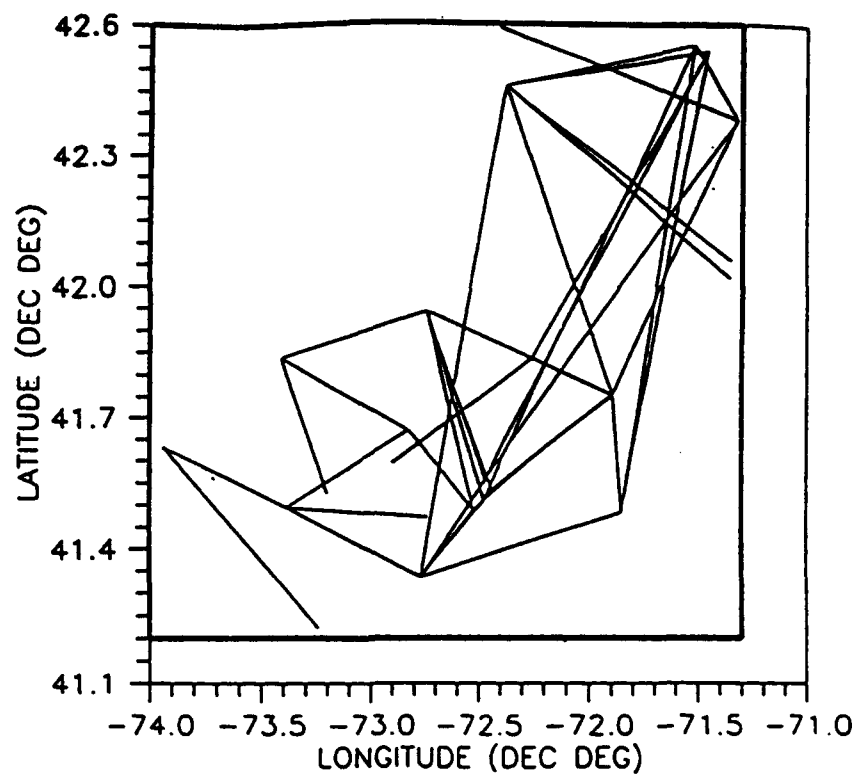


Figure 20 The synthetic example using seven data values.

(A)



(B)

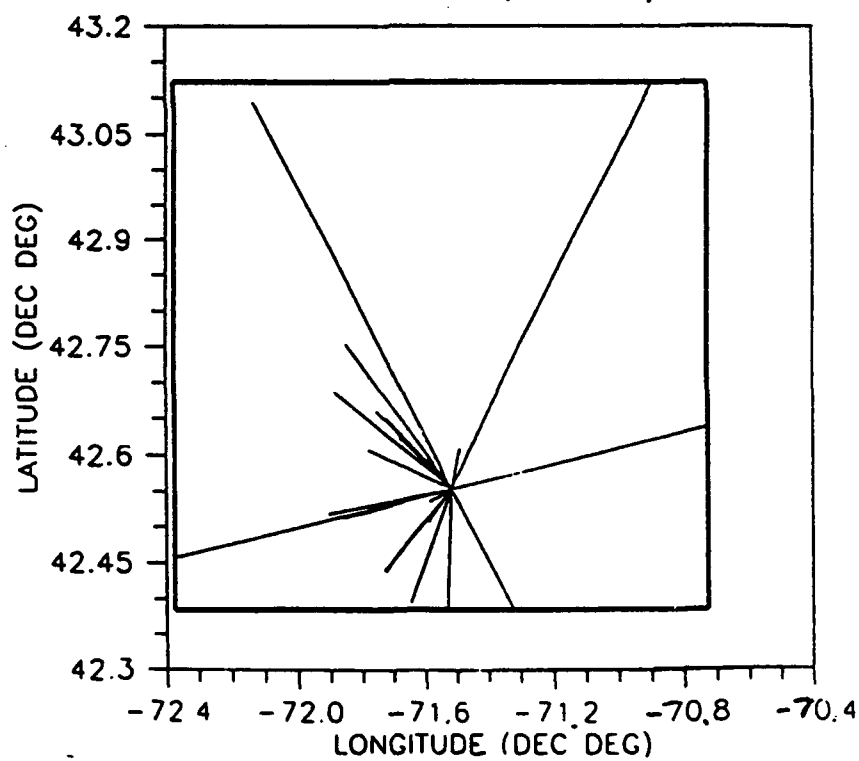


Figure 21 Path information (unevenly distributed) at a period of 0.7 sec for (a) study area A and (B) study area B.

Path	Data Value	Source		Receiver		"Observed" Travel Time (in seconds)
		Longitude (in decimal degrees)	Latitude (in decimal degrees)	Longitude (in decimal degrees)	Latitude (in decimal degrees)	
1	1	0.0001	0.0001	0.0179	0.0179	2.092
	2	0.0001	0.0001	0.0179	0.0179	2.301
	3	0.0001	0.0001	0.0179	0.0179	1.883
2	4	0.0001	0.0179	0.0179	0.0001	2.092
	5	0.0001	0.0179	0.0179	0.0001	2.301
	6	0.0001	0.0179	0.0179	0.0001	1.883
3	7	0.0001	0.0090	0.0179	0.0090	1.485
	8	0.0001	0.0090	0.0179	0.0090	1.633
	9	0.0001	0.0090	0.0179	0.0090	1.336
4	10	0.0030	0.0001	0.0030	0.0179	1.966
	11	0.0030	0.0001	0.0030	0.0179	2.163
	12	0.0030	0.0001	0.0030	0.0179	1.769

Table 4 Data values for the synthetic example with errors that one might expect in a practical case.

where

U = eigenvectors spanning the data space $S(d)$

Λ = $N \times M$ diagonal eigenvalue matrix, and

V = eigenvectors spanning the model parameter space $S(m)$.

The diagonal eigenvalues of Λ are called singular values and are arranged in decreasing order.

The equation $d = Gm$ contains data values that in general constrain some or all of the model parameters. These combinations reside in the vector space $S_p(m)$. The part which contains no information resides in the vector space $S_0(m)$. The number of nonzero eigenvalues, p , indicates the number of model parameters that are constrained by the observed data vector. By the definition of a mix-determined problem, p is less than the number of model parameters M . By the definition of an overdetermined problem, p is equal to M . The kernel matrix G can be defined more specifically as

$$G = U_p \Lambda_p V_p^T \quad (5.12)$$

The natural generalized inverse, $G^{\#}$, can be expressed as

$$G^{\#} = V_p \Lambda_p^{-1} U_p^T \quad (5.13)$$

The model parameters are then estimated by the equation $m = G^{\#}d$.

Our simple example of a 1 km by 1 km study area would be an overdetermined

problem if we include all four data values in Table 3, and would be mix-determined problem if we include only the fourth data value in Table 3. First, consider the overdetermined problem. Since the vector space $S_p(m)$ spans the entire model space V_p , one would expect that there would be two nonzero eigenvalues and p is equal to M . The two eigenvalues are 3.47 and 1.25, i.e. both are greater than zero. Second, consider the mix-determined problem. The model parameters m_1 is underdetermined while the model parameter m_2 is even-determined. One would expect that there would be only one nonzero eigenvalue and $p=1$. The only non-zero eigenvalue is 1.97.

The Weighted Damped Least Squares Solution

In the second method, a weighted damped least squares solution is estimated. This method uses added information, or a priori information, to minimize the negative effects of underdeterminacy and conflicting path information. Here the generalized inverse includes a weighting model matrix W_m , a weighting data matrix W_e , and a damping constant ε . The derivation begins with the solution of an entirely overdetermined problem.

Where the problem is entirely overdetermined, there exists a least squares solution that minimizes the data prediction E . The estimated solution can be expressed as the value of m that satisfies the following equation.

$$E = e^T e = (d - G m)^T (d - G m). \quad (5.14)$$

To minimize E , its derivative is calculated and set to zero. It follows that the least squares solution for $d=Gm$ is

$$\mathbf{m}^{\text{est}} = [\mathbf{G}^T \mathbf{G}]^{-1} \mathbf{G}^T \mathbf{d}. \quad (5.15)$$

When the problem is mix-determined, the underdeterminacy of the problem is minimized while estimating a solution for that part which is overdetermined. Instead of just minimizing the data prediction error E , a solution can be estimated that minimizes E and weights the solution error, or solution length, L , of the underdetermined model parameters. The solution error can be expressed as

$$L = \mathbf{m}^T \mathbf{m}. \quad (5.16)$$

The solution must minimize some combination of E and L . Using the notation of Menke (1984), this condition is expressed in terms of the function $\Phi(\mathbf{m})$ where

$$\Phi(\mathbf{m}) = E + \epsilon^2 L = \mathbf{e}^T \mathbf{e} + \epsilon^2 \mathbf{m}^T \mathbf{m}. \quad (5.17)$$

The weighting factor, or the damping constant, ϵ , weights the importance of the solution error. Using an appropriate value of ϵ , the damped least squares solution is given by

$$\mathbf{m}^{\text{est}} = [\mathbf{G}^T \mathbf{G} + \epsilon^2 \mathbf{I}]^{-1} \mathbf{G}^T \mathbf{d} \quad (5.18)$$

The solution error L is a measure of how "simple" a solution is. Some problems require that the solution be simple based on specific a priori information. This a priori information is given by the matrix \mathbf{F} . For example, suppose group velocities were

required to change slowly across the study area. In this case, F would represent the first derivative, which can be estimated by

$$F = \begin{bmatrix} -1 & 1 & 0 & \cdot & \cdot & 0 \\ 0 & -1 & 1 & \cdot & \cdot & 0 \\ \cdot & \cdot & \cdot & \cdot & \cdot & \cdot \\ 0 & 0 & 0 & 0 & -1 & 1 \end{bmatrix} \quad (5.19)$$

The weighting matrix W_m weights the solution error so that it satisfies this a priori requirement. W_m is expressed as

$$W_m = F^T F. \quad (5.20)$$

The solution error L is rewritten as

$$L = m^T W_m m \quad (5.21)$$

The prediction error E can also be weighted by a matrix W_e . In this case, each observed data point is weighted based on a priori information such as the accuracy with which each observation was measured. If all observations are weighted equally, W_e is the identity matrix. The prediction error E is

$$E = e^T W_e e \quad (5.22)$$

The solution that weights both the data prediction and solution error, and damps

the underdeterminacy of the problem is called the weighted damped least squares solution. It is given as

$$\mathbf{m}^{\text{est}} = \mathbf{m} + [\mathbf{G}^T \mathbf{W}_d \mathbf{G} + \epsilon^2 \mathbf{W}_m]^{-1} \mathbf{G}^T \mathbf{W}_d [\mathbf{d} - \mathbf{G}\mathbf{m}] \quad (5.23)$$

where \mathbf{m} is the previous estimate of the solution. If \mathbf{W}_m and \mathbf{W}_d are equivalent to the identity matrix, the equation reduces to that of the damped least squares (Menke, 1984).

5.3 The Solution Obtained from a Tomographic Inversion

The solution of $\mathbf{d}=\mathbf{G}\mathbf{m}$ yields a set of model parameters, $\mathbf{m}=[m_1, \dots, m_M]^T$.

Questions pertinent to this solution are

1) How are errors in the observed data mapped to the model parameters?

and

2) How uniquely is each model parameter determined with respect to all other model parameters?

5.3.1 Errors Mapped from the Data to the Solution

The answer to the first question is quantified in terms of the model covariance matrix, $[\text{cov } \mathbf{m}]$. The model covariance matrix is defined by Menke (1984) as

$$[\text{cov } \mathbf{m}] = \mathbf{G}^{-\epsilon} [\text{cov } \mathbf{d}] \mathbf{G}^{-\epsilon T} \quad (5.24)$$

where $[\text{cov } \mathbf{d}]$ is the data covariance matrix. In this study, the data values are assumed to be uncorrelated and each observation is assumed to have an equal variance σ_d^2 .

Therefore, $[\text{cov } \mathbf{d}]$ is written as

$$[\text{cov } d] = \begin{bmatrix} \sigma_d^2 & 0 & 0 & \cdot & \cdot & 0 \\ 0 & \sigma_d^2 & 0 & \cdot & \cdot & 0 \\ \cdot & \cdot & \cdot & \cdot & \cdot & \cdot \\ 0 & 0 & 0 & 0 & 0 & \sigma_d^2 \end{bmatrix} \quad (5.25)$$

The model covariance matrix, $[\text{cov } m]$, describes how the variance assigned to the data values is mapped to the model parameters. The variance of m_j is given by element j in row j of $[\text{cov } m]$. The paths represented by the data values cross one or more blocks (model parameters). The variance of the observed data for these paths are then distributed among these blocks (model parameters). The remaining elements of row j describe how the variance of the data values is mapped to the remaining model parameters with respect to model parameter j . If the assumptions made about $[\text{cov } d]$ are valid, the diagonal element in row j of $[\text{cov } m]$ is larger than all other elements of row j .

In our example, the natural generalized inverse is used to estimate the model parameters from the data values listed in Table 5.1. Since the observed data values have been synthetically calculated to fit the model exactly, the variance, σ_d^2 , of the data values is 0. All elements of the model covariance matrix are 0. Therefore, the variance of each model parameter is 0.

However, inherent to each observation is an error with which it was measured. In order to illustrate the effect of errors in the data values, I have re-calculated the "observed" data using errors that are on the order of what one would expect in a practical situation (Table 5.2). The variance of the data values, σ_d^2 , is equal to 0.1658

sec².

Using the natural generalized inverse, the model covariance matrix is

$$[\text{cov } \mathbf{m}] = \begin{bmatrix} 0.026 & -0.014 \\ -0.014 & 0.014 \end{bmatrix}. \quad (5.26)$$

The variance for m_1 is 0.026 sec², the diagonal element of row 1. The other element in row 1 indicates how the variance of the data values for all four paths is mapped to the model parameter m_2 with respect to m_1 . The variance for m_2 is 0.014 sec², the diagonal element of row 2. The other element in row 2 indicates how the variance of the data values for the first three paths are mapped to the model parameter, m_1 . The assumptions made about [cov d] appear to be valid because the diagonal element of each row is the largest with respect to the other elements in the row.

5.3.2 Resolution of a Solution

The answer to the second question is characterized by the model resolution matrix

R. One can envision a model vector, \mathbf{m}_{true} , that exactly solves the equation

$$\mathbf{d}_{\text{obs}} = \mathbf{G} \mathbf{m}_{\text{true}}. \quad (5.27)$$

where \mathbf{d}_{obs} is the vector of observed data values. R indicates how close the estimated model parameters, \mathbf{m}_{est} , are to \mathbf{m}_{true} . R is an M x M matrix defined as

$$\mathbf{R} = \mathbf{G}^{-1} \mathbf{G}. \quad (5.28)$$

Each row j of R describes how well model parameter j is resolved with respect to all other model parameters. Where a model parameter is perfectly resolved, the diagonal element of row j is equal to 1 and all other elements of row j are equal to 0. Thus when all model parameters are perfectly resolved, R is the identity matrix I . If a diagonal element is not equal to 1, the values across the row are weighted averages of the true model parameters.

In the example shown in Figure 16, an estimate of the true model parameters are $m = [2.0, 1.0]^T$. The observed data for each path is described by $[d_1, d_2, d_3, d_4]$ (Table 3), which are superimposed over the simple block structure. Using the natural generalized inverse, the resolution matrix is the identity matrix I . Each block is well resolved and each model parameter is uniquely determined.

Suppose that each block shared the same path information ($d = [d_1, d_2, d_3]$). As discussed previously, this problem is underdetermined. Using the natural generalized inverse, R is

$$R = \begin{bmatrix} 0.5 & 0.5 \\ 0.5 & 0.5 \end{bmatrix} \quad (5.29)$$

The resolution of both model parameters is 0.5, the diagonal element of each row. This indicates that the model parameters obtained by the inversion procedure are actually an average of the known model parameters for both blocks.

5.4 Program Development

Tomographic methods were used in a study by Zhu (1991) to determine the

seismic P-wave velocity structure beneath northern New England. He developed a computer program written in FORTRAN called TOMONET. TOMONET read in P wave refraction data and estimated P wave velocities for a multi-layered model, where each layer was divided into equally sized blocks by the same block structure. A detailed discussion of the development of TOMONET is given in Zhu (1991).

One of the options in TOMONET is the tomographic inversion of direct P wave travel times. Direct P wave velocities are estimated for a single layer model because the direct P wave travels horizontally across the structure. First the study area is divided into equally sized blocks and the paths represented by the observed direct P wave travel times are superimposed over the block structure. The P wave velocity is estimated for each block by using the SVD method and the natural generalized inverse.

This same option can be used to estimate Rg group velocities at a specific period because Rg waves also travel horizontally. The observed travel times of direct P waves are replaced by observed travel times of Rg waves at a specific period. Using the single layered model, TOMONET is able to estimate Rg group velocities at a specific period. These group velocities are analogous to the P wave velocities estimated for a single layer.

However, in order to adapt the program to this study, I have modified TOMONET to address 1) specific problems encountered in the tomographic inversion of Rg travel time data, and 2) details about tomographic inversion that are not considered by Zhu (1991). The computer program SURFTOMO contains some of the original source code in TOMONET as well as the following modifications.

First, the program code in SURFTOMO that pertains to the tomographic inversion of refraction data has been removed, leaving only the program code that allows for the tomographic inversion of observed direct P wave travel times. Also, the format of the input file read in by TOMONET has been changed. The only variables that are used in the input file are the source and receiver locations, and the observed Rg travel times.

Second, SURFTOMO computes the boundaries of the study area to be 0.0001 km outside of the minimum and maximum longitude and 0.0001 km outside of the minimum and maximum latitude of all paths represented by the data set. SURFTOMO then provides the opportunity for the study area to be specified otherwise by the computer user. Only those paths whose source and receiver are within the study area are included in the tomographic inversion.

Third, more inversion methods are available in SURFTOMO for the tomographic inversion of observed Rg travel times than were available in the original TOMONET program. The inversion method for which the code in TOMONET is written is the SVD method. Modifications have been made to this code and included in SURFTOMO. Furthermore, the code for other inversion methods in addition to the SVD method is included in SURFTOMO.

The SVD method requires the definition of what is considered a nonzero eigenvalue (i.e. how small must an eigenvalue be to be considered as "zero"). In TOMONET, an eigenvalue is considered to be nonzero if it is greater than the fraction 0.00001 of the largest eigenvalue. SURFTOMO allows the computer user to choose this percentage since this percentage should be allowed to change with each tomographic

inversion.

Another inversion method that can be used to solve a tomographic problem is the "weighted damped least squares" method. In TOMONET, the program code for the least squares method is written but not operational. In SURFTOMO, the original code from TOMONET for the least squares solution is rewritten and operating. In addition SURFTOMO includes the choice of the "weighted damped least squares solution".

Finally, the "credibility function" in TOMONET (see Zhu, 1991) has been replaced by the model covariance and resolution matrices in SURFTOMO. These matrices allow the computer user to interpret each group velocity in the solution in terms of the error and resolution with which each group velocity was estimated. These matrices are calculated for the SVD method and for the weighted damped least squares method.

6. Vertical Variation in the Seismic Velocity Structure

The maximum likelihood method (Menke, 1984; Reiter et al., 1988) is used to invert the Rg group velocity dispersion results to obtain models of the vertical variation of the shear wave velocity structure. This inversion involves solving the equation $\Delta d = G \Delta m$, similar to the case of the tomographic inversion, but in this case

$$\Delta d = (\text{observed group velocities}) - (\text{theoretical dispersion calculated for a starting model})$$

G = a matrix consisting of partial derivatives of group velocity with respect to the starting model parameters, and

Δm = the correction to the previous solution.

As in the previous cases, the solution to this problem is

$$\Delta \mathbf{m} = \mathbf{G}^{-\mathbf{t}} \Delta \mathbf{d} \quad (6.1)$$

but, in this case, $\mathbf{G}^{-\mathbf{t}}$ is the maximum likelihood inverse. The maximum likelihood inverse which is written as (Menke, 1984)

$$\mathbf{G}^{-\mathbf{t}} = (\mathbf{G}^T [\text{cov } \mathbf{d}]^{-1} \mathbf{G} + [\text{cov } \mathbf{m}]^{-1})^{-1} \mathbf{G}^T [\text{cov } \mathbf{d}]^{-1}. \quad (6.2)$$

The problem is solved in an iterative manner in which we begin by assuming a starting model \mathbf{m}_0 and use the maximum likelihood inverse to calculate $\Delta \mathbf{m}_1 = \mathbf{m}_1 - \mathbf{m}_0$. The starting model is then updated, and a revised \mathbf{G} is calculated for the revised model. The maximum likelihood inverse is used again to revise the model, and this procedure is repeated iteratively until a theoretical dispersion curve is obtained that matches the observed data to some desired degree of precision.

The details of the maximum likelihood inverse are discussed in Menke(1984) and Reiter et al. (1988). An essential feature of the maximum likelihood inverse are that it provides a way of balancing the extent to which *a priori* information about the model and the data variances are weighted in the solution. If the data values and model parameters are uncorrelated (as is assumed in this analysis), the covariance matrices are diagonal, with

$$[\text{cov } \mathbf{d}] = \sigma_d^2 \mathbf{I} \quad (6.3)$$

and

$$[cov\ m] = \sigma_m^2 I \quad (6.4)$$

Substituting equation 6.3 and 6.4 into equation 6.2, we have

$$G^{-2} = \left(G^T G + \frac{\sigma_d^2}{\sigma_m^2} I \right)^{-1} G^T. \quad (6.5)$$

Thus, when the data and model parameters are uncorrelated, the effect of including the inverse of the covariance matrices in equation 6.2 is to damp the inverse operator, similar to the case of the damped least squares (see Menke, 1984). The amount of damping is dependent on the ratio of the data and model variances. Making the *a priori* estimate of the model variance small has the effect of inhibiting the movement of the solution away from the initial model. In a similar manner, making the *a priori* estimate of the data variance small has the effect of forcing the solution to fit the observed data closely.

7. Data Analysis

7.1 The Determination of Lateral Variation in Group Velocity

Lateral variation is determined using tomographic inversion. First the observed travel times are obtained from seismograms whose source and receiver are within the study area. These travel times are organized into data sets, each associated with a distinct period. The variance, σ_d^2 , with which the observed travel times in a data set are

measured is estimated. The observed travel times are read by SURFTOMO. A block structure is chosen for a particular study area. Based on the tomographic problem corresponding to the data values and chosen block structure for the study area, an appropriate inversion technique is selected and the observed travel times are inverted to yield a set of group velocities (model parameters) at a specific period for the study area. Finally, each set of group velocities and the variance and resolution with which they are estimated is interpreted. The extent of lateral variation within the study area is then discussed.

7.1.1 Preparation of Observed Rg Travel Times for Tomographic Inversion

First, observed Rg travel times at a series of discrete periods specified for the study area are prepared in a format required by SURFTOMO. Observed Rg travel times at a specific period comprise one data set. Each data set has been prepared from seismograms whose source and receiver are located within the study area. Within each data set, many paths are represented. Because several events may have occurred at one source and have been recorded at the same receiver, a particular path may be represented by more than one travel time.

The quality of each seismogram is evaluated before it is used in this study. Many factors affect the quality of a seismogram and the quality of the observed Rg travel time results. A rigorous discussion of these factors and a detailed assessment of the quality of a seismogram is beyond the scope of this study. However, two simple requirements for a seismogram included in this study are 1) clearly identifiable P, S, and Rg waveforms, and 2) a signal to noise ratio that is fairly high based on inspection of the

seismogram. In cases where a seismogram has been partly processed in previous studies, it is assumed to have met these two requirements.

The seismograms are processed in four steps. First, the arrival time of the P and S waves are selected for each seismogram. The location of the event that generated each seismogram is confirmed and the origin time is estimated from the selected arrival times. Second, group velocities for the period range specified for the study area are calculated from each seismogram. Third, these group velocities are converted to observed travel times. Finally, these observed travel times are organized into data sets, each of which is associated with a specific period.

Study Area A

Observed travel times for study area A [Figure 14] have been prepared from seismograms generated by quarry blasts and shallow focus earthquakes. The observed Rg travel times have been obtained from four sets of seismograms. I have processed the seismograms of the first and second set of seismograms through all four steps. The third set of seismograms have been processed through step two in a previous study by Kafka (1990). I have processed these seismograms through the last two steps. The fourth set of seismograms have been processed through step three in other previous studies (Kafka and Dollin, 1985; Saikia et al., 1990; and Gnewuch, 1987). I have processed these seismograms through the last step.

The seismograms in the first set have been recorded by the Geophysical Data Acquisition System (GDAS) across a local array in the area surrounding Weston Observatory. A more complete description of the GDAS array is given in Kafka and

Jacobson-Carroll (1992). At the time the seismograms were recorded, the array consisted of seven field stations at sites A through G (Kafka and Jacobson-Carroll, 1992) located within 0.25 km of the main recording piers at Weston Observatory. Quarry blasts at the San-Vel/Lonestar Quarry in Littleton, MA, have generated all of these seismograms. The location of each station in the local array is within about 0.25 kilometers of the NESN station WES. The location of the San-Vel/Lonestar Quarry is measured to within approximately 0.5 kilometers. Therefore the location of WES (Table 5) is assumed to be adequate for the location of each station in the local array.

Seismograms from four events recorded across the GDAS array are included in this study. In the case of these four events, each had generated at least eight seismograms. The location and average origin time for each event is listed in Table 6(A).

In the first step, the arrival times of the P wave were estimated from seismograms generated by each event. The travel time, t , was estimated using the equation (D'Annolfo, 1992)

$$t = 0.171 x + 0.151 \quad (7.1)$$

where x is the distance from the source to the receiver. The distance, calculated by SURFTOMO, from the San-Vel/Lonestar Quarry to Weston Observatory is 25.0 km. From equation 7.1, a travel time of 4.4 sec was calculated. For all seismograms generated by each event, the travel time was subtracted from each arrival time of the P wave, the result being a series of estimates of the origin time for each event. These estimates were averaged to give the origin time for each event.

In the second step, the group velocities for periods 0.5 to 1.5 sec were calculated from each seismogram by a computer program that estimates group velocities by using a narrow band pass filter method (Dziewonski et al., 1969). In this technique, the group velocity chosen for each period is that velocity at which the peak wave energy arrives.

In the third step, each group velocity, U_i , was converted to an observed Rg travel time, d_i , using the equation

$$d_i = \frac{g_i}{U_i} \quad (7.2)$$

where g_i is the length of the path calculated by SURFTOMO (25.0 km in this case).

The second set of seismograms have also been generated by quarry blasts at the San-Vel/Lonestar Quarry and recorded at the NESN station WES. The origin times of these quarry blasts are listed in Table 6(B). These seismograms have been processed through steps 1 through 4 in exactly the same manner as was the first set of seismograms.

The third set of seismograms has been processed through step 1 in previous studies (Kafka, 1990). The origin time and hypocenter of two shallow focus earthquakes have been estimated in Kafka (1990) and are listed in Table 6(C). The locations of the receivers, stations of the NESN, are listed in Table 5.

In step 1, the epicenter and the origin time of each earthquake was estimated by the computer program HYPO. First, the P and S wave arrival times were estimated for each seismogram generated by the earthquake. The estimation of the origin time was then made by HYPO based on the P and S arrival times, and an estimated velocity model

STATION NAME	STATION LOCATION	LONGITUDE (DEC DEG)	LATITUDE (DEC DEG)
BCT	BROOKFIELD, CT	73.3839	41.4933
BPT	BRIDGEPORT, CT	73.2422	41.2221
BVT	BALTIMORE, VT	72.5853	43.3488
DNH	DURHAM, NH	70.8948	43.1225
ECT	ELLSWORTH, CT	73.4113	41.8346
HDM	HADDAM, CT	72.5232	41.4857
IVT	IRA, VT	73.0533	43.5221
MD1	MOODUS, CT	72.4667	41.5529
MD2	MOODUS, CT	72.4337	41.5314
MD3	MOODUS, CT	72.4715	41.5066
NSC	NO STONINGTON, CT	71.8516	41.4807
PNH	PITCHER MTN, NH	72.1358	43.0942
QUA	QUABBIN, MA	72.3738	42.4566
UCT	STORRS, CT	72.2505	41.8317
WES	WESTON, MA	71.3221	42.3847
WFM	WESTFORD, MA	71.4906	42.6106
WNH	WHITEFACE MTN, NH	71.3997	43.8683

Table 5 Study area A: Stations of the New England Seismic Network (NESN).

for southern New England.

In step 2, the group velocities for periods from 0.5 to 1.5 sec were calculated from each seismogram using the narrow band pass filter analysis. The distances upon which these group velocities were based were calculated by HYPO. For the group velocities from these seismograms to be consistent with those of the first set of seismograms, each group velocity calculated on the basis of a distance obtained by HYPO, U_p , was then converted to a group velocity based on a distance obtained by SURFTOMO, U_i . The following equation was used to make this conversion.

$$U_i = \left(\frac{g_i}{g_p} \right) U_p \quad (7.3)$$

where

g_i = distance from source to receiver calculated by SURFTOMO

g_p = distance upon which the calculation of u was based

In step 3, these group velocities were converted to observed Rg travel times. The conversion of each group velocity, U_i , for the second set of seismograms to each observed travel time, d_i , was made using equation 7.2.

The fourth set of seismograms was prepared through step 2 in previous studies (Kafka and Dollin, 1985; Saikia et al., 1990; and Gnewuch, 1987), where group velocities have been calculated from each seismogram. These seismograms were all generated by quarry blasts in southern New England. The receivers, again stations of the NESN, are listed in Table 5. The location and origin times for each event are listed in Table 6(D).

EVENT	LOCATION	LOCATION CODE	DATE	ORIGIN TIME (DY:HR:MN:SEC)	* RMS (SEC)	LONGITUDE (DEC DEG)	LATITUDE (DEC DEG)
91212A	SAN-VEL QUARRY LITTLETON, MA	LTMA	7/31/92	212:18:60:12.12	0.025	71.5170	42.5540
91227B	SAN-VEL QUARRY LITTLETON, MA	LTMA	8/15/91	227:15:59:29.24	0.129	71.5170	42.5540
91234B	SAN-VEL QUARRY LITTLETON, MA	LTMA	8/22/91	234:19:29:23.05	0.014	71.5170	42.5540
91249D	SAN-VEL QUARRY LITTLETON, MA	LTMA	9/6/91	249:18:60:06.45	0.010	71.5170	42.5540

* Standard deviation of the origin times estimated by Equation 7.1.

Table 6(A) Event information recorded over the GDAS array.

EVENT	LOCATION	LOCATION CODE	DATE	ORIGIN TIME (DY:HR:MN:SEC)	LONGITUDE (DEC DEG)	LATITUDE (DEC DEG)
0801803	SAN-VEL QUARRY LITTLETON, MA	LTMA	3/21/89	080:01:40.854	71.5170	42.5540
0971832	SAN-VEL QUARRY LITTLETON, MA	LTMA	4/7/89	097:18:29:56.234	71.5170	42.5540
1041832	SAN-VEL QUARRY LITTLETON, MA	LTMA	4/14/89	104:18:29:39.814	71.5170	42.5540
1101733	SAN-VEL QUARRY LITTLETON, MA	LTMA	4/20/89	110:17:30:49.714	71.5170	42.5540
1161805	SAN-VEL QUARRY LITTLETON, MA	LTMA	4/26/89	116:18:03:30.614	71.5170	42.5540
1301814	SAN-VEL QUARRY • LITTLETON, MA	LTMA	5/10/89	130:18:11:56.194	71.5170	42.5540
1361802	SAN-VEL QUARRY LITTLETON, MA	LTMA	5/16/89	136:18:00:36.034	71.5170	42.5540
1431732	SAN-VEL QUARRY LITTLETON, MA	LTMA	5/23/89	143:17:30:06.874	71.5170	42.5540
1511805	SAN-VEL QUARRY LITTLETON, MA	LTMA	5/31/89	151:18:03:16.134	71.5170	42.5540
1561838	SAN-VEL QUARRY	LTMA	6/5/89	156:18:36:30.154	71.5170	42.5540

Table 6(B) Event information recorded at the NESN station WES.

EVENT	LOCATION	LOCATION CODE	DATE	ORIGIN TIME (DY:HR:MN:SEC)	LONGITUDE (DEC DEG)	LATITUDE (DEC DEG)
	LITTLETON, MA					
1591947	SAN-VEL QUARRY LITTLETON, MA	LTMA	6/8/89	159:19:45:15.594	71.5170	42.5540
1641904	SAN-VEL QUARRY LITTLETON, MA	LTMA	6/13/89	164:19:02:35.534	71.5170	42.5540

Table 6(B) Event information recorded at the NESN station WES.

ERVG	ERVING, MA	ERVG	6/14/84	166:20:56:33.93	0.54	72.4000	42.5900
BXBR	BOXBORO, MA	BXBR	10/15/85	288:20:00:38.64	0.40	71.4580	42.5400

* Standard deviation of the origin times estimated by HYPO.

Table 6(C) Event information taken from Kafka (1990).

EVENT	LOCATION	LOCATION CODE	DATE	ORIGIN TIME (DY:HR:MN:SEC)	** RMS (SEC)	LONGITUDE (DEC DEG)	LATITUDE (DEC DEG)
P1	G	CLINTON POINT, NY	6/7/74	158:19:45:35.40	0.050	73.9400	41.6300
P2	G	CLINTON POINT, NY	6/15/75	166:08:08:48.53	0.310	73.9400	41.6300
P3	G	CLINTON POINT, NY	10/17/75	290:19:43:30.99	0.860	73.9400	41.6300
P4	G	CLINTON POINT, NY	12/5/85	339:20:31:25.40	0.180	73.9400	41.6300
G8	G	NORTH BRANFORD, CT	6/9/86	160:14:20:00.83	0.160	72.7670	41.3330
G17	G	NORTH BRANFORD, CT	5/8/86	128:13:59:57.85	0.250	72.7670	41.3330
G19	G	NORTH BRANFORD, CT	3/17/86	076:15:45:00.47	0.240	72.7670	41.3330
D9	G	NORTH BRANFORD, CT	6/21/83	172:14:58:58.70	0.090	72.7670	41.3330
F2	G	NORTH BRANFORD, CT	4/25/84	116:16:30:01.24	0.140	72.7670	41.3330

Table 6(D) Event information taken from Dollin (1984), Saikia et al. (1986), and Gnewuch (1987).

EVENT	LOCATION	LOCATION CODE	DATE	ORIGIN TIME (DY:HR:MN:SEC)	RMS (SEC)	LONGITUDE (DEC DEG)	LATITUDE (DEC DEG)
15 G	NORTH BRANFORD, CT	NBCT	8/3/84	216:16:55:03.50	0.110	72.7670	41.3330
G12 G	NEW BRITAIN- PLAINVILLE, CT	NPCT	5/29/86	149:14:00:01.15	0.240	72.8250	41.6670
G20 G	NEW BRITAIN- PLAINVILLE, CT	NPCT	3/17/86	076:16:50:00.48	0.200	72.8250	41.6670
D-14 D	NEW BRITAIN- PLAINVILLE, CT	NPCT	?	???15:10:40.70	0.170	72.8250	41.6670
G1 G	REEDS GAP, CT	RGCT	7/20/86	201:13:24:59.45	0.200	72.7350	41.4710
G4 G	REEDS GAP, CT	RGCT	7/9/85	190:14:25:01.71	0.140	72.7350	41.4710
G5 G	REEDS GAP, CT	RGCT	8/6/85	218:14:20:00.27	0.210	72.7350	41.4710
G6 G	REEDS GAP, CT	RGCT	6/26/86	177:13:58:58.25	0.180	72.7350	41.4710
G9 G	REEDS GAP, CT	RGCT	6/6/86	157:14:14:54.76	0.210	72.7350	41.4710
G13 G	REEDS GAP, CT	RGCT	5/27/86	147:14:30:59.60	0.070	72.7350	41.4710
G15 G	REEDS GAP, CT	RGCT	5/19/86	139:15:00:00.69	0.170	72.7350	41.4710

Table 6(D) Event information taken from Dollin (1984), Saikia et al. (1986), and Gnewuch (1987).

EVENT	LOCATION	LOCATION CODE	DATE	ORIGIN TIME (DY:HR:MN:SEC)	**RMS (SEC)	LONGITUDE (DEC DEG)	LATITUDE (DEC DEG)
12 G,S	EAST GRANBY, CT	EGCT	7/19/84	201:16:04:23.60	0.140	72.7420	41.9390
D-12 D,G	EAST GRANBY, CT	EGCT	7/19/84	201:16:04:23.60	0.140	72.7420	41.9390
4 G,S	EAST GRANBY, CT	EGCT	6/3/84	155:16:18:44.15	0.280	72.7420	41.9390
2 G,S	EAST GRANBY, CT	EGCT	8/14/84	227:16:04:45.38	0.180	72.7420	41.9390
13 G,S	LITTLETON, MA	LTMA	6/11/85	162:18:47:20.10	0.220	71.5170	42.5540
17 G,S	LITTLETON, MA	LTMA	10/24/85	297:16:22:58.02	0.250	71.5170	42.5540
14 G,S	LITTLETON, MA	LTMA	8/12/85	224:16:22:55.24	0.140	71.5170	42.5540
D-8 D	SOUTH WOODBURY, CT	SWCT	?	??? :18:00:57.40	0.460	73.2000	41.5250
10 G,S	WAUREGAN, CT	WGCT	7/22/84	204:15:09:55.17	0.130	72.8890	41.7490
11 G,S	WAUREGAN, CT	WGCT	6/22/84	174:15:00:0168	0.340	72.8890	41.7490

Table 6(D) Event information taken from Dollin (1984), Saikia et al. (1986), and Gnewuch (1987).

EVENT	LOCATION	LOCATION CODE	DATE	ORIGIN TIME (DY:HR:MN:SEC)	** RMS (SEC)	LONGITUDE (DEC DEG)	LATITUDE (DEC DEG)
3	G,S WAUREGAN, CT	WGCT	7/20/84	202:15:49:58.38	0.200	72.8890	41.7490
5	G,S WAUREGAN, CT	WGCT	8/10/84	223:17:45:01.38	0.200	72.8890	41.7490
8	G,S PLAINVILLE, MA	PVMA	8/14/84	227:20:25:52.08	0.310	71.3560	41.6950
6	G,S WRENTHAM, MA	WTMA	3/27/84	087:17:29:37.86	0.100	71.3500	42.0540
18	D ROAD BLAST, CT	RBCT	?	???:16:07:27.6	0.270	72.9000	41.5920

* The group velocity information for these events was taken from Dollin (1984), Saikia et al. (1986), and Gnewuch (1987). They are abbreviated D, S, and G respectively.

** Standard deviation of the origin times estimated by HYPO.

Table 6(D) Event information taken from Dollin (1984), Saikia et al. (1986), and Gnewuch (1987).

As in the second set of seismograms, the origin time was estimated using the HYPO computer program. The arrival times of the P and S waves were chosen for each seismogram generated by the quarry blast. Each quarry blast location was confirmed with the operator at the nearest quarry. The origin time was estimated again based on the known location of the quarry.

In the second step, the group velocities were calculated for each seismogram. As in the previous set of seismograms, each calculation of group velocity was based on a distance obtained from HYPO. This group velocity, U_p , was converted to one whose calculation was based on a distance obtained from SURFTOMO. The group velocity, U_p , was then converted to U_i by equation 7.3.

In step three, these group velocities were converted to observed travel times. Equation 7.2 was used to convert each group velocity, U_i , to an observed travel time, d_i . Finally, the observed travel times for all seismograms used for study area A were organized into data files, each associated with a specific period. All observed travel times at 0.5 sec were written to a computer file A1_05.DAT. This was also done for the periods 0.7, 0.9, 1.1, 1.3, and 1.5 sec, generating data sets A1_07.DAT, A1_09.DAT, A1_11.DAT, A1_13.DAT, and A1_15.DAT respectively. The paths represented by each data set are shown in Figure 22. For future analyses of the vertical variation in shear wave velocity, the observed travel times that are represented by the path from the San-Vel/Lonestar Quarry to the NESN station WES have been written to the computer files A2_05.DAT, A2_07.DAT, A2_09.DAT, A2_11.DAT, A2_13.DAT, and A2_15.DAT. The path from the San-Vel/Lonestar quarry to WES is marked in

Figure 22.

Study Area B

The seismograms for study area B [Figure 14] were processed through the first three steps by D'Annolfo (1992). The seismograms, whose origin times are given in Table 7(B), have been generated by quarry blasts at the San-Vel/Lonestar Quarry. The receivers, whose locations are given in Table 7(A), include a few NESN stations and many field stations set up closer to the quarry.

In the third step, the group velocities taken from D'Annolfo (1992) were converted into observed travel times. As was the case with study area A, the calculations of the group velocities taken from D'Annolfo (1992) were based on distances not calculated by SURFTOMO. Therefore, each group velocity, U_p , was converted to a U_i by equation 7.3.

In the final step, the observed travel times for all seismograms were organized into data files. All observed travel times at 0.5 sec were written to a computer file B1_05.DAT. This was also done for the periods 0.7, 0.9, and 1.1 sec, generating data files B1_07.DAT, B1_09.DAT, and B1_11.DAT respectively. The paths represented by each data set are shown in Figure 23.

Errors in the Measurement of Observed R_g Travel Times

The variance corresponding to each observed R_g travel time was estimated for the tomographic inversion. A variance, σ_d^2 , is calculated for each data set and assigned to the diagonal elements of [cov d]. The variance for each data set is calculated in the following way. An initial group velocity at a specific period is assigned to every model

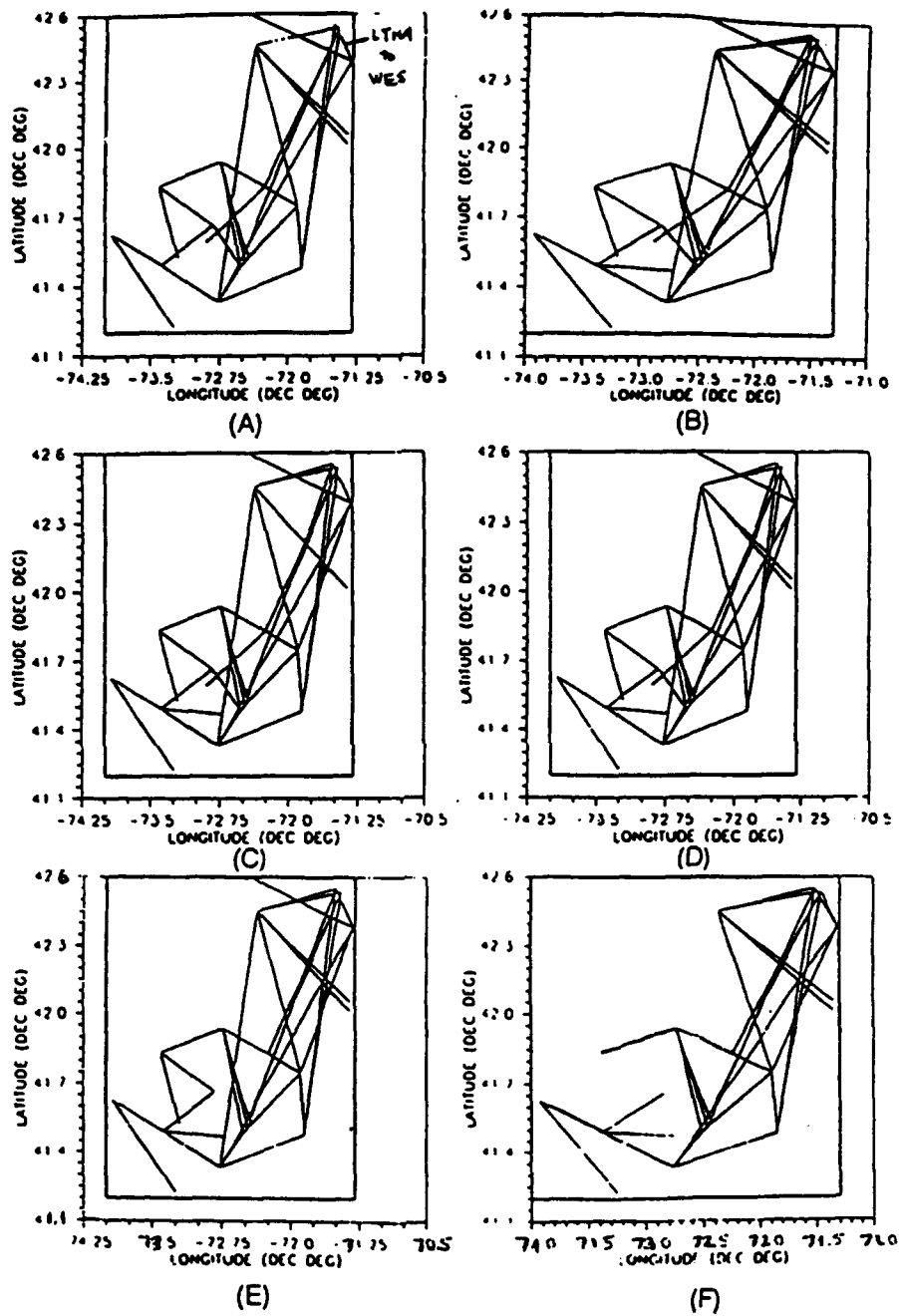


Figure 22 Paths in study area A represented by the Rg observed travel times at (A) $T=0.5$, (B) $T=0.7$, (C) $T=0.9$, (D) $T=1.1$, (E) $T=1.3$, and (F) $T=1.5$.

STATION NAME	* STATION LOCATION	LONGITUDE (DEC DEG)	LATITUDE (DEC DEG)
AZ1	TFS	71.5311	42.3864
AZ2	TFS	71.6467	42.3937
AZ3	TFS	71.8221	42.5156
AZ4	TFS	71.7821	42.6079
COD	CAPE COD, MA	70.1350	41.6858
DNH	DURHAM, MA	70.8948	43.1225
DUX	DUXBURY, MA	70.7678	42.0686
GLO	GLOUCESTER, MA	70.7272	42.6403
LC1	TFS	71.5571	42.5312
LC2	TFS	71.5910	42.5071
LC3	TFS	71.6267	42.4962
LC4	TFS	71.6935	42.4603
ONH	OAKHILL, NH	71.5056	43.2792
PNH	PITCHER MTN, NH	72.1358	43.0942
QUA	QUABBIN, MA	72.3738	42.4566
UXB	UXBRIDGE, MA	71.6773	42.0614
WES	WESTON, MA	71.3221	42.3847
WFM	WESTFORD, MA	71.4906	42.6106
WNH	WHITEFACE MTN, NH	71.3997	43.8683
NSA0	TFS	71.7270	42.4400
NSA1	TFS	71.7280	42.4390
NSA2	TFS	71.7240	42.4400

Table 7(A) Locations of stations used by D'Annolfo (1992).

STATION NAME	* STATION LOCATION	LONGITUDE (DEC DEG)	LATITUDE (DEC DEG)
NSA3	TFS	71.7280	42.4410
NSB1	TFS	71.7290	42.4400
NSB2	TFS	71.7260	42.4420
NSB3	TFS	71.7230	42.4390
NSB4	TFS	71.7260	42.4370
NSB5	TFS	71.7300	42.4390
NW01	TFS	71.5800	42.5790
NW02	TFS	71.5960	42.5940
NW03	TFS	71.6110	42.5950
NW04	TFS	71.6630	42.6155
NW05	TFS	71.6830	42.6240
NW06	TFS	71.7010	42.6360
NW07	TFS	71.7250	42.6520
NW08	TFS	71.7540	42.6610
NW10	TFS	71.8880	42.6880
NW11	TFS	71.8500	42.7550
P102	TFS	71.5660	42.5400
P103	TFS	71.5880	42.5360
P112	TFS	71.8396	42.5145
P113	TFS	71.8546	42.5121
P115	TFS	71.9054	42.5187

Table 7(A) Locations of stations used by D'Annolfo (1992).

STATION NAME	* STATION LOCATION	LONGITUDE (DEC DEG)	LATITUDE (DEC DEG)
P201	TFS	71.5390	42.5480
P202	TFS	71.5460	42.5450
P203	TFS	71.5550	42.5440
P206	TFS	71.5980	42.5310

* Temporary field stations (TFS) set up around the San-Vel Quarry

Table 7(A) Locations of stations used by D'Annolfo (1992).

EVENT	LOCATION	LOCATION CODE	DATE	ORIGIN TIME (DY:HR:MN:SEC)	* RMS (SEC)	LONGITUDE (DEC DEG)	LATITUDE (DEC DEG)
87202	SAN-VEL QUARRY LITTLETON, MA	LTMA	7/21/87	202:16:58:14.97	NA	71.5170	42.5540
87210	SAN-VEL QUARRY LITTLETON, MA	LTMA	7/29/87	210:18:13:56.17	NA	71.5170	42.5540
88089	SAN-VEL QUARRY LITTLETON, MA	LTMA	4/31/88	089:18:01:50.31	NA	71.5170	42.5540
89177	SAN-VEL QUARRY LITTLETON, MA	LTMA	6/26/89	177:18:28:55.31	0.240	71.5170	42.5540
89192	SAN-VEL QUARRY LITTLETON, MA	LTMA	7/11/89	192:19:33:54.80	0.150	71.5170	42.5540
89208	SAN-VEL QUARRY LITTLETON, MA	LTMA	7/27/89	208:17:29:48.18	0.200	71.5170	42.5540
89213	SAN-VEL QUARRY LITTLETON, MA	LTMA	8/1/89	213:19:29:25.89	0.300	71.5170	42.5540

- * Standard deviation of the origin times estimated by Equation 6.1.
NA indicates that origin times were known and not estimated.

Table 7(B) Event information recorded by D'Annolfo (1992).

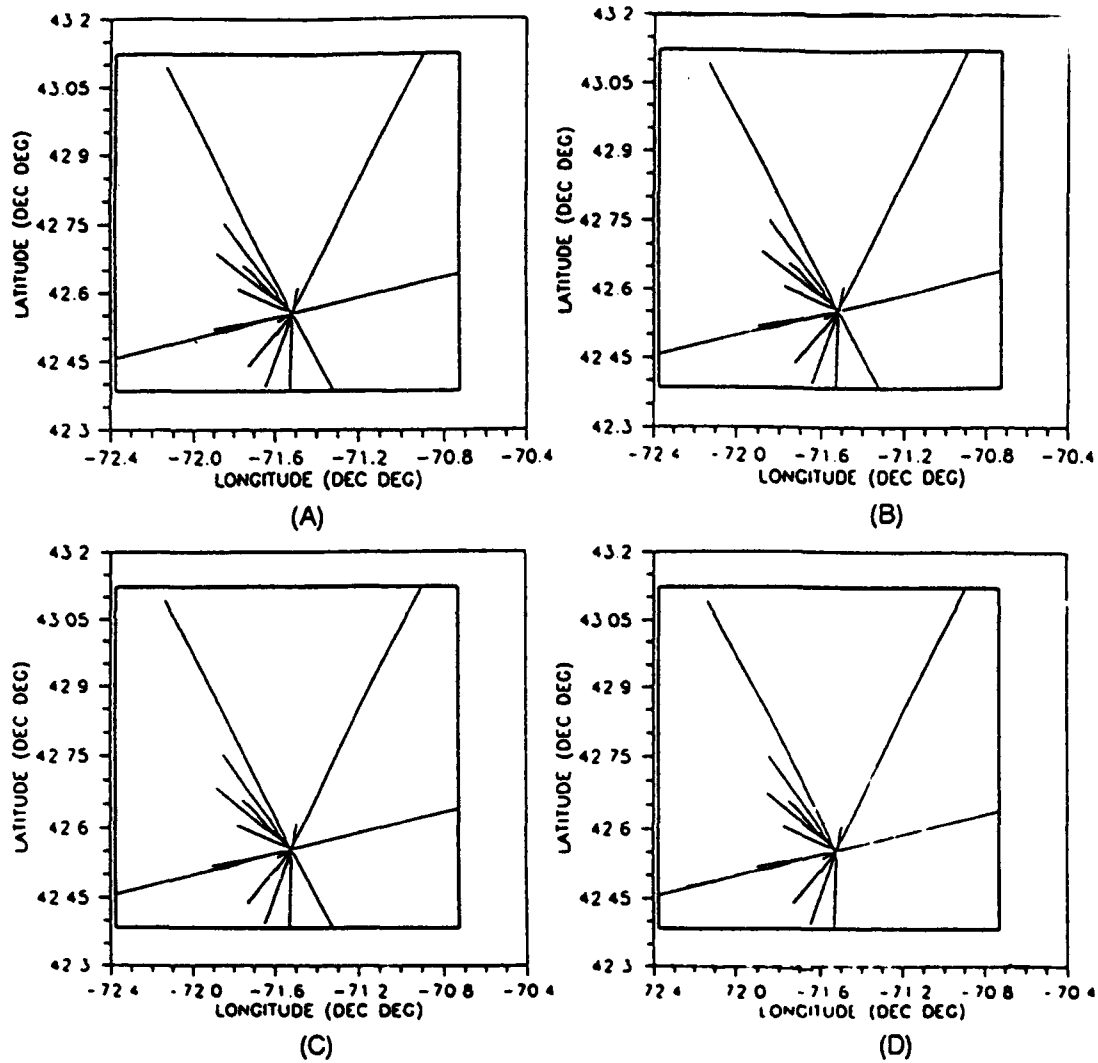


Figure 23 Paths in study area B represented by the Rg observed travel times at (A) $T=0.5$, (B) $T=0.7$, (C) $T=0.9$, and (D) $T=1.1$.

parameter before the first iteration of the analysis. The initial group velocity chosen for each period is that which has been published for the BADR because it is thought to represent a rough estimate of the average dispersion for most of SNE. Before the first inversion, SURFTOMO calculates the travel time residual for each data value (Δd_i) and the average travel time residual for all data values (σ_d^2). The resulting value of σ_d^2 is assumed to be a reasonable estimate of the variance for each data set.

The initial velocity model used for each data set from study area A is listed in Table 8(A) as well as the average travel time residual (σ_d^2) for all data values in each data set. Similarly, the initial velocity model used for each data set from study area B is listed in Table 8(B) as well as the average travel time residual (σ_d^2) for all data values in each data set.

7.1.2 The Analysis of Lateral Variation in Group Velocity

First, a block structure is chosen for the study area. The path information represented by the data values and the chosen block structure constitute a tomographic problem. An inversion technique that is most appropriate for this particular problem is chosen. Finally, an interpretation is made from the group velocities resulting from the tomographic inversion and the resolution and variance with which each group velocity was measured.

The Tomographic Problem

First, a tomographic problem is defined by selecting a block structure(s) for a data set represented by a specific density and distribution of paths. A block structure(s) is chosen based one or more of the following criteria: 1) the boundaries of the blocks

DATA SET	INITIAL GROUP VELOCITY OF MODEL (km/sec)	AVERAGE VARIANCE OF DATA (sec ²)
A1_05	2.45	1.358
A1_07	2.52	2.573
A1_09	2.59	1.902
A1_11	2.66	2.040
A1_13	2.71	2.196
A1_15	2.73	8.109

DATA SET	INITIAL GROUP VELOCITY OF MODEL (km/sec)	AVERAGE VARIANCE OF DATA (sec ²)
B1_05	2.45	1.333
B1_07	2.52	0.892
B1_09	2.59	0.745
B1_11	2.66	0.635

Table 8 (A) Study area A: Variance for each data set, and (B) Study area B: Variance for each data set.

coincided with the geologic boundaries of the lithotectonic terranes in the study area, 2) the block structure and path information presented a tomographic problem whose result was useful in the analysis of vertical variation of shear wave velocity, 3) the block structure allowed for the determination of as much group velocity information from the study area as was permitted by SURFTOMO and/or the path information, and 4) the preliminary results from a tomographic inversion were consistent with the R_g group velocities published in previous studies.

Inversion Techniques

Two inversion techniques, the SVD and weighted damped least squares methods, have been described above. Each method can be employed in two ways. The way in which each can be used is dictated by the kind of tomographic problem being solved, and by the desired resolution and variance with which the group velocities are to be estimated.

The SVD Method

The SVD method used to find the natural generalized inverse can be employed in two ways. In the first approach, all eigenvalues in the matrix Λ_p^{-1} are included in the analysis. In the second approach, each eigenvalue (starting with the lowest) is excluded from the analysis until most or all of the group velocities are within some predetermined range expected for SNE. An "eigenvalue ratio" is used to exclude each eigenvalue and those that are lower. An eigenvalue ratio is defined as slightly greater than the ratio of the eigenvalue that is being excluded to the maximum eigenvalue.

In the first approach, all eigenvalues in the matrix Λ_p^{-1} are included with the

exception of those that are considered to be the result of ill-defined variables in computer calculations. The eigenvalue ratio is set to 0.00001. In this case, any group velocity (model parameter) that is constrained by any observed R_g travel time is included in the vector space V_p . Also, any block that contains even the shortest path segment is included.

In the second approach, eigenvalues are excluded from the analysis by systematically increasing the cutoff for the eigenvalue ratio. The eigenvalue ratio is increased to the point where most or all of the group velocities are within the range expected for SNE. As the number of blocks for the same data set within a study area increases, the likelihood that a block has a low density and uneven distribution of path segments is high. A greater number of blocks are poorly constrained by the data values and the level of underdeterminacy increases. Consequently the cutoff for the eigenvalue ratios also increases.

The adjustment of the eigenvalue ratio profoundly affects the resolution and variance of the estimated group velocities. Since the variance of the model parameters is proportional to Λ_p^{-2} , the inclusion of very small eigenvalues generates large variances in the group velocities. However, in this case, the solution is very close to the natural solution and is well resolved. On the other hand, exclusion of small eigenvalues artificially lowers the dimensions of V_p and U_p . The solution is not the natural solution so the resolution is poor. However, the variance of each group velocity is smaller.

The Weighted Damped Least Squares Method

The weighted damped least squares method can be applied in many ways. Two

examples of how the weighted damped least squares method can be applied are considered in this study. In the first approach, the weighting model matrix, W_m , and the weighting data matrix, W_e , are equal to I and the damping constant, ϵ , is zero. In the second approach, W_m and W_e are equal to I , and the damping constant is nonzero.

To apply the first approach, the tomographic problem must be completely overdetermined. In the second approach, a damping constant that is nonzero damps the underdeterminacy of the problem. If the level of underdeterminacy in a mix-determined problem is relatively high, a larger damping constant is required by the analysis to yield group velocities within the range expected for SNE.

The value of the damping constant, ϵ , greatly affects the resolution and variance of the group velocities. Both solutions use a priori information to minimize the negative effects of the underdeterminacy of the problem. If ϵ^2 is large, the solution error, L , of the problem is minimized. However, the overdeterminacy of the problem is also minimized. The resolution of the solution is poor but the variances of the group velocities are small. Likewise, a very small value for ϵ^2 clearly minimizes the data prediction error, E , but not the underdeterminacy of the solution. The solution is well resolved but the variances of the group velocities are large. An appropriate value of ϵ^2 is one which approximately minimizes the data prediction error and the solution error of the problem. The value of ϵ^2 increases with the level of underdeterminacy of the problem.

Interpretation of Lateral Variation

Lateral variation in group velocity is interpreted from the results of the

tomographic inversion. A judgement of what constitutes lateral variation between adjacent blocks is based on the model variance and resolution with which each group velocity is estimated. If the difference between the group velocities of adjacent blocks is greater than the standard deviation with which each group velocity was estimated, and both group velocities are well resolved, lateral variation in group velocity exists (at least in the data, if not in the earth).

7.2 The Determination of Vertical Variation in Shear Wave Velocity

To estimate vertical variation in shear wave velocities beneath SNE, Rg dispersion data are inverted. First, sets of dispersion data from SNE are collected and prepared for an inversion program, RGINV, written by Edmund C. Reiter (Reiter et al., 1988). RGINV estimates a shear wave velocity structure for each set of dispersion data. As in the analysis of lateral variation in Rg group velocities, the errors mapped from the dispersion data to the shear wave velocity structure are given by the model covariance matrix. The resolution with which each shear wave velocity is estimated is given by the model resolution matrix. A three dimensional shear wave velocity structure for SNE is interpreted from the combination of the estimated shear wave velocity structures and their respective model covariance and resolution matrices.

7.2.1 Preparation of Dispersion Data for the Analysis of Vertical Variation

A typical dispersion curve from this and other published studies of Rg group velocity is comprised of estimated group velocities for a range of periods, often measured at equal intervals of period. For example, a typical dispersion curve for a path within the BADR is shown in Figure 24. It contains six group velocities measured at 0.5, 0.7,

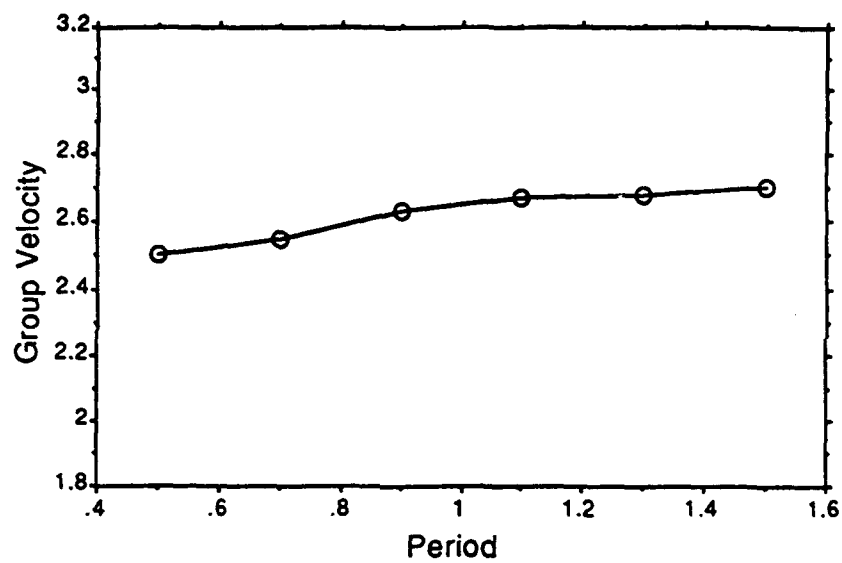


Figure 24 Typical dispersion curve for a path within the BADR.

0.9, 1.1, 1.3, and 1.5 sec respectively. The equal interval along the period axis is 0.2 sec. The computer program RGINV has been written for dispersion data estimated for some number, N , of group velocities measured at equal intervals of frequency. Thus, it is necessary to convert the dispersion data from this study (equal intervals of period) to data estimated at equal intervals of frequency. To prepare the dispersion data for RGINV, the original dispersion data are converted to a dispersion curve expected by RGINV in the following way. First a polynomial of degree 3 is fitted to the original dispersion data. The group velocities for the RGINV dispersion data are then interpolated from this polynomial at equal intervals of frequency.

Average Dispersion Data for the SNECB

The first set of dispersion data used for the analysis of vertical variation is prepared from the average dispersion curve from the study by D'Annolfo (1992). Her average dispersion curve is from numerous paths covering a large portion of the SNECB, and is assumed here to represent a good estimate of the average shallow crustal structure beneath the SNECB. The average dispersion curve published by D'Annolfo (1992), and that published by Kafka (1988) are shown in Figure 25. A second set of dispersion data is from this study. Specifically, I have analyzed dispersion data from over 50 seismograms recorded over a path from the San-Vel/Lonestar Quarry (LTMA) to the NESN station WES (A2_*.DAT) contained within the SNECB [Figure 25]. A third set of dispersion data used for this analysis of vertical variation is the dispersion curve for seven observations of the dispersion for the path from the San-Vel/Lonestar Quarry to a seismic array temporarily installed at Sterling, MA (STMA, see D'Annolfo, 1992). The

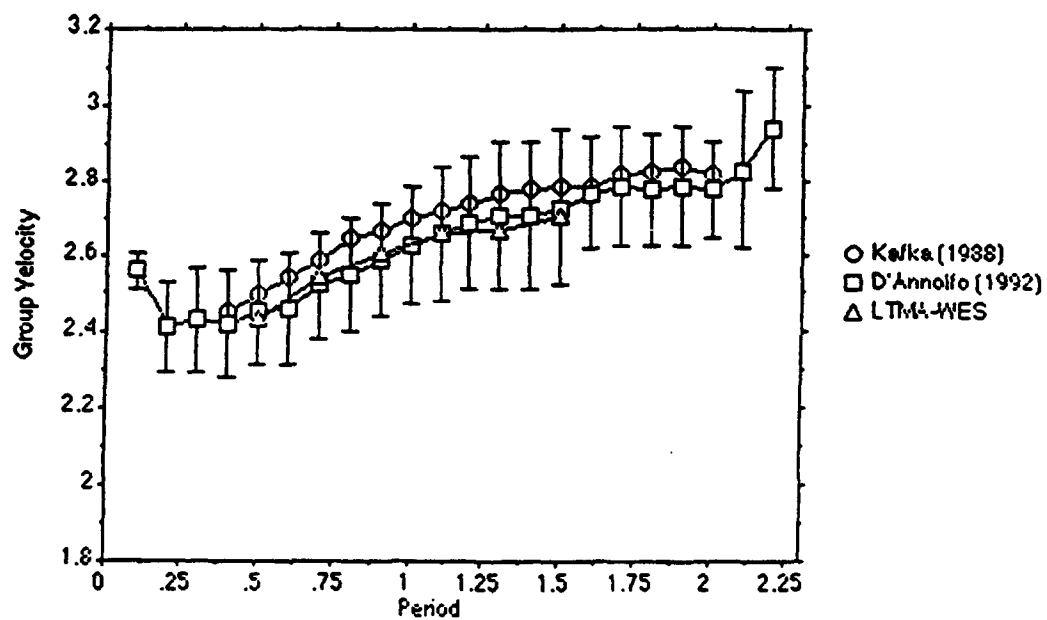


Figure 25 Dispersion data for the SNECB (Kafka, 1988; D'Annolfo, 1992), and along the path from the San-Vel/Lonestar Quarry (LTMA) to the NESN station WES.

STMA data are shown in Figure 26 along with those from D'Annolfo (1992) and Kafka (1988). All of these curves are quite similar, suggesting that the curve published by D'Annolfo (1992) is indeed generally representative of the average dispersion in the SNECB.

Dispersion Data from the Tomographic Inversion of Observed Rg Travel Times

The final set of dispersion data used for the analysis of vertical variation is prepared from the results of the tomographic inversion of observed Rg travel times. For the same block structure and study area, the tomographic inversion of observed Rg travel times at a series of discrete periods yields a series of solutions, each being a set of group velocities for a specific period [Figure 27(A)]. One can envision each set as corresponding to a "layer" [Figure 27(B)]. Each block can then be represented by a dispersion curve as illustrated in Figure 27(C).

Ideally, the dispersion curve estimated for every block in the block structure is a "high quality" estimate of the actual dispersion. In other words, the Rg group velocities are well resolved and have a low variance, the dispersion curve is estimated over a wide range of periods, and the curve is smooth enough that it can be interpolated to yield a curve acceptable to RGINV without introducing significant errors. Furthermore, since all of the average curves discussed above exhibit normal dispersion in the period range of 0.5 to 2.0 sec (the period range over which the Rg waves are strongest), blocks that produced results with suspiciously low values of group velocity at longer periods should probably not be considered as "high quality" in terms of dispersion results.

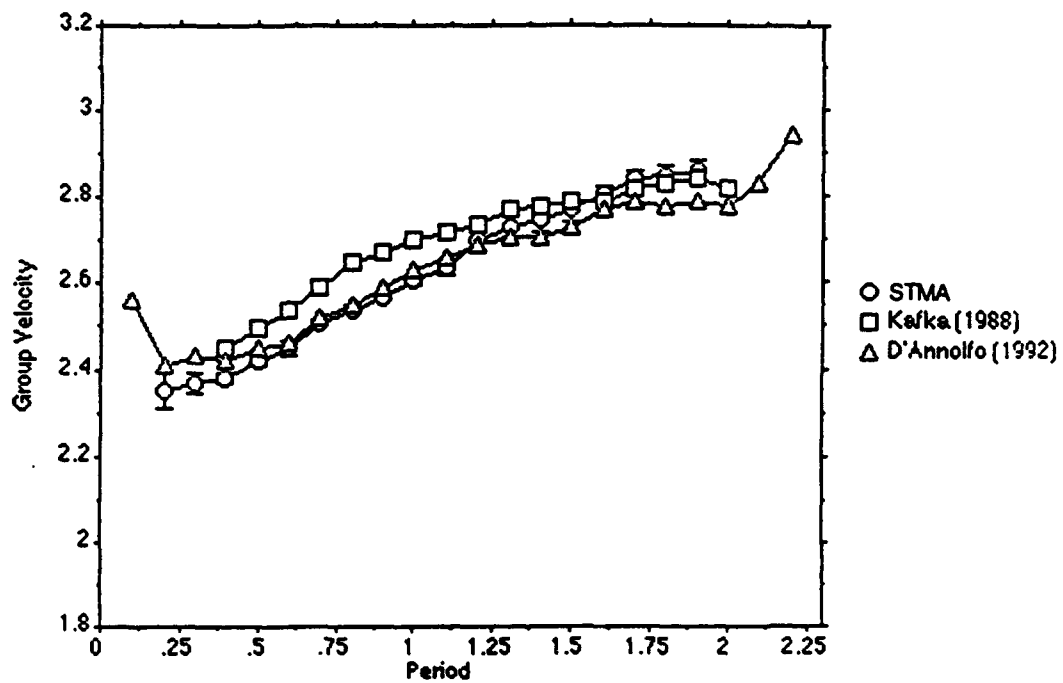
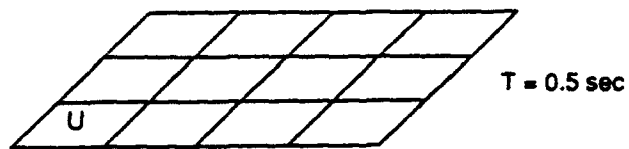
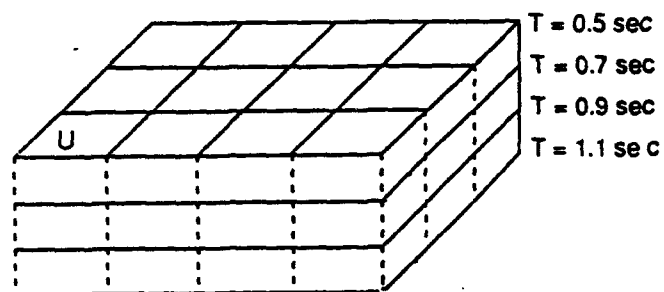


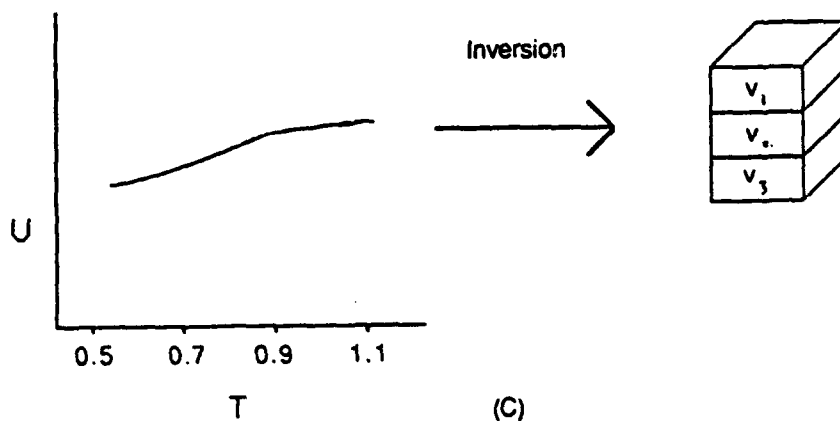
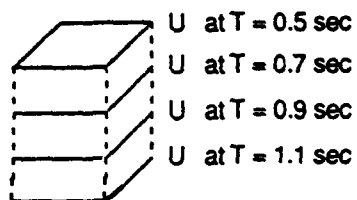
Figure 26 Dispersion data for the SNECB (Kafka, 1988; D'Annolfo, 1992), and dispersion data recorded at the Sterling, MA (STMA) array (D'Annolfo, 1992).



(A)



(B)



(C)

Figure 27 (A) Group velocity results from a tomographic inversion, (B) "stacking" group velocity results for several periods, and (C) a dispersion curve for each block. An inversion of each curve yields a shear wave velocity structure for each block.

More often than not, the dispersion curves of only some of the blocks in a block structure exhibit these characteristics, and can be considered "high quality" dispersion results. Therefore, only some of the blocks in a block structure are chosen to be inverted.

7.2.2 The Analysis of Vertical Variation in Shear Wave Velocity

Dispersion data for the average dispersion curves representing the SNECB (discussed in the previous section), as well as for blocks from the tomographic inversion which exhibit "high quality" normal dispersion are inverted to obtain estimates of the variation of shear-wave velocity as a function of depth in various parts of SNE. The inversion method used for this part of the study is the maximum likelihood inverse (Reiter et al., 1988; see chapter 6). Inversion procedures for determining the depth dependence of seismic velocities from surface wave dispersion data are based on the relationship between the frequency dependence of surface wave velocity and the depth dependence of seismic velocities. Thus, these procedures are only effective if the observed dispersion curves are defined over a wide frequency band.

The average dispersion curve for the SNECB (taken from D'Annolfo, 1992) is defined over an acceptable period range [Figure 25]. However, the dispersion data from the tomographic inversion of observed R_g travel times are defined over a narrower (and therefore unacceptable) period range (0.5 - 1.5 sec). To invert this dispersion data, the following approach was taken. First the average curve for the SNECB was inverted to obtain a shear wave velocity model. This model was then systematically perturbed and forward modelled to obtain shear wave velocity models that match the dispersion data for

individual blocks (i.e. defined over the narrower frequency range). The validity of this approach is (to some extent) supported by the observation that for all of the "high quality" dispersion data obtained from the tomographic inversion, the shape of the dispersion curves are quite similar. I do, of course, recognize that there is some circular reasoning here because several of the dispersion curves were eliminated because they did not exhibit normal dispersion.

The approach described above was considered to be acceptable for all "high quality" dispersion curves corresponding to blocks within the SNECB. Another approach is taken in the case of blocks associated with the HRB because the shapes of the dispersion curves for those blocks are not expected to be similar to that of the SNECB. Based on a third degree polynomial fit, the dispersion curve for one of the blocks covering the HRB was interpolated to obtain estimates of dispersion data at equal intervals of frequency. This curve was inverted to obtain a shear wave velocity model for that block.

8. Results

In this section, the results of the tomographic inversion of observed R_g travel times are discussed for study areas A and B. For study area A, 3x2 and 5x6 block structures are chosen. The SVD method is employed to yield a set of group velocities at periods of 0.5, 0.7, 0.9, 1.1, 1.3, and 1.5 sec. For study area B, a 9x9 block structure is chosen. The SVD method is employed to yield a set of group velocities at 0.5, 0.7, 0.9, and 1.1 sec. Only those blocks that exhibit "high quality" normal

dispersion (see Section 7.2) have been selected for the discussion of lateral variation in group velocity across SNE.

The dispersion data for the blocks that exhibit "high quality" normal dispersion are compared with dispersion results from previous studies of SNE. The average dispersion curve for SNECB, the dispersion curve for the HRB, and the "high quality" dispersion curves obtained from the tomographic inversion are analyzed to obtain shear wave velocity models for SNE. The methods used for this part of the study involve a combination of inversion and forward modelling approaches (see Section 7.2).

8.1 Study Area A

Two block structures are chosen for the tomographic analyses of study area A. The first, a 3x2 block structure, is chosen because it, along with the path information represented by the A1 data sets (A1_*.DAT), describes a tomographic problem whose results were appropriate for the analysis of vertical variation. Furthermore, the boundaries of the blocks coincided (approximately) with the geologic boundaries of the lithotectonic terranes of study area A. The second structure, a 5x6 block structure, is chosen because the block boundaries coincide more closely with the boundaries of lithotectonic terranes than in the case of the 3x2 block structure. Furthermore, preliminary results of the tomographic analyses for the 5x6 structure yield results similar to Rg group velocity results published in previous studies (e.g. Kafka and Skehan, 1990).

8.1.1 Dispersion Across Study Area A

A 3x2 Block Structure

The 3x2 block structure divides study area A into six blocks as shown in Figure

28(A). The paths represented by the data values (data set A1_07.DAT) at a period of 0.7 sec are shown in Figure 28(B). Block 4 does not contain any path segments at any period. Therefore, the group velocity of block 4 is set equal to the that of the initial model assigned to every block for each period, and it remains constant throughout the tomographic inversion.

The SVD method was used to obtain an R_g group velocity for each block at periods 0.5, 0.7, 0.9, 1.1, 1.3, and 1.5 sec. The density and distribution of path segments in every block, with the exception of block 4, is relatively high. Therefore, all eigenvalues are included in the analyses.

The group velocities at each period are shown in Figure 29. The group velocities at a period of 0.7 sec for all blocks except block 4 are shaded in Figure 30(A). Each group velocity, with the exception of that for block 4, is perfectly resolved to 8 decimal places for every period. Each row of the model covariance matrix is plotted in Figure 31. The assumptions made regarding the data covariance matrix appear to be valid since the diagonal element of every row is larger than all other elements in the row.

The dispersion data for blocks 1, 2, 3, and 6 exhibit "high quality" normal dispersion. Block 4 contains no path segments. The density and distribution of path segments in block 5 are poor. Furthermore it does not exhibit normal dispersion. Eliminating blocks 4 and 5, Figure 30 is redrawn in Figure 32. The dispersion curve associated with each of these blocks, and the average dispersion data for the SNECB are shown in Figure 33(A).

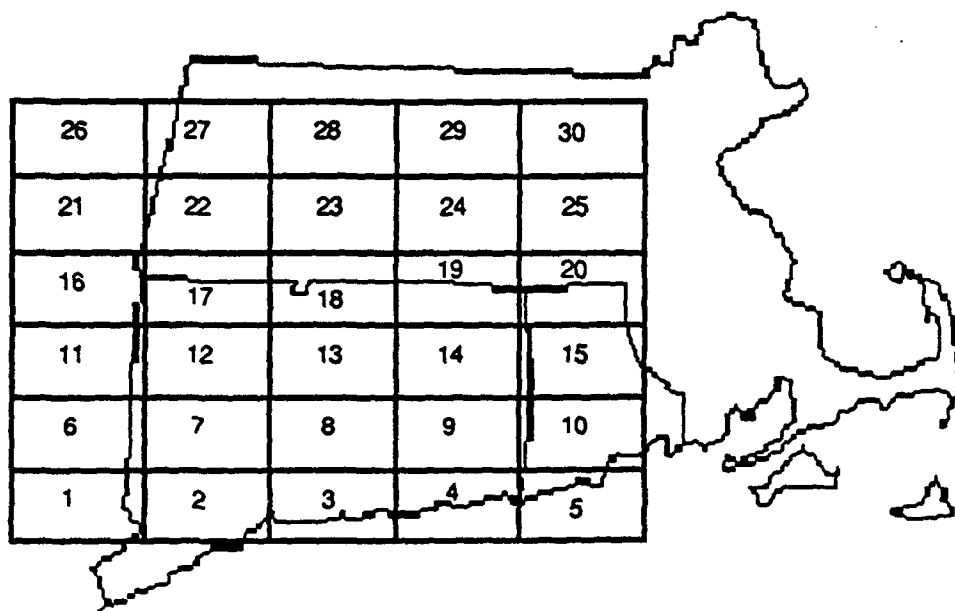
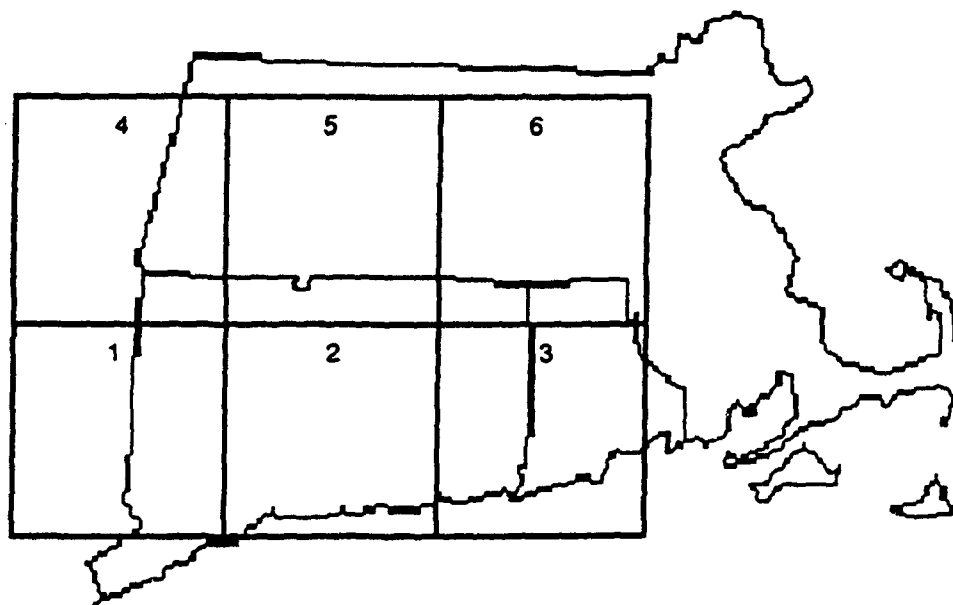


Figure 28(A) (Top) A 3x2 block structure divides study area A into six blocks. (Bottom) A 5x6 block structure divides study area A into thirty blocks.

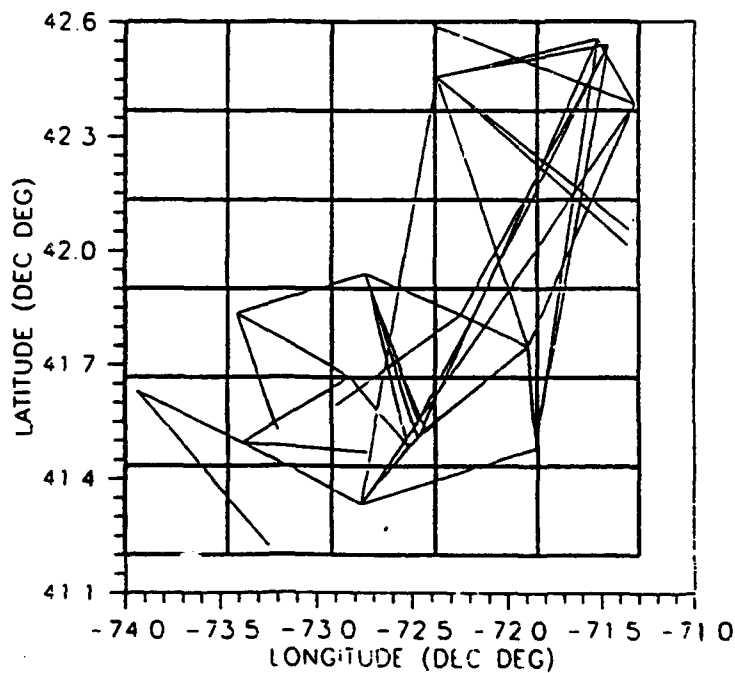
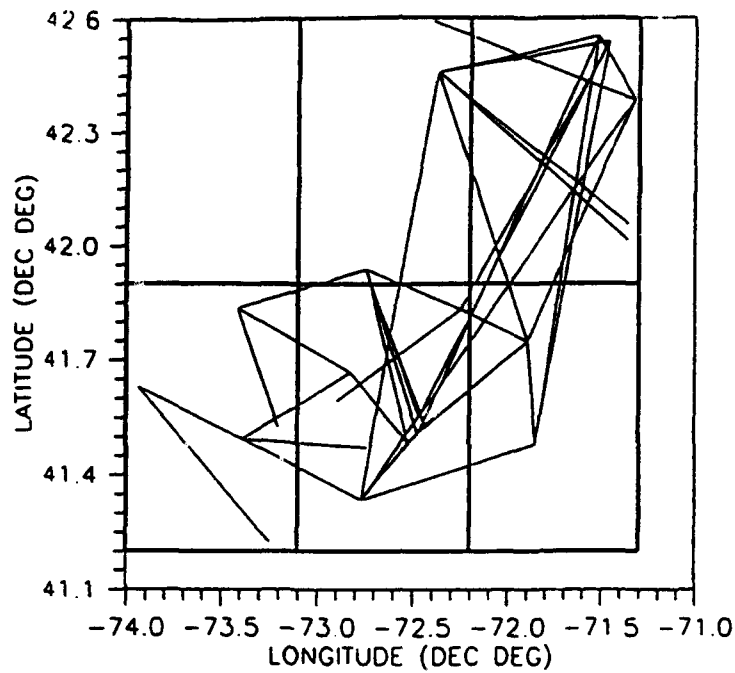


Figure 28(B) Paths represented by R_g observed travel times at $T=0.7$ are superimposed over the 3x2 block structure (top) and the 5x6 block structure (bottom). Curvature of the earth is not taken into account.

T=0.5 sec			T=0.7 sec			T=0.9 sec		
2.45			2.52			2.59		
.	2.67	2.46	.	2.69	2.58	.	2.80	2.67
2.52	2.33	2.62	2.63	2.30	2.81	2.67	2.49	2.78
T=1.1 sec			T=1.3 sec			T=1.5 sec		
2.66			2.71			2.73		
.	2.64	2.74	.	2.69	2.75	.	2.50	2.72
2.75	2.54	2.85	2.84	2.52	2.97	2.94	2.51	3.09

T=0.5 sec, Ratio = 0.0371					T=0.7 sec, Ratio = 0.0633				
2.45*	2.45*	2.79	2.56	2.42	2.52*	2.52*	2.71	2.57	2.54
2.45*	2.45*	3.75	2.35	2.49	2.52*	2.52*	3.34	2.46	2.65
2.45*	2.42	2.62	2.70	2.48	2.52*	2.52	3.12	2.91	2.42
2.45*	2.31	2.03	2.43	2.72	2.52*	2.49	1.99	2.47	2.80
2.59	2.40	2.62	2.42	2.64	2.90	2.27	2.39	2.73	2.73
3.10	2.32	2.28	3.66	2.45*	2.27	2.67	2.69	2.19	2.52*
T=0.9 sec, Ratio = 0.0633					T=1.1 sec, Ratio = 0.0234				
2.59*	2.59*	2.74	2.67	2.60	2.66*	2.66*	2.95	2.73	2.66
2.59*	2.59*	3.47	2.64	2.88	2.66*	2.66*	4.89	2.34	2.66
2.59*	2.52	3.39	2.95	2.60	2.66*	2.29	2.36	3.54	2.94
2.59*	2.25	2.13	2.50	2.70	2.66*	2.30	2.26	2.69	2.93
2.93	2.54	2.59	2.73	2.63	3.03	2.65	2.59	2.72	2.44
2.61	2.54	2.69	2.53	2.59*	2.84	2.56	2.68	2.61	2.66*
T=1.3 sec, Ratio = 0.0617					T=1.5 sec, Ratio = 0.1553				
2.71*	2.71*	2.70	2.88	2.67	2.73*	2.73*	2.73*	2.87	2.57
2.71*	2.71*	3.26	2.43	3.03	2.73*	2.73*	2.73*	2.39	3.05
2.71*	2.51	3.01	3.23	2.46	2.73*	2.74	2.61	3.31	2.46
2.71*	2.30	2.23	2.58	2.94	2.73*	2.82	2.35	2.65	3.00
3.14	2.65	2.48	3.09	2.84	3.22	2.64	2.43	3.16	2.99
2.35	2.96	2.79	2.31	2.71*	2.35	3.01	2.97	2.48	2.73*

Figure 29 Study area A: Group velocity results at periods 0.5, 0.7, 0.9, 1.1, 1.3, and 1.5 sec using (top) a 3x2 block structure and (bottom) a 5x6 block structure (a * indicates the absence of path segments in a block).

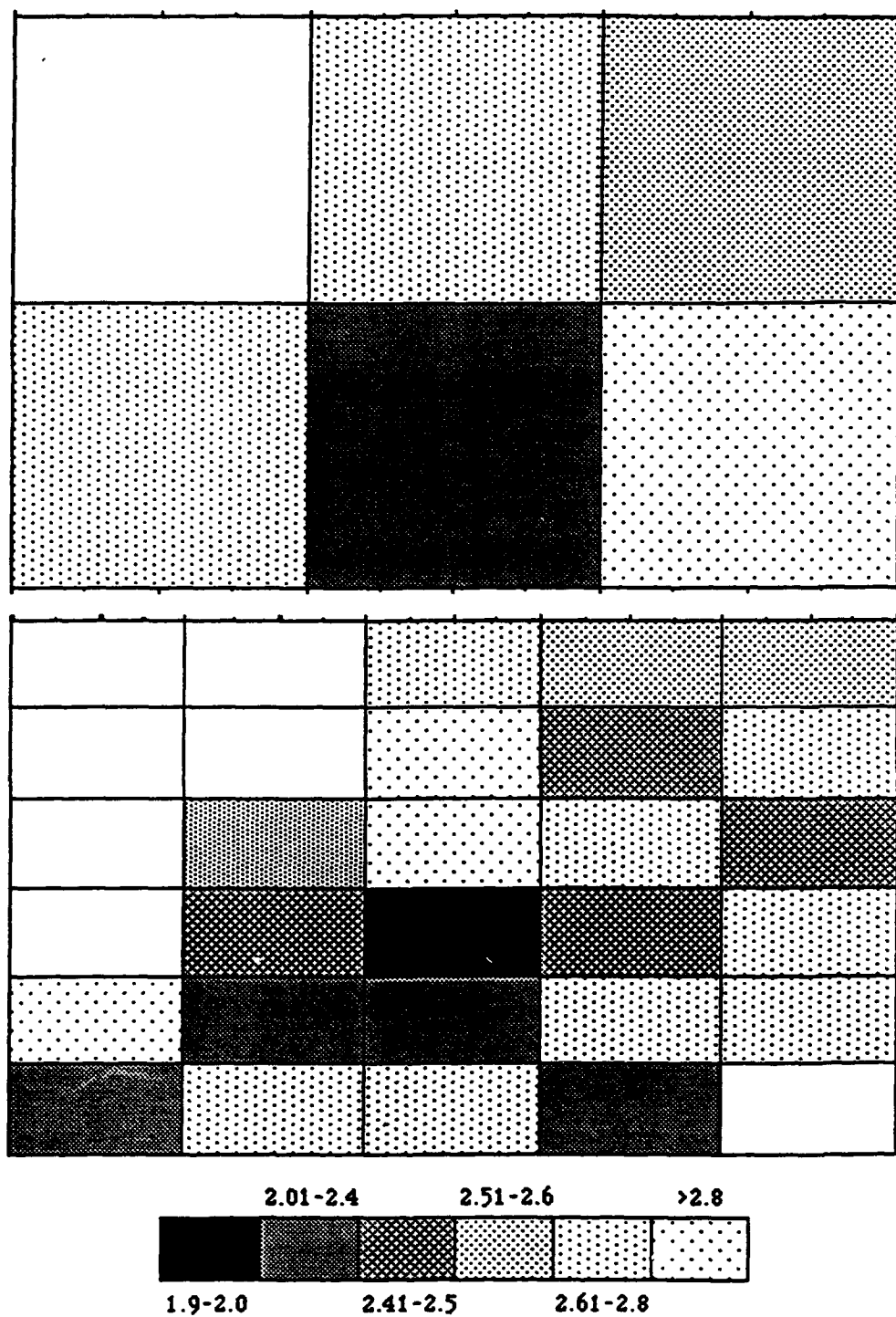


Figure 30 Study area A: Dispersion results using (top) a 3x2 block structure and (bottom) a 5x6 block structure (only blocks containing path segments are shaded).

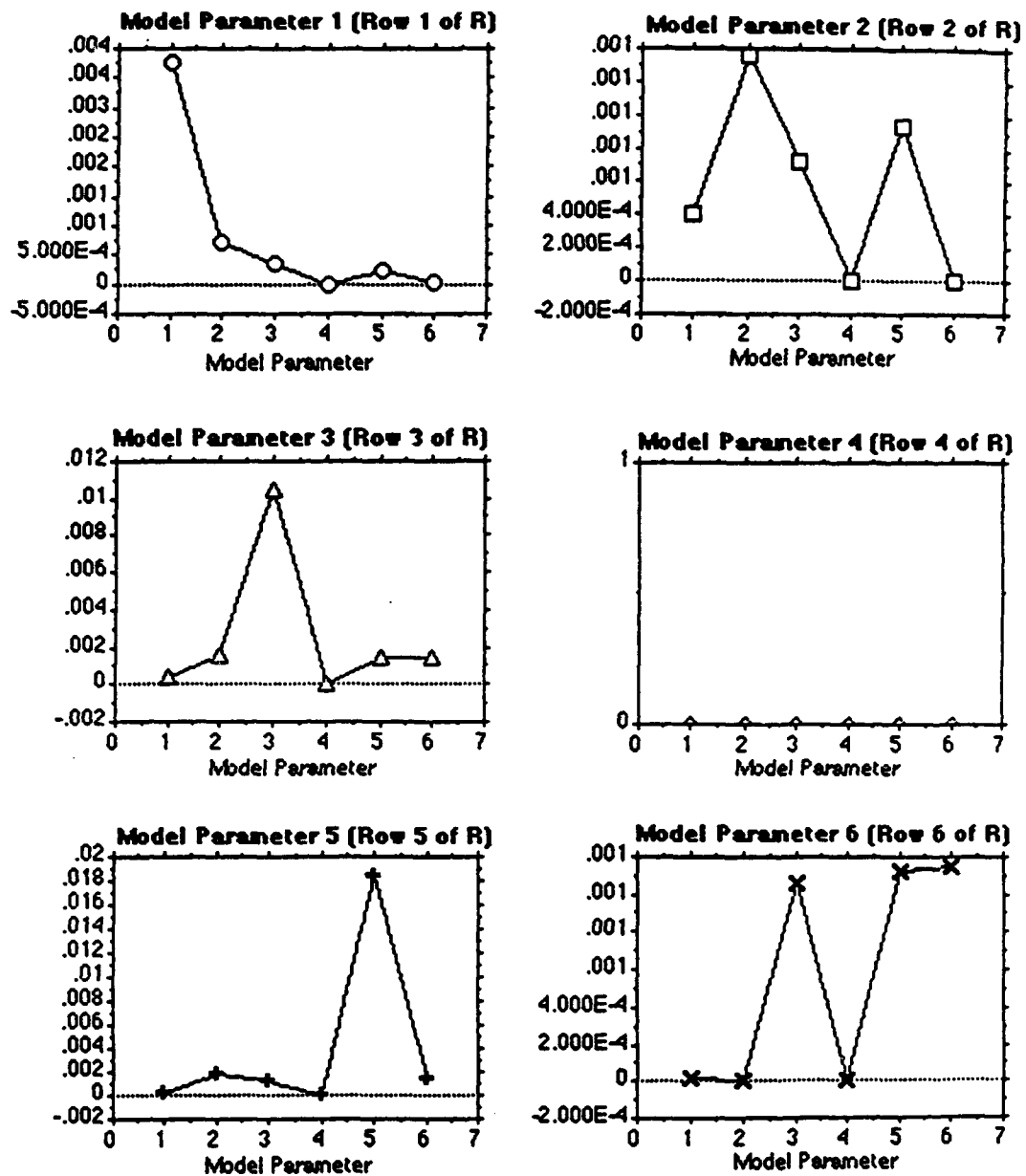


Figure 31 Study area A: Variance of each group velocity at $T=0.7$ sec.

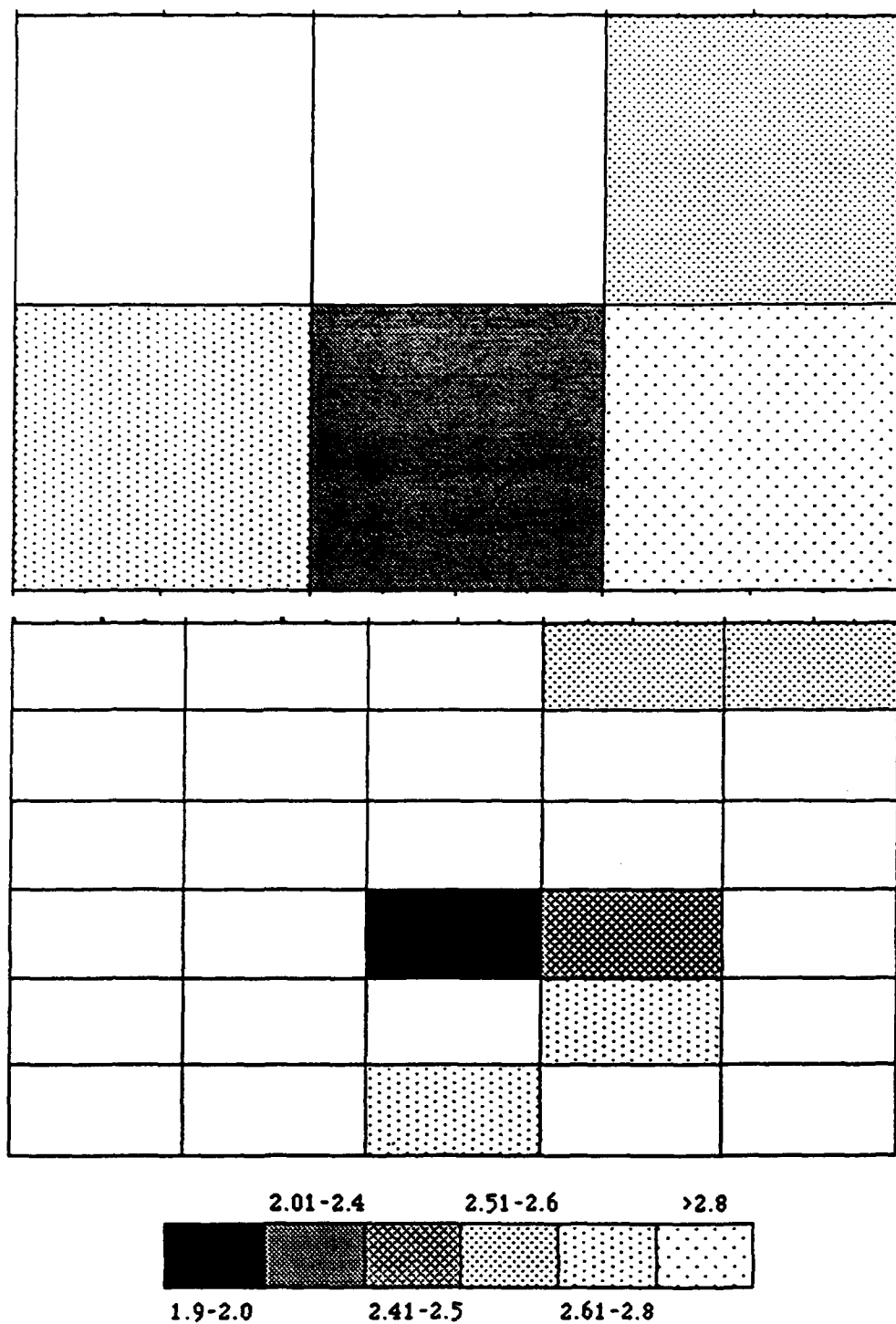


Figure 32 Study area A: Dispersion results using (top) a 3x2 block structure and (bottom) a 5x6 block structure (shaded blocks exhibit "high quality" dispersion).

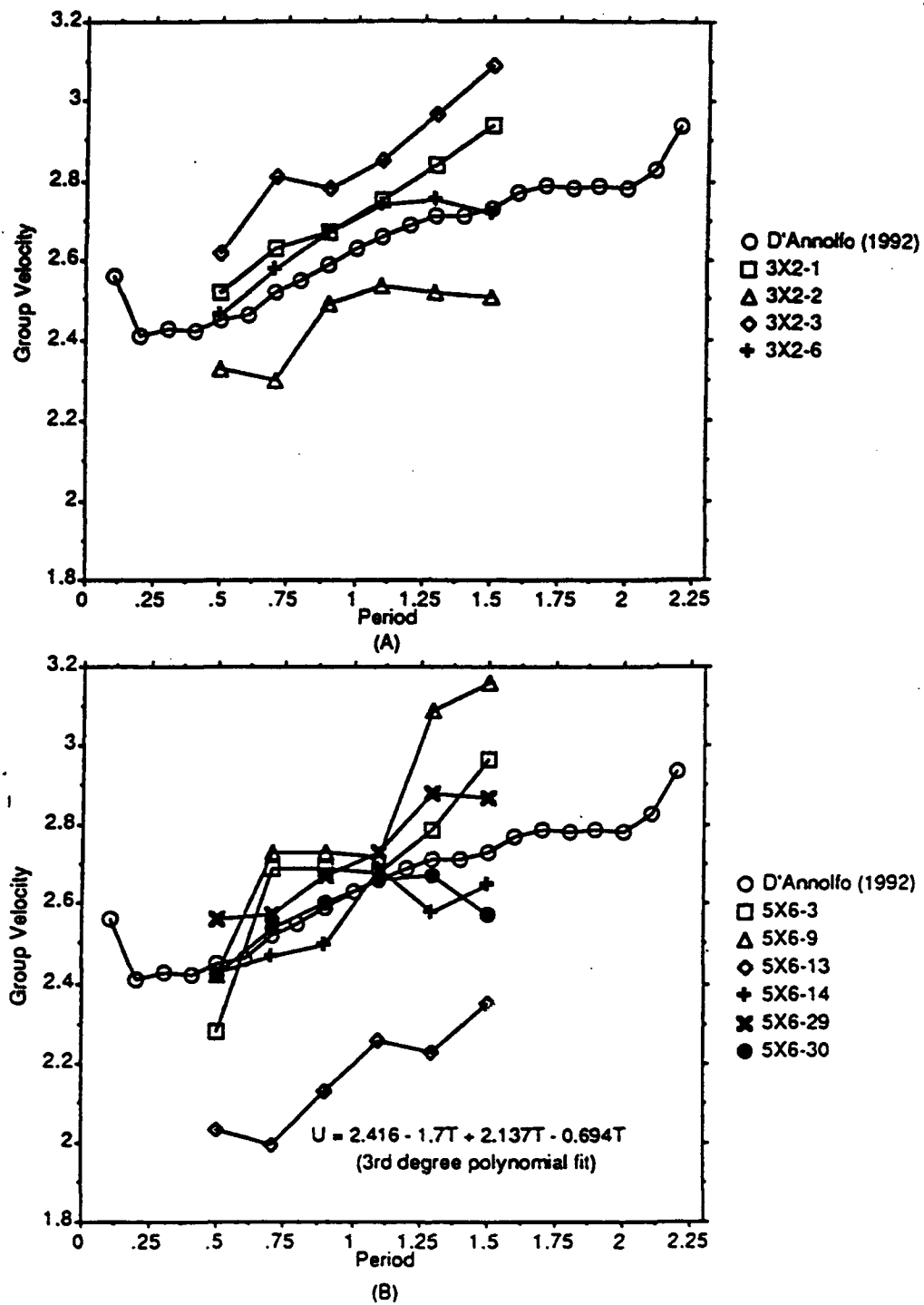


Figure 33 Study area A: Dispersion curves for the SNECB and for blocks exhibiting "high quality" dispersion of (A) the 3x2 block structure and (B) the 5x6 block structure.

A 5x6 Block Structure

The 5x6 block structure divides study area A into thirty blocks as shown in Figure 28(A). The paths represented by the data values (data set A1_07.DAT) at a period of 0.7 sec are shown in Figure 28(B). Blocks 5, 11, 16, 21, 22, 26, and 27 do not contain any path segments at any period. Blocks 23 and 27 do not contain any path segments at a period of 1.5 sec. The group velocity for each of these blocks with no data is assigned the velocity of the initial model and remains constant throughout the tomographic analysis.

The SVD method was also used to obtain Rg group velocities at periods of 0.5, 0.7, 0.9, 1.1, 1.3, and 1.5 sec. Since the 5x6 block structure divides the study area into a larger number of blocks than in the previous case, the density and distribution of path segments were quite high for some blocks, but quite low for others. Therefore low eigenvalues were systematically excluded from the tomographic analysis. First all eigenvalues were used in the tomographic analysis for each period. The smallest eigenvalue was then removed from the analysis of each period by increasing the eigenvalue ratio. The procedure was repeated until most or all of the group velocities were within a reasonable range of group velocities expected for SNE.

The group velocities and eigenvalue ratio used for each period are shown in Figure 29. The group velocity at a period of 0.7 sec is shaded for each block that contained path segments in Figure 30. Some of the group velocities, with the exception of those blocks with no path segments, are perfectly resolved to within two decimal places. The resolution of each group velocity (model parameter j) was classified as

quality A, B, C, or D, based on the value of the diagonal element of row j. The classification of resolution is as follows:

A	diagonal element	> 0.80
B	diagonal element	0.5-0.79
C	diagonal element	0.3-0.49
D	diagonal element	< 0.30

Table 9 indicates how the resolution of each group velocity in Figure 29 was classified for periods from 0.5 to 1.5 sec.

The group velocities that are not perfectly resolved are weighted averages of the group velocities of adjacent blocks. For example, the resolution of model parameters 10, 15, and 20 (which represent velocities of adjacent blocks in the eastern section of the study area) are given by rows 10, 15, and 20 of the model resolution matrix respectively. The elements of each row are plotted in Figure 34 for the period of 0.7 sec. The group velocities for blocks 10, 15, and 20 are weighted averages of the group velocities for blocks 10, 15, and 20 as illustrated by the first, second, and third plots respectively in Figure 34.

The model covariance matrix suggests that the assumptions for the data covariance matrix [cov d] appear to be invalid for some of the group velocities in this tomographic analysis. In some cases, the diagonal element of each row in the model covariance matrix for all periods is not larger than the other elements of that row. Nevertheless, the diagonal elements for each group velocity, along with information on whether the diagonal element was larger relative to the other elements in the row, are given in Table 10.

The dispersion data for blocks 3, 9, 13, 14, 29, and 30 exhibit "high quality"

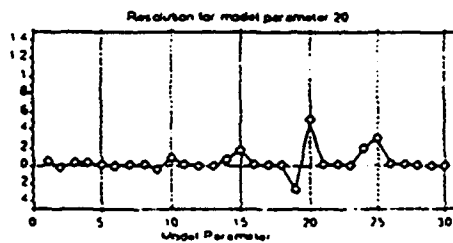
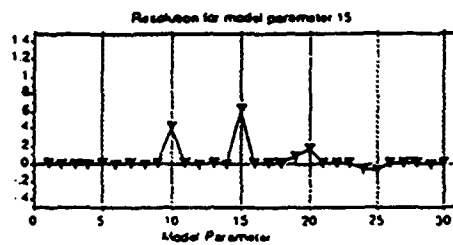
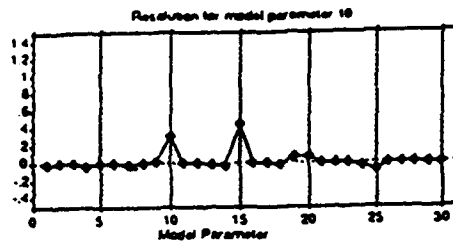


Figure 34 Study area A: The resolution of the group velocity at $T=0.7$ sec for blocks 10, 15, and 20 respectively, where each plot is representative of rows 10, 15, and 20 respectively of the model resolution matrix R .

BLOCK #	PERIOD					
	0.5 SEC	0.7 SEC	0.9 SEC	1.1 SEC	1.3 SEC	1.5 SEC
1	A	B	B	A	B	D
2	A	A	A	A	A	A
3	A	A	A	A	A	A
4	A	B	B	A	B	D
5	NA	NA	NA	NA	NA	NA
6	A	A	A	A	A	A
7	A	A	A	A	A	A
8	A	A	A	A	A	B
9	A	A	A	A	A	A
10	D	C	C	B	C	D
11	NA	NA	NA	NA	NA	NA
12	A	A	A	A	A	B
13	A	A	A	A	A	B
14	A	A	A	A	A	B
15	B	B	B	B	B	D
16	NA	NA	NA	NA	NA	NA
17	D	D	D	D	D	D
18	A	B	B	A	B	D
19	A	A	B	A	A	B
20	C	B	B	A	B	C
21	NA	NA	NA	NA	NA	NA
22	NA	NA	NA	NA	NA	NA
23	A	C	C	A	C	NA
24	A	A	A	A	A	A
25	A	B	B	A	B	B
26	NA	NA	NA	NA	NA	NA
27	NA	NA	NA	NA	NA	NA
28	D	D	D	D	D	D
29	A	A	A	A	A	A
30	A	A	A	A	A	A

NA indicates that the block did not contain any path segments

Table 9 Resolution of group velocities for study area A for a 5x6 block structure.

BLOCK #	T = 0.5 SEC		T = 0.7 SEC		PERIOD T = 0.9 SEC		T = 1.1 SEC		T = 1.3 SEC		T = 1.5 SEC	
	(")		(")		(")		(")		(")		(")	
1	0.87	*	0.14	*	0.18	*	0.89	*	0.14	*	0.01	
2	0.05		0.06	*	0.03	*	0.11		0.07	*	0.16	*
3	0.04		0.04	*	0.03	*	0.10		0.04	*	0.15	*
4	2.07	*	0.10		0.13		0.73	*	0.11	*	0.02	
5	NA		NA		NA		NA		NA		NA	
6	0.01	*	0.03	*	0.03	*	0.03	*	0.04	*	0.11	*
7	0.01		0.01	*	0.01	*	0.01		0.01		0.03	*
8	0.04		0.03	*	0.03	*	0.05		0.04	*	0.03	*
9	0.02	*	0.05	*	0.04	*	0.05	*	0.07	*	0.09	*
10	0.01		0.03		0.03		0.15	*	0.04	*	0.08	
11	NA		NA		NA		NA		NA		NA	
12	0.01	*	0.03	*	0.01	*	0.02	*	0.02	*	0.25	*
13	0.01	*	0.01	*	0.01	*	0.02		0.02	*	0.03	*
14	0.03	*	0.05	*	0.04	*	0.07	*	0.05	*	0.06	*
15	0.04	*	0.07	*	0.05	*	0.07	*	0.06	*	0.17	*
16	NA		NA		NA		NA		NA		NA	
17	0.02		0.00		0.00		0.02		0.00		0.01	
18	0.18	*	0.11	*	0.10	*	0.16	*	0.07	*	0.05	
19	0.03	*	0.06	*	0.05	*	0.48	*	0.08	*	0.23	*
20	0.01		0.01		0.02	*	0.39	*	0.01		0.03	*
21	NA		NA		NA		NA		NA		NA	
22	NA		NA		NA		NA		NA		NA	
23	0.86	*	0.12	*	0.10	*	4.26	*	0.11	*	NA	
24	0.02	*	0.04	*	0.04	*	0.04		0.03	*	0.09	*
25	0.03	*	0.05	*	0.04	*	0.16	*	0.08	*	0.02	*
26	NA		NA		NA		NA		NA		NA	
27	NA		NA		NA		NA		NA		NA	
28	0.02		0.00		0.00		0.05		0.01		NA	
29	0.02	*	0.01	*	0.01	*	0.01	*	0.02	*	0.08	*
30	0.00	*	0.00	*	0.00	*	0.00	*	0.00	*	0.01	*

Table 10 Variance of group velocities for study area A using a 5x6 block structure.

normal dispersion. The remaining blocks contain either no path segments or exhibit dispersion not considered to be high enough quality for the study of vertical variation in shear wave velocity. Considering only the blocks listed above, Figure 30 is redrawn in Figure 32. The dispersion curve associated with each of these blocks, and the average dispersion data for the SNECB are shown in Figure 33(B).

8.1.2 Shear-Wave Velocity Models for Study Area A

Two dispersion curves are inverted to obtain two shear wave velocity models. The first is the average dispersion curve for the SNECB [Figure 35], taken from D'Annolfo (1992). The resulting shear wave velocity model is shown in Figure 36. The resolution and variance with which each shear wave velocity was measured is given in Table 11. The second dispersion curve that was inverted is that of block 13 of the 5x6 block structure. The dispersion curve that is inverted for block 13 is shown in Figure 35. The resulting shear wave velocity model is shown in Figure 36. The resolution and variance with which each shear wave velocity was measured is given in Table 11.

8.2 Study Area B

The 9x9 block structure was chosen for study area B. This structure was chosen based on the analysis of the results of the previous study of this area by D'Annolfo (1992). Furthermore, this block structure represents an attempt to obtain as much group velocity information as possible from the path information.

8.2.1 Dispersion Across Study Area B

The 9x9 Block Structure

This block structure divides study area B into 81 blocks as shown in Figure 37.

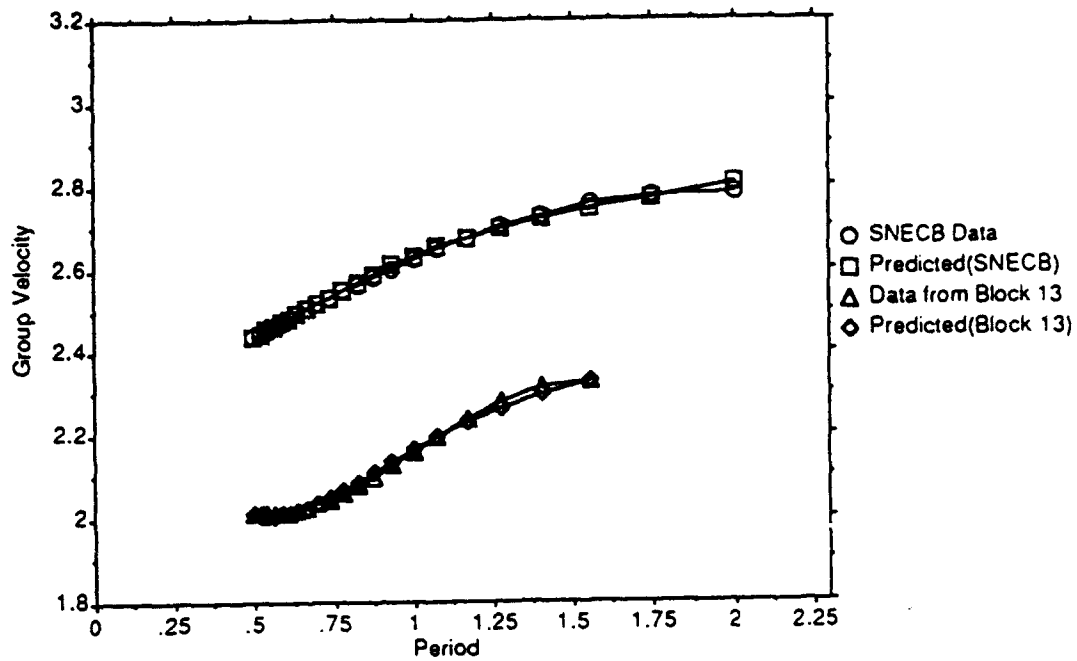


Figure 35 Study area A: Dispersion curves for block 13 and the SNECB (D'Annolfo, 1992) inverted by RGINV, and for block 13 and the SNECB as predicted by the shear wave velocity models in Figure 36.

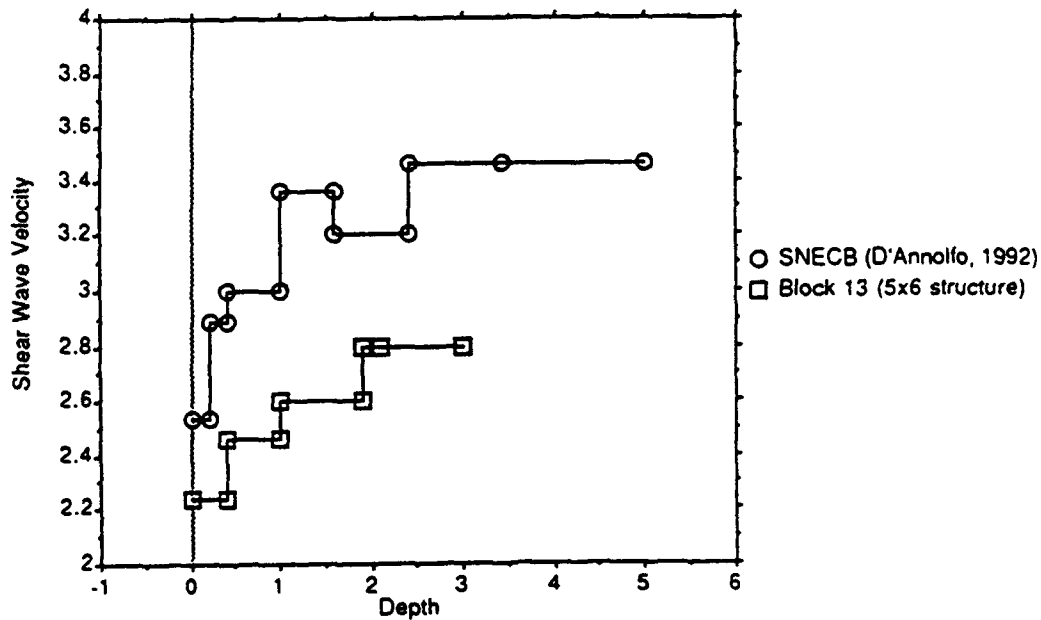


Figure 36 Study area A: Shear wave velocity models obtained from the inversion of the original dispersion data in Figure 35 for block 13 and the SNECB (D'Annolfo, 1992).

SNECB (D'Annolfo, 1992):

Resolution:	0.03	0.12	0.04	0.04	0.04
	0.12	0.65	0.06	-0.16	0.09
	0.04	0.06	0.92	0.07	-0.08
	0.04	-0.16	0.07	0.79	0.17
	0.04	0.09	-0.08	0.17	0.71
Variance: (km/sec)	0.0009	0.0024	0.0014	0.0020	0.0023

Hartford Basin (Block #13):

Resolution:	0.91	0.17	-0.10
	0.17	0.53	0.23
	-0.10	0.23	0.67
Variance: (km/sec)	0.025	0.042	0.040

Table 11 The resolution and variance for the shear wave velocity models obtained for study area A.

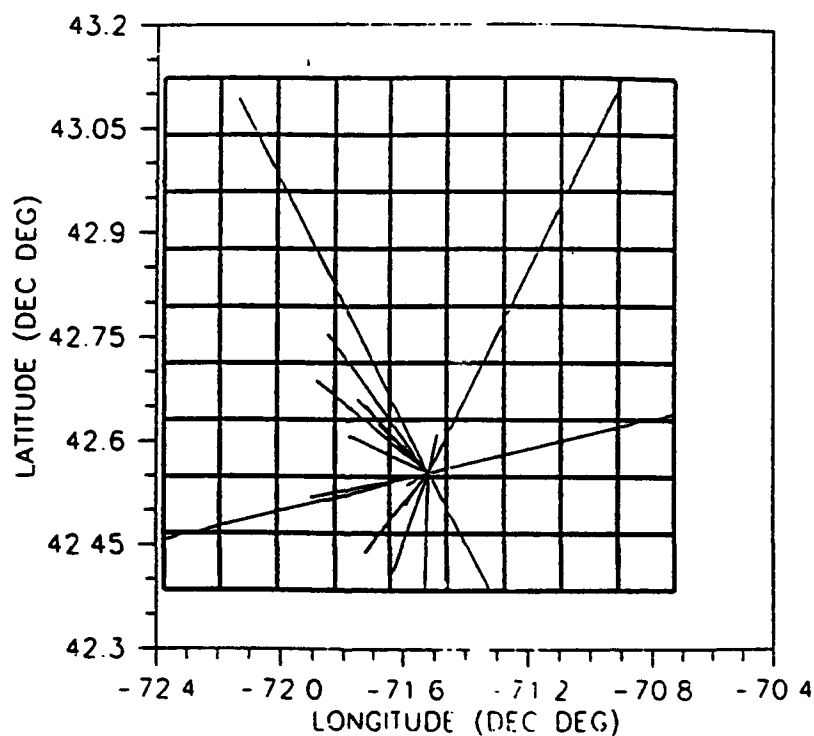
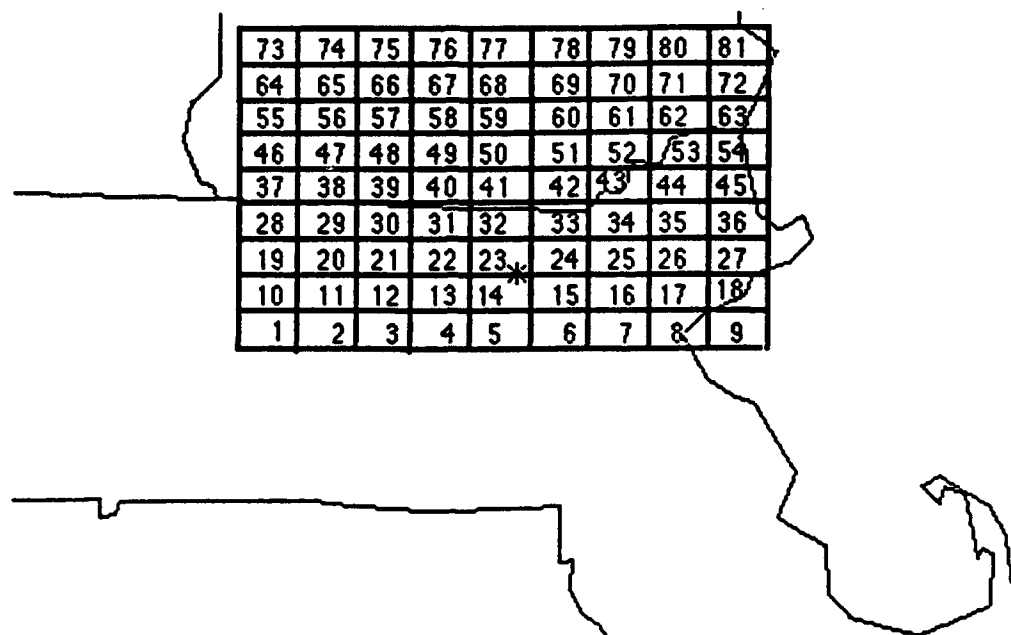


Figure 37 Study area B: (Top) Divided into 81 blocks (* = location of the San-Vel/Lonestar Quarry), and (bottom) paths at $T=0.7$ superimposed over the 9×9 block structure. Curvature of the earth is not taken into account.

The paths represented by the data values (data set B1_07.DAT) at a period of 0.7 sec are shown in Figure 37. For this case, many blocks do not contain any path segments. The group velocity for each of these blocks with no path segments is assigned the group velocity of the initial model and remains constant throughout the tomographic analysis.

The SVD method is used to obtain Rg group velocities at periods of 0.5, 0.7, 0.9, and 1.1 sec. As in the case of the 5x6 block structure for study area A, the density and distribution of path segments are quite high for some blocks, but quite low for others. Therefore, eigenvalues are excluded from the tomographic analysis at some periods, in the same way as was done in the tomographic analysis of the 5x6 structure for study area A.

The group velocities and eigenvalue ratio for each period are shown in Figure 38. The group velocity at a period of 0.7 sec for each block is shaded in Figure 39. The resolution of each group velocity (model parameter j) is classified as A, B, C, or D based on the diagonal element of row j. Table 12 indicates how the resolution of each group velocity is classified for periods from 0.5 to 1.1 sec.

The model covariance matrix suggests that the assumptions for the data covariance matrix are not valid for some of the group velocities from these tomographic analyses (as was the case for the 5x6 structure for study area A). Nevertheless, the diagonal elements for each group velocity, along with information on whether these elements are larger than the other elements in their row, are given in Table 13.

The dispersion data for the blocks that exhibit "high quality" normal dispersion are shown in Figure 40. Considering only these blocks, Figure 39 is redrawn in Figure

*	2.71	*	*	*	*	*	2.67	2.49
*	2.73	2.56	*	*	*	*	2.71	*
*	*	3.87	*	*	*	2.65	2.50	*
*	*	2.71	2.58	*	*	2.71	*	*
*	*	2.31	2.53	*	2.64	2.51	*	*
*	*	**	2.60	2.60	2.72	*	*	2.54
*	*	*	2.41	2.40	2.73	2.65	2.65	2.55
2.56	2.68	2.43	2.35	2.47	2.46	*	*	*
2.55	*	*	2.31	2.53	2.46	*	*	*

* indicates no path segments
 ** indicates that the group velocity
 for this block is greater than 3.5
 4.0 km/sec

T = 0.5 sec
 Eigenvalue Ratio = 0.00001

*	2.87	*	*	*	*	*	2.72	2.56
*	2.91	2.67	*	*	*	*	2.76	*
*	*	3.10	*	*	*	2.71	2.57	*
*	*	2.87	2.69	*	*	2.76	*	*
*	*	2.14	2.23	*	2.70	2.58	*	*
*	*	**	2.70	2.72	2.76	*	*	2.58
*	*	*	2.87	2.39	2.73	2.66	2.66	2.59
2.74	2.98	2.34	2.57	2.54	2.51	*	*	*
2.72	*	*	2.38	2.64	2.49	*	*	*

T = 0.7 sec
 Eigenvalue Ratio = 0.0300

*	2.94	*	*	*	*	*	2.76	2.62
*	2.98	2.74	*	*	*	*	2.79	*
*	*	3.17	*	*	*	2.75	2.63	*
*	*	2.95	2.77	*	*	2.79	*	*
*	*	2.20	2.28	*	2.74	2.64	*	*
*	*	**	2.73	2.79	2.79	*	*	2.65
*	*	*	2.97	2.49	2.77	2.71	2.71	2.65
2.62	2.64	2.84	2.65	2.57	2.63	*	*	*
2.62	*	*	2.49	2.82	2.68	*	*	*

T = 0.9 sec
 Eigenvalue Ratio = 0.0300

*	2.73	*	*	*	*	*	2.82	2.69
*	2.74	2.69	*	*	*	*	2.85	*
*	*	2.77	*	*	*	2.81	2.70	*
*	*	2.73	2.70	*	*	2.86	*	*
*	*	2.93	3.35	*	2.80	2.71	*	*
*	*	**	2.47	2.70	2.86	*	*	2.69
*	*	*	2.97	2.58	2.78	2.73	2.73	2.69
2.73	2.81	2.80	2.77	2.61	*	*	*	*
2.73	*	*	2.53	3.15	*	*	*	*

T = 1.1 sec
 Eigenvalue Ratio = 0.00001

Figure 38 Study area B: Group velocity results.

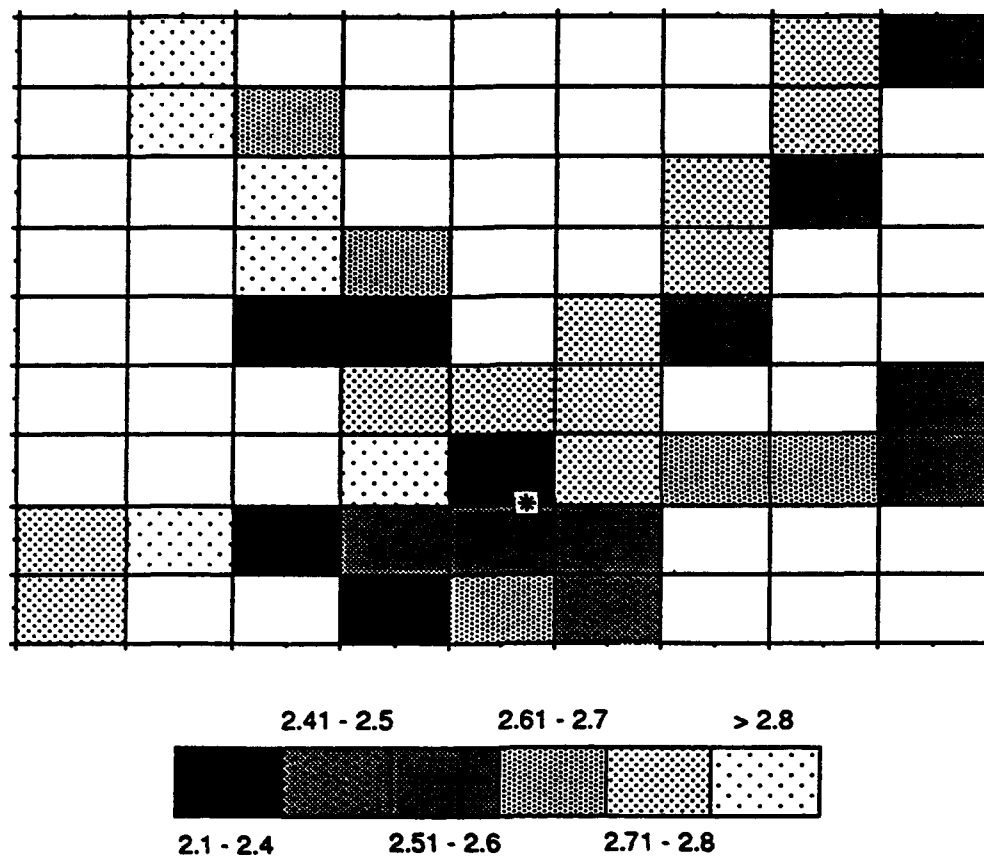


Figure 39 Study area B: Dispersion results.

BLOCK #	PERIOD			
	0.5 SEC	0.7 SEC	0.9 SEC	1.1 SEC
1	D	D	D	D
2	NA	NA	NA	NA
3	NA	NA	NA	NA
4	A	A	A	A
5	A	A	A	A
6	A	A	A	NA
7	NA	NA	NA	NA
8	NA	NA	NA	NA
9	NA	NA	NA	NA
10	D	D	D	D
11	B	B	B	B
12	A	A	A	A
13	A	A	A	A
14	A	A	A	A
15	D	D	D	NA
16	NA	NA	NA	NA
17	NA	NA	NA	NA
18	NA	NA	NA	NA
19	NA	NA	NA	NA
20	NA	NA	NA	NA
21	NA	NA	NA	NA
22	A	A	A	A
23	A	A	A	A
24	D	D	D	D
25	D	D	D	D
26	D	D	D	D
27	D	D	D	D
28	NA	NA	NA	NA
29	NA	NA	NA	NA
30
31	A	A	A	A
32	D	D	D	D
33	D	D	D	D
34	NA	NA	NA	NA
35	NA	NA	NA	NA
36	D	D	D	D
37	NA	NA	NA	NA
38	NA	NA	NA	NA
39	D	D	D	D
40	B	C	C	B
41	NA	NA	NA	NA
42	D	D	D	D
43	D	D	D	D
44	NA	NA	NA	NA

Table 12 Resolution of group velocities for study area B using a 9x9 block structure.

BLOCK #	PERIOD			
	0.5 SEC	0.7 SEC	0.9 SEC	1.1 SEC
45	NA	NA	NA	NA
46	NA	NA	NA	NA
47	NA	NA	NA	NA
48	D	D	D	D
49	D	D	D	D
50	NA	NA	NA	NA
51	NA	NA	NA	NA
52	D	D	D	D
53	NA	NA	NA	NA
54	NA	NA	NA	NA
55	NA	NA	NA	NA
56	NA	NA	NA	NA
57	C	C	C	C
58	NA	NA	NA	NA
59	NA	NA	NA	NA
60	NA	NA	NA	NA
61	D	D	D	D
62	D	D	D	D
63	NA	NA	NA	NA
64	NA	NA	NA	NA
65	D	D	D	D
66	D	D	D	D
67	NA	NA	NA	NA
68	NA	NA	NA	NA
69	NA	NA	NA	NA
70	NA	NA	NA	NA
71	D	D	D	D
72	NA	NA	NA	NA
73	NA	NA	NA	NA
74	D	D	D	D
75	NA	NA	NA	NA
76	NA	NA	NA	NA
77	NA	NA	NA	NA
78	NA	NA	NA	NA
79	NA	NA	NA	NA
80	D	D	D	D
81	D	D	D	D

NA indicates that the block did not contain any path segments

** indicates that the group velocity for the block was greater than 10 km/sec

Table 12 Resolution of group velocities for study area B using a 9x9 block structure.

BLOCK #	T = 0.5 SEC		T = 0.7 SEC		PERIOD T = 0.9 SEC		T = 1.1 SEC	
	()		()		()		()	
1	0.00		0.00		0.00		0.00	
2	NA		NA		NA		NA	
3	NA		NA		NA		NA	
4	0.00	*	0.00	*	0.00	*	0.00	*
5	0.00	*	0.00	*	0.00	*	0.00	*
6	0.00	*	0.00	*	0.00	*	NA	
7	NA		NA		NA		NA	
8	NA		NA		NA		NA	
9	NA		NA		NA		NA	
10	0.00		0.00		0.00		0.00	
11	0.00	*	0.00	*	0.00	*	0.00	*
12	0.00	*	0.00	*	0.00	*	0.00	*
13	0.00	*	0.00	*	0.00	*	0.00	*
14	0.00	*	0.00	*	0.00	*	0.00	*
15	0.00		0.00		0.00		NA	
16	NA		NA		NA		NA	
17	NA		NA		NA		NA	
18	NA		NA		NA		NA	
19	NA		NA		NA		NA	
20	NA		NA		NA		NA	
21	NA		NA		NA		NA	
22	0.00	*	0.00	*	0.00	*	0.00	*
23	0.00		0.00		0.00		0.00	
24	0.00		0.00		0.00		0.00	
25	0.00		0.00		0.00		0.00	
26	0.00		0.00		0.00		0.00	
27	0.00		0.00		0.00		0.00	
28	NA		NA		NA		NA	
29	NA		NA		NA		NA	
30	1.45	*	0.43	*	0.41	*	**	*
31	0.00	*	0.00	*	0.00	*	0.00	*
32	0.00		0.00		0.00		0.00	
33	0.00		0.00		0.00		0.00	
34	NA		NA		NA		NA	
35	NA		NA		NA		NA	
36	0.00		0.00		0.00		0.00	
37	NA		NA		NA		NA	
38	NA		NA		NA		NA	
39	0.00		0.00		0.00		0.00	
40	0.00	*	0.00	*	0.00	*	0.00	*
41	NA		NA		NA		NA	
42	0.00		0.00		0.00		0.00	
43	0.00		0.00		0.00		0.00	
44	NA		NA		NA		NA	
45	NA		NA		NA		NA	

Table 13 Variance of group velocities for study area B using a 9x9 block structure.

BLOCK #	PERIOD			
	T = 0.5 SEC (°)	T = 0.7 SEC (°)	T = 0.9 SEC (°)	T = 1.1 SEC (°)
46	NA	NA	NA	NA
47	NA	NA	NA	NA
48	0.00	0.00	0.00	0.00
49	0.00	0.00	0.00	0.00
50	NA	NA	NA	NA
51	NA	NA	NA	NA
52	0.00	0.00	0.00	0.00
53	NA	NA	NA	NA
54	NA	NA	NA	NA
55	NA	NA	NA	NA
56	NA	NA	NA	NA
57	0.00	0.00	0.00	0.00
58	NA	NA	NA	NA
59	NA	NA	NA	NA
60	NA	NA	NA	NA
61	0.00	0.00	0.00	0.00
62	0.00	0.00	0.00	0.00
63	NA	NA	NA	NA
64	NA	NA	NA	NA
65	0.00	0.00	0.00	0.00
66	0.00	0.00	0.00	0.00
67	NA	NA	NA	NA
68	NA	NA	NA	NA
69	NA	NA	NA	NA
70	NA	NA	NA	NA
71	0.00	0.00	0.00	0.00
72	NA	NA	NA	NA
73	NA	NA	NA	NA
74	0.00	0.00	0.00	0.00
75	NA	NA	NA	NA
76	NA	NA	NA	NA
77	NA	NA	NA	NA
78	NA	NA	NA	NA
79	NA	NA	NA	NA
80	0.00	0.00	0.00	0.00
81	0.00	0.00	0.00	0.00

NA indicates that the block did not contain any path segments

** indicates that the group velocity for the block was greater than
10 km/sec

Table 13 Variance of group velocities for study area B using a 9x9 block structure.

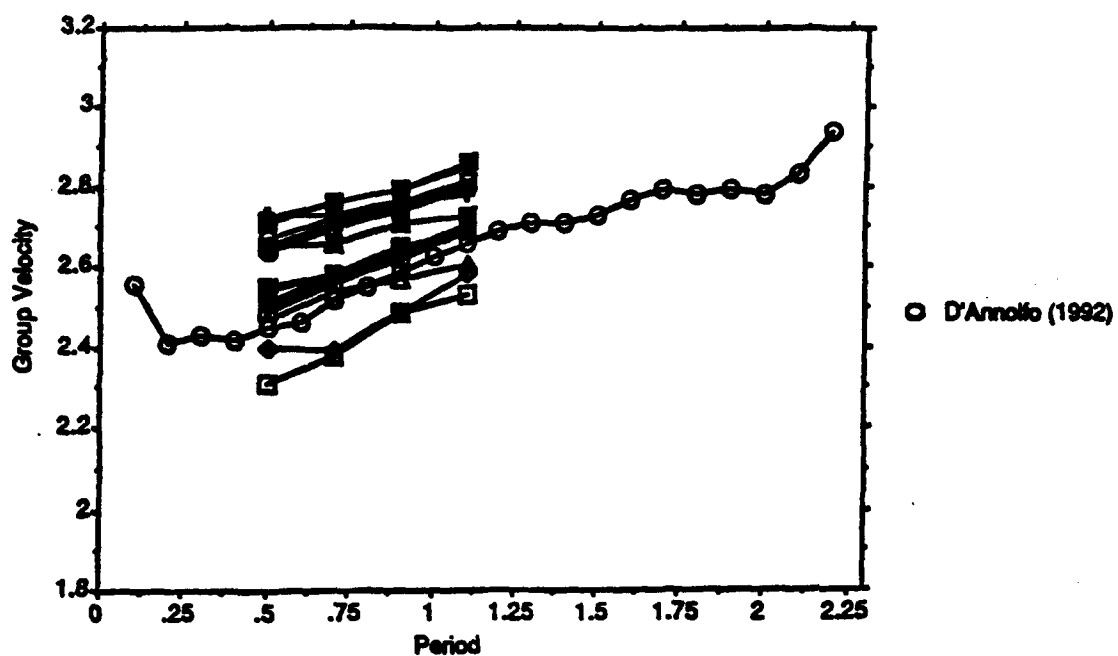


Figure 40 Study area B: Dispersion curves for blocks exhibiting "high quality" normal dispersion.

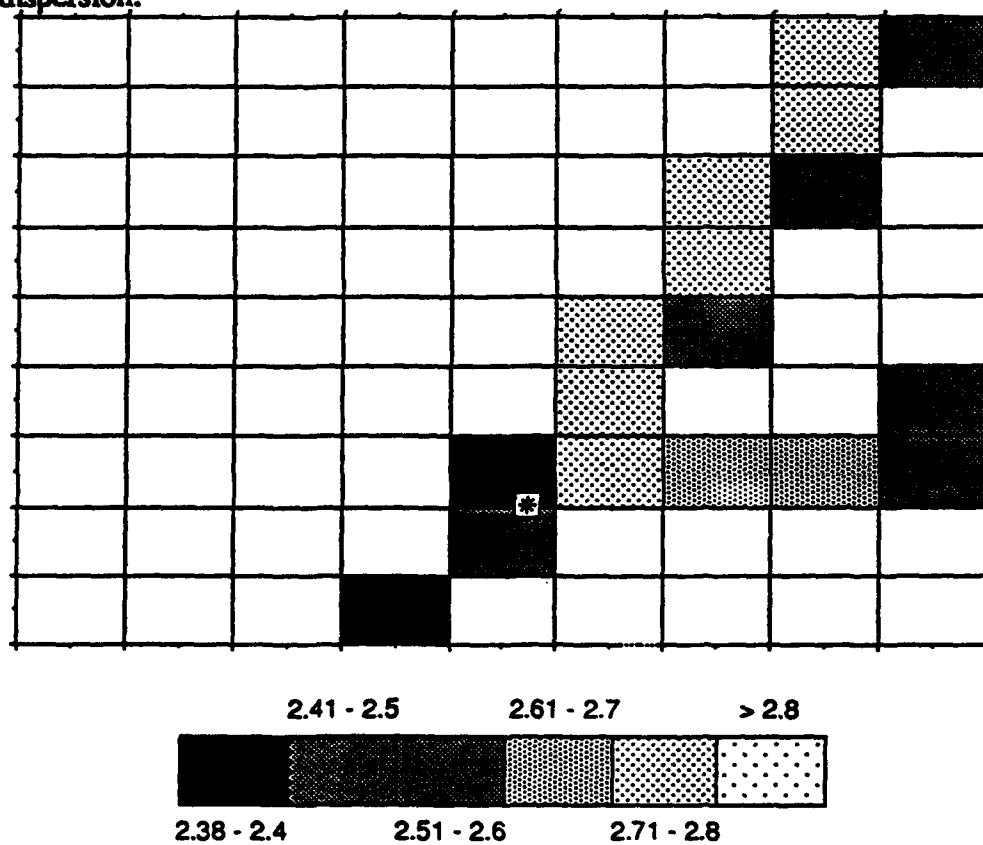


Figure 41 Study area B: Dispersion results (shaded blocks exhibit "high quality" normal dispersion).

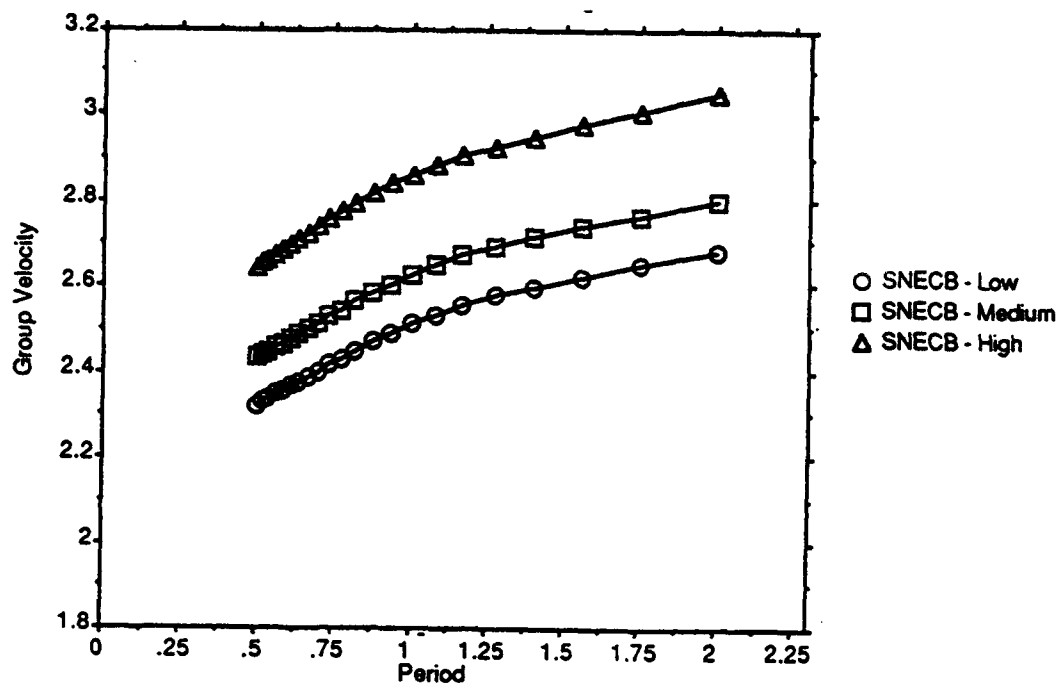


Figure 42 Study area B: Three dispersion curves predicted by the shear wave velocity models in Figure 43.

41. The dispersion shown in Figure 41 appears to fall into three categories: slightly higher than, slightly lower than, and virtually the same as the average dispersion observed for the SNECB.

8.2.2 Shear-Wave Velocity Models for Study Area B

Shear wave velocity models were obtained from the dispersion curves shown in Figure 40 by using the combined inversion/forward modelling procedure described in Section 7.2.2 (Figures 42 and 43). The model in Figure 43 with the lowest shear wave velocities corresponds approximately to the dispersion curve from blocks 4 and 23. The intermediate velocity model in Figure 43 corresponds to the dispersion curves of blocks that appear to be underlain by a structure similar to that of the average SNECB. The high velocity model in Figure 43 corresponds to the highest velocity dispersion curves (block 52). The dispersion curves predicted by these models are shown in Figure 42.

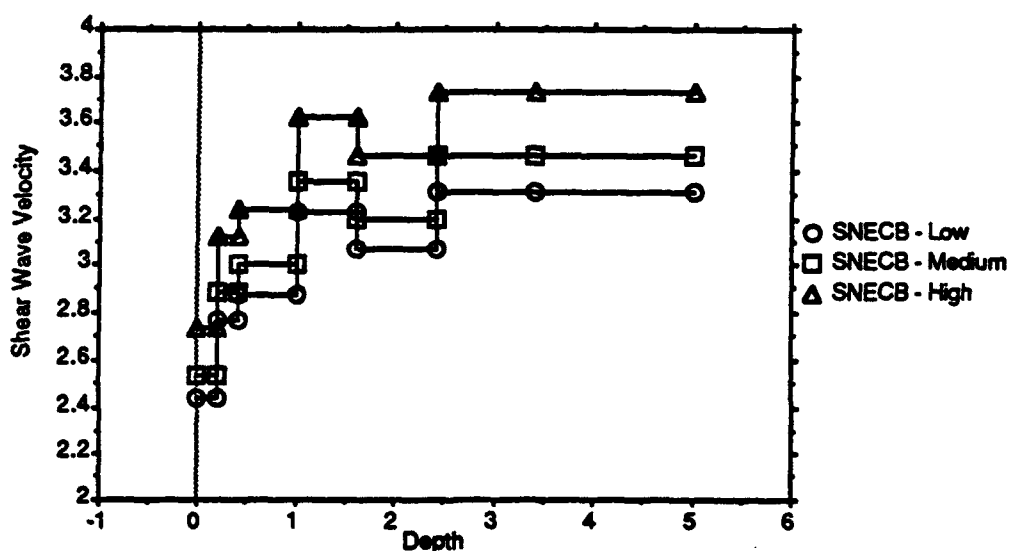


Figure 43 Study area B: Shear wave velocity models corresponding to the dispersion curves shown in Figure 42.

9. Conclusions

In spite of the very large amount of scatter in the group velocity data, to what extent can tomographic analyses of that data provide an estimate of the lateral variation in dispersion across SNE? This question can be answered in as much detail as can be characterized by the chosen block structure(s) and the path information in SNE. By examining the group velocity results for each block structure along with the resolution and variance with which each group velocity is determined, conclusions can be made regarding the question of lateral variation in Rg dispersion for SNE. After the dispersion characteristics have been estimated for SNE, the three dimensional variation of the shear wave velocity structure beneath SNE can be investigated.

9.1 Study Area A

9.1.1 Lateral Variation Across Study Area A

Lateral variation of Rg dispersion appears to exist within study area A, at least at the level of detail characterized by the 3x2 and 5x6 block structures. In this section, the dispersion data from both block structures are compared with published studies of Rg dispersion, and are discussed in terms of the mapped lithotectonic terranes of SNE [Figure 15].

The 3x2 Block Structure

The 3x2 block structure divides study area A into six blocks. Blocks 1, 2, 3, and 6 exhibit "high quality" normal dispersion. Dispersion for blocks 1, 3, and 6 are similar to that for the SNECB, while dispersion exhibited by block 2 is slightly lower.

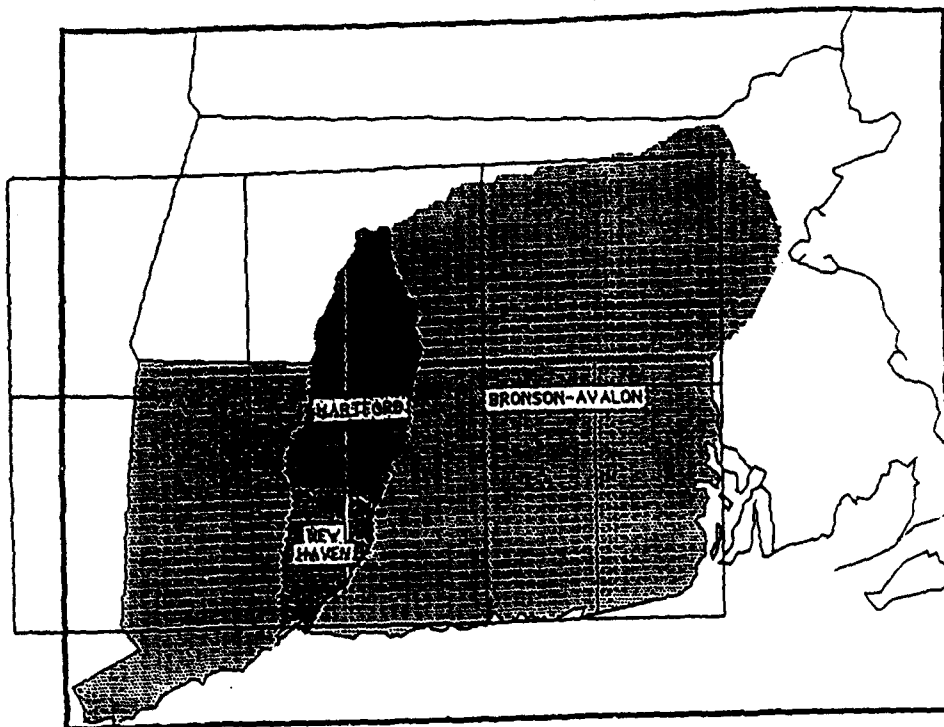
In Figure 44(A), this block structure is superimposed over the dispersion results

from previous studies (e.g. Kafka and Skehan, 1990). Block 2 contains both the HDR and the NHDR. These studies have suggested that the average dispersion curve published for the HDR and the NHDR are lower than the average dispersion curve for the SNECB. In Figure 45(A), this block structure is superimposed over the mapped lithotectonic terranes in SNE [also see Figure 15]. The HRB in Connecticut, the only regional sedimentary terrane in SNE, is entirely contained within block 2. Dispersion exhibited by block 2 is slightly lower than the average dispersion curve for the SNECB as would be expected for a block superimposed over a sedimentary basin. The agreement between the dispersion results of this study and those of previous studies as well as the correlation between my results and the geology of the HRB suggest that block 2 has successfully isolated the subregion covering the HRB in Connecticut and its dispersion characteristics from the rest of SNE.

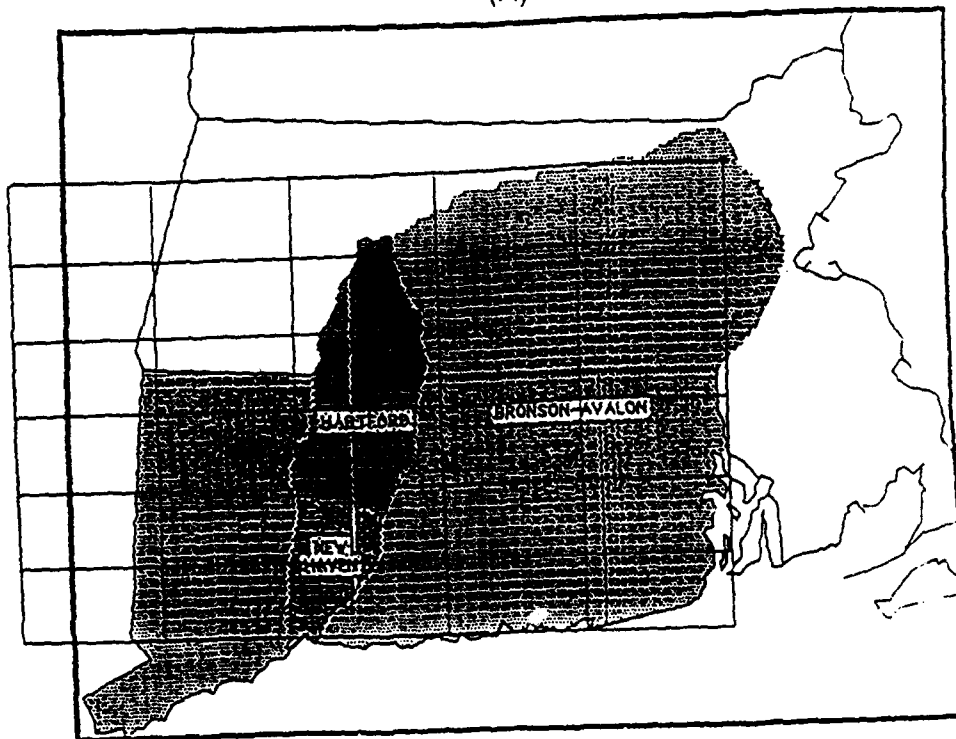
The 5x6 Block Structure

The 5x6 block structure divides study area A into thirty blocks. Blocks 3, 9, 13, 14, 29, and 30 exhibit "high quality" dispersion. With the exception of block 13, these blocks exhibit dispersion similar to that for the average SNECB. Group velocities for block 13 are dramatically lower.

In Figure 44(B), this block structure is superimposed over the dispersion results from previous studies (e.g. Kafka and Skehan, 1990). Block 13 contains the HDR in Connecticut. These studies have suggested that the dispersion curve published for the HDR is dramatically lower than that for any other part of the SNECB and slightly lower than the dispersion curve for the NHDR. Dispersion exhibited by block 13 is



(A)



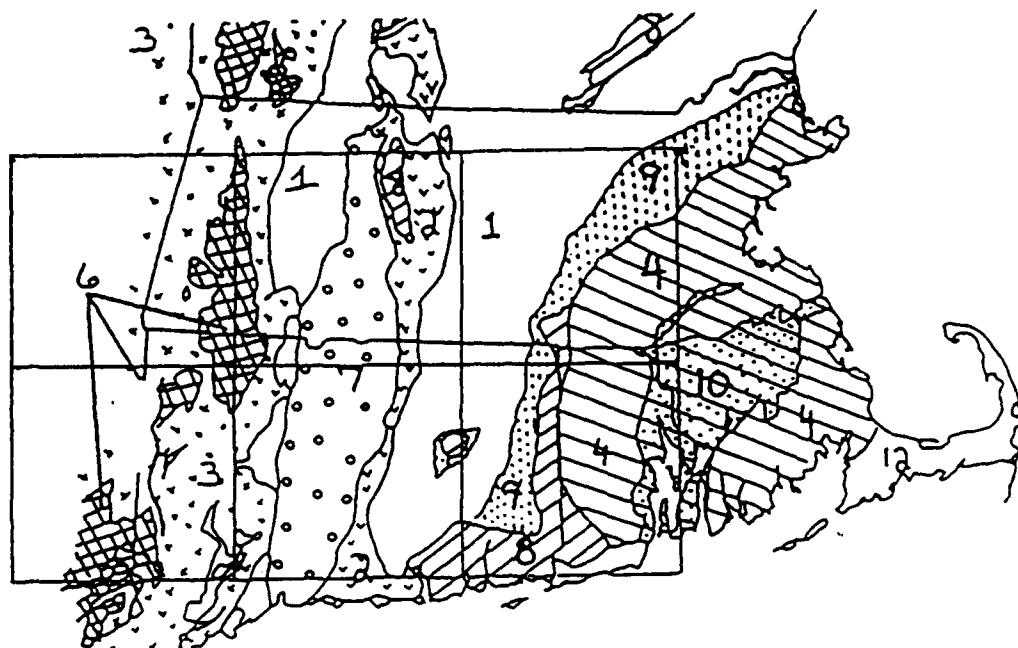
(B)

Figure 44 Study area A: Dispersion results from previous studies (e.g. kafka and Skehan, 1990) superimposed over (A) the 3x2 block structure and (B) the 5x6 block structure.

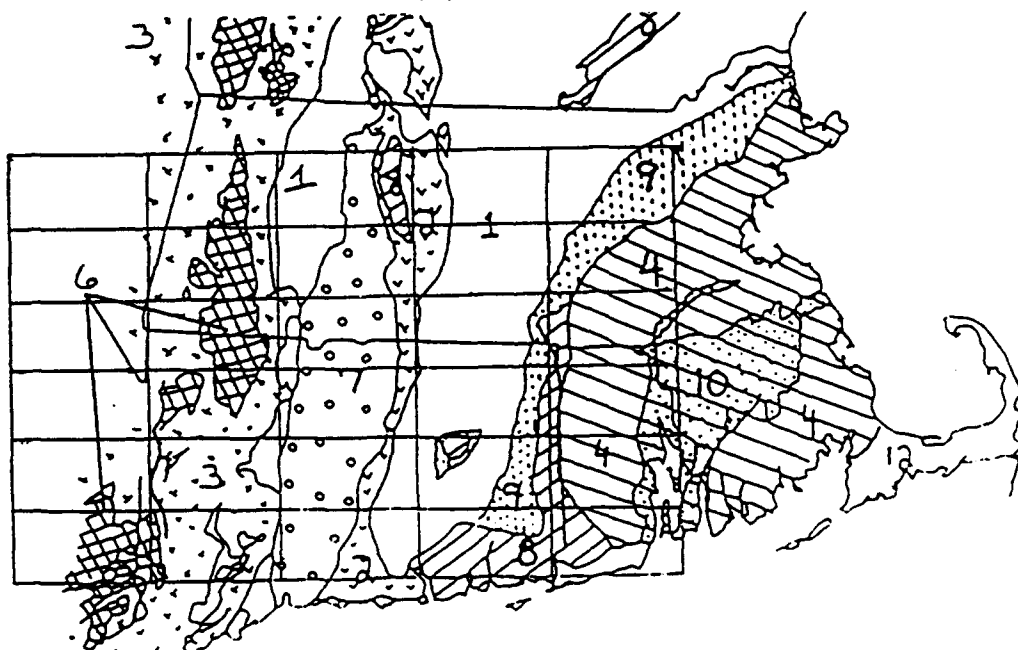
dramatically lower than the average SNECB dispersion curve. In Figure 45(B), this block structure is superimposed over the mapped lithotectonic terranes in SNE. The northern part of the HRB in Connecticut, where the sedimentary sequence is thicker than in the southern part of the HRB (Wenk, 1984), is entirely contained within block 13. Dispersion exhibited by block 13 is dramatically lower than the average dispersion curve for the SNECB as would be expected. The agreement between the dispersion results of this study and those of previous studies as well as the correlation between my results and the geology of the HRB suggest that block 13 has successfully isolated the subregion covering the northern part of the HRB in Connecticut and its dispersion characteristics from the rest of SNE.

As discussed in Section 8, dispersion results corresponding to some blocks within study area A have satisfied my criteria for being considered "high quality" dispersion. These results suggest lateral variation in group velocity across study area A, at least in the data, if not in the earth. Furthermore, the subregion overlying the HRB in CT exhibits distinctly lower group velocities than the rest of study area A. Group velocities in the southern part of the HRB in CT are higher than in the northern part of the HRB in CT, but similar to those of the SNECB. Previous studies (e.g. Kafka and Skehan, 1990; Wenk, 1984) are in full agreement with the results of this study. Furthermore, the dispersion results for blocks that contain part of the HRB are lower than the average SNECB dispersion curve, indicating a correlation between the dispersion results and the mapped lithotectonic terranes in Figure 15.

9.1.2 Three-Dimensional Variation in Shear Wave Velocity within Study Area A



(A)



(B)

Figure 45 Study area A: Regional geology superimposed over (A) the 3x2 block structure, and (B) the 5x6 block structure.

The results of the tomographic inversion provide a basis for investigating the extent to which three-dimensional variation in shear wave velocities exists across study area A. Shear wave velocities in the shallow crust underlying the northern part of the HRB in CT are distinctly lower than those observed for the rest of study area A [Figure 36]. There appears to be very little difference between the shear wave velocity structure underlying the southern end of the HRB and that underlying the rest of study area A.

9.2 Study Area B

9.2.1 Lateral Variation Across Study Area B

Lateral variation of Rg dispersion appears to exist within study area B, at least at the level of detail characterized by the 9x9 block structure. In this section, the dispersion data for this block structure is compared with results of previously published studies of Rg dispersion in SNE. The results are also discussed in terms of the lithotectonic terranes of SNE.

The 9x9 Block Structure

The 9x9 block structure divides study area B into 81 blocks. Blocks 4, 14, 23, 24, 25, 26, 27, 33, 36, 42, 43, 52, 61, 62, 71, 80, and 81 exhibit "high quality" normal dispersion. For the period range analyzed, the dispersion curves for these blocks are similar in shape to that of the average SNECB dispersion curve. However, dispersion data for the 9x9 block structure exhibits significant variation with three distinct clusters: higher than, lower than, and similar to that for the SNECB.

In Figure 46, this block structure is superimposed over the dispersion results published by D'Annolfo (1992). Most previous studies (e.g. Kafka and Skehan, 1990)

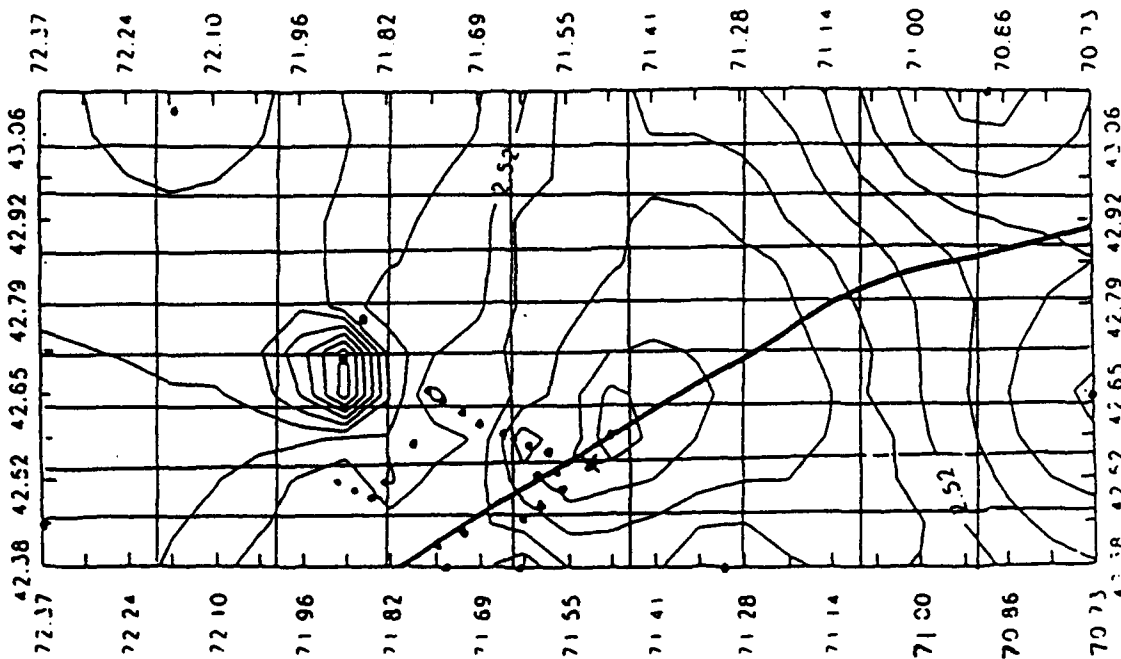


Figure 46 Study area B: Dispersion results from D'Annolfo (1992) superimposed over the 9x9 block structure.

have been unable to identify lateral variation in Rg group velocities within the SNECB. D'Annolfo (1992), on the other hand, has suggested that there is indeed lateral variation in the area covered by the 9x9 block structure. Specifically, she concluded that the group velocities in the immediate area surrounding the San-Vel/Lonestar Quarry are lowest, and that group velocities systematically increase with distance from the quarry. This study suggests this as well.

In Figure 47, this block structure is superimposed over the mapped lithotectonic terranes. The results of this study do not reveal any particular pattern of correlation

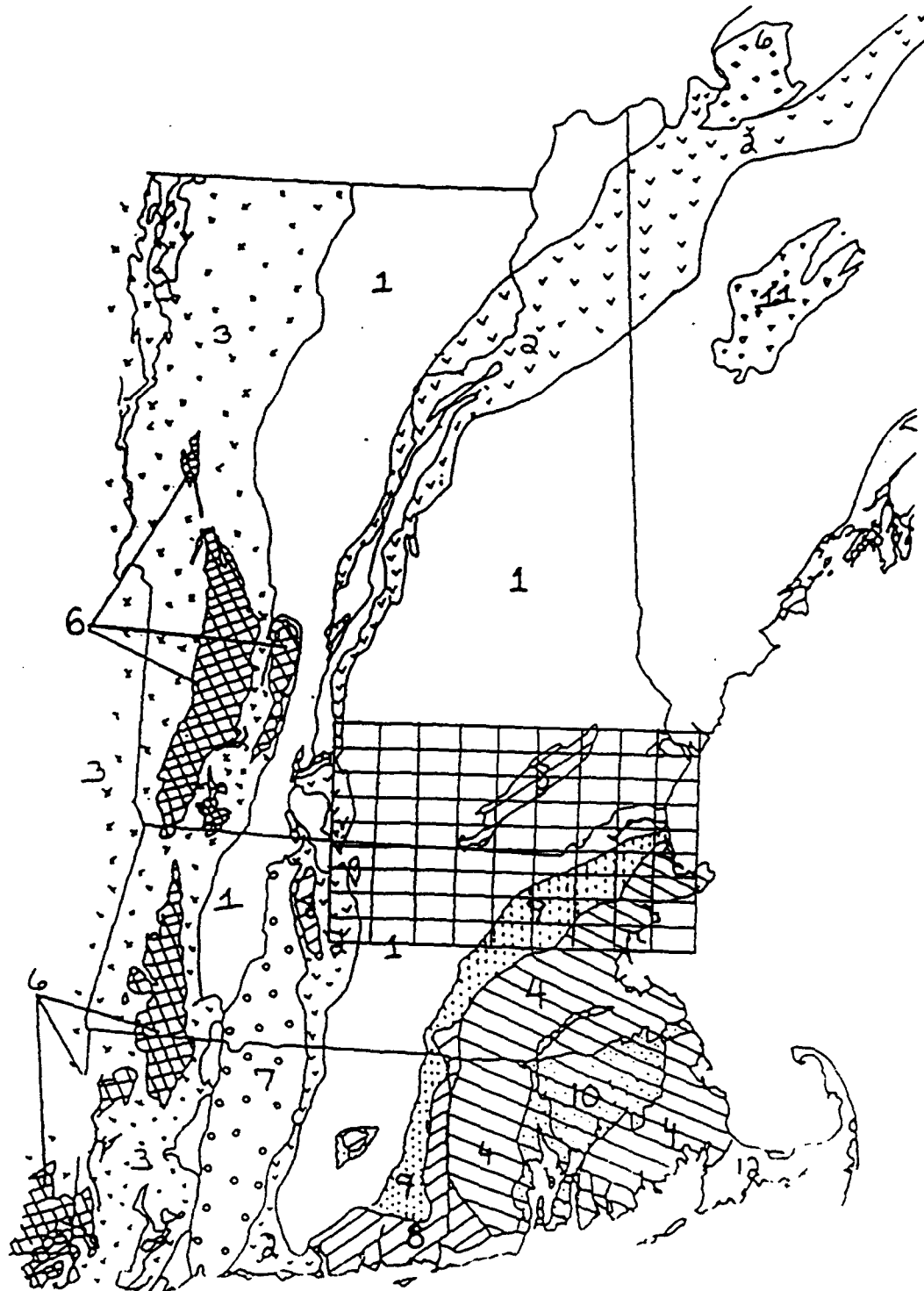


Figure 47 Study area B: Regional geology superimposed over the 9x9 block structure.

between the group velocity and geologic features or lithotectonic terranes. One plausible explanation can be found in the relationship between the size of the blocks and the size of the mapped geologic features. If the size of the blocks is roughly the same as the average size of the mapped geologic features, the detail characterized by the blocks and the mapped geologic features are roughly the same. The group velocity information can be correlated with the mapped geologic features. If the size of the blocks is significantly different than the average size of the mapped geologic features, the detail characterized by the blocks and the mapped geology are significantly different. The group velocity information and mapped geology cannot be correlated unless the mapped geologic features are roughly the same size as the blocks.

9.2.2 Three-Dimensional Variation in Shear Wave Velocity within Study Area B

The results of the tomographic inversion provide a basis for investigating the extent to which three dimensional variation in shear wave velocities exists across study area B. The southern half of study area B contains the SNECB. Slight variations in shear wave velocity are observed within the SNECB in study area B because of the great level of detail characterized by the 9x9 block structure.

9.3 Effectiveness of Tomographic Analyses and Inversion Methods in the Determination of Three-Dimensional Velocity Variation

The results of this study illustrate how effective computer tomography is in the determination of shallow crustal velocities from Rg dispersion data. In a tomographic analysis, a subregion(s) and its velocity structure can be effectively isolated from the rest of the study area. The size and location of this subregion(s) is chosen based on 1)

whether the path information for the study area is sufficient to give results for the subregion(s), and 2) what features (e.g. lithotectonic terranes, dispersion results from previous studies, and gravity anomalies) the researcher wants to isolate.

This study also indicates that the inversion methods used in this study are less sensitive to large variations in observed Rg travel times than other methods previously used in dispersion and shear wave velocity studies. The observed Rg travel times used in this study have been taken from many sources. Measurements of observed Rg travel times for some of the repeated paths in this study contain a large amount of scatter. A tomographic inversion uses observed Rg travel time information from several different paths, thereby reducing the effects of the scatter observed along a single path. Thus, the tomographic inversions discussed in this study make it possible to systematically analyze all Rg travel time information, regardless of the scatter observed along one or more paths, and to investigate the extent to which the "signal" can be extracted from the "noise".

10. Future Work

This study, to a large extent, has addressed the questions discussed in the introduction about lateral variation in Rg group velocities and three dimensional variation of shear wave velocities in SNE. To more completely address these questions in the future, I propose modifications to 1) the tomographic inversion program SURFTOMO, 2) the analysis of lateral and vertical variation in velocity, and 3) the interpretation of the results of this analysis.

10.1 Modifications to the Tomographic Inversion Program SURFTOMO

Two specific problems that I encountered in this study require three modifications to SURFTOMO, respectively. The first problem arises when the study area is not located at the equator. Study areas A and B are obviously not located at the equator. This study has presented these regions and the blocks of each block structure as strictly rectangular. However, due to the curvature of the earth, the study area and blocks are not rectangular. In SURFTOMO, the study area is divided into blocks based on a baseline drawn along the lower latitudinal and higher latitudinal lines. Therefore, the boundaries of the blocks are drawn such that the blocks are not rectangular.

Secondly, the boundaries of the blocks for a specific block structure rarely coincide with the boundaries established by the regional geology and/or dispersion regions outlined by previous studies. Furthermore, none of the lithotectonic terranes, geologic formations, and dispersion regions in any study area are ideally rectangular.

I propose two modifications to SURFTOMO to address these three problems. First, the latitudinal and longitudinal boundaries chosen for the study area and blocks should be corrected for their respective distances away from the equator. Secondly, the shape and size of each block in a study area should be flexible enough for its boundaries to coincide with the boundaries of terranes, formations, or dispersion regions. Alternatively, the velocity information from several block structures can be integrated to form a more complete description of group velocities across a study area.

10.2 Modifications to the Interpretation of Velocity Results from the Analysis

The results produced from a tomographic inversion includes one vector and two matrices: the model parameter vector, and the model resolution and covariance matrices.

In cases where the block structure divides the study area into only a few blocks, these matrices are small. For example, the result from a 3x2 block structure produces a vector of length 6 and two matrices of dimensions 6 by 6. However, in cases where more detailed velocity information must be determined for a study area, the more detailed 9x9 block structure produces a vector of length 81 and two matrices of dimensions 81 by 81.

To assess whether there is lateral variation between a given block and each adjacent block, one must compare the results of that block to those of each adjacent block. This assessment should be done for all blocks in a block structure that exhibit "high quality" dispersion. Often the study area must be divided into many blocks, so that the group velocity results of a tomographic inversion can be correlated with either the mapped geology and/or previous studies. Such a detailed assessment is more efficiently done by a computer program. This program would allow the researcher to 1) select a subset of this information in a timely manner, and 2) systematically analyze this subset of information.

10.3 Modifications to the Analysis of Lateral Variation of Group Velocity

In Sections 5 and 6, three approaches to inversion were outlined. For the determination of lateral variation in R_g group velocity, the SVD method and weighted damped least squares were described. For the determination of three dimensional variation in shear wave velocity, the maximum likelihood method was described. As part of the determination of both lateral and vertical variation, the results of all three methods should be compared. Although the results of all three methods will most likely be similar to those discussed in this study, the determination of velocity variation would be

more extensive and complete.

References

- Bath, M. (1979). *Introduction to Seismology*, Birkhauser, Stockholm, Sweden.
- Chiburis, E.F., Ahner, R. O., and T. Graham (1977). Preliminary travel-time model of southern New England, *Earthquake Notes (Abstract)* **49**, 11.
- D'Annolfo, S. (1992). Investigation of lateral variation in the seismic velocity structure of the shallow crust beneath eastern Massachusetts and southern New Hampshire, *Master's Thesis*, Boston College, Weston, MA.
- Dollin, M. (1984). The use of Rg waves to constrain crustal velocity structure in Connecticut, *Master's Thesis*, Boston College, Weston, MA.
- Dziewonski, A.M., Block, S. and M. Landisman (1969). A technique for the analysis of transient seismic signals, *Bull. Seis. Soc. Am.* **59**, 427.
- Gnewuch, S. C. (1987). Investigation of velocity and anelastic attenuation structures of the shallow crust in New England by time domain modeling of Rg waves, *Master's Thesis*, Boston College, Weston, MA.
- Hatcher, Jr., R. D., Thomas, W. A., and G. W. Viele (1989). The Appalachian-Ouachita Orogen in the United States, *The Geological Society of America, Inc.*, Boulder, CO.
- Kafka, A. L. (1988). Earthquakes, geology and crustal features in southern New England, *Seismol. Res. Lett.* **59**(4), 173-181.
- Kafka, A. L. (1990). Rg as a depth discriminant for earthquakes and explosions: A case study in New England, *Bull. Seis. Soc. Am.* **80**(2), 373 - 394.
- Kafka, A. L. and A. K. Bowers (1991). Corrections to Rg group velocity dispersion in southwestern New England, *Seismol. Res. Lett.* **62**, 221-23
- Kafka, A. L., and M. F. Dollin (1985). Constraints on lateral variation in upper crustal structure beneath southern New England from the dispersion of Rg waves, *Geophys. Res. Lett.* **12**, 235-238.
- Kafka, A. L. and M. R. Jacobson-Carroll (1992). Variation of amplitudes and waveforms of seismic phases recorded by a small-aperture array surrounding Weston Observatory, Phillips Laboratory and Defense Advanced Research Projects Agency, Seismic Research Symposium. PL-TR-92-2210, ADA256711

- Kafka, A. L. and E. C. Reiter (1987). Dispersion of Rg waves in southeastern Maine: Evidence for lateral anisotropy in the shallow crust, *Bull. Seismol. Soc. Am.* **77**, 925-941.
- Kafka, A. L. and J. W. Skehan, S.J. (1990). Major geological features and lateral variation of crustal structure in southern New England, *Tectonophysics* **178**, 183-192.
- McTigue, J. W. (1986). Modeling upper crustal structure in southern New England using short period Rg waves, *Master's Thesis*, Boston College, Weston, MA.
- Menke, W. (1989). Geophysical Data Analysis: Discrete Inverse Theory, Academic Press, Inc., San Diego, CA.
- Pesceckis, L. and L. R. Sykes (1979), P-wave residuals in the northeastern United States and their relationship to major structural features (Abstract), *EOS Trans. Am. Geophys. Un.* **60**, 311
- Press, W. H., Flannery, B. P., Teukolsky, S. A., and W. T. Vetterling (1986). Numerical Recipes: the Art of Scientific Computing, Cambridge University Press, New York, NY.
- Reiter, E. C., M. N. Toksoz and A. M. Dainty (1988). Influence of scattering on seismic waves: velocity and attenuation structure of the upper crust in southeast Maine, Scientific Report, Air Force Geophysics Laboratory, AFGL-TR-88-0094, ADA199131.
- Saikia, C. K., A. L. Kafka, S. C. Gnewuch, and J. W. McTigue (1990). Shear velocity and intrinsic Q structure of the shallow crust in southeastern New England from Rg wave dispersion, *Jour. Geoph. Res.* **95(B6)**, 8527-8541.
- Spotila, J. (1992). Investigation into the current relationship between earthquakes and regional geology/tectonics in the northeastern United States and southeastern Canada, *Senior Thesis*, Boston College, Chestnut Hill, MA
- Taylor, S. R. and M. N. Toksöz (1979). Three-dimensional crust and upper mantle structure of the northeastern United States, *J. Geophys. Res.* **84**, 7627-7644.
- Taylor, S. R. and M. N. Toksöz (1982). Structure in the northeastern United States from inversion of Rayleigh wave phase and group velocities, *Earthquake Notes* **53(4)**, 5-24.
- Tu, Zhiping (1990). A study of Rg wave dispersion in New Hampshire and Vermont, *Master's Thesis*, Boston College, Weston, MA.
- Wenk, W. J. (1984). Seismic refraction model of depth of basement in the Hartford rift

basin, Connecticut and Massachusetts, *Northeastern Geol.* **64**, 196-202.

Zhu, Hong (1991). Tomographic Inversion for the seismic velocity structure beneath northern New England using data from seismic refraction experiments, *Master's Thesis*, Boston College, Weston, MA.

Addendum

Note the following corrections to Appendix A of Bowers (1993). The longitude and latitude of the source of all events listed in data sets B1_*.DAT is 71.517 and 42.554 respectively. The longitude and latitude (71.555, 42.545) listed on pages 227, 229, 231, and 233 is incorrect. This source location was not used in the tomographic analysis; the data used in the analysis, the results, and conclusions drawn from them are correct.

Prof. Thomas Ahrens
Seismological Lab, 252-21
Division of Geological & Planetary Sciences
California Institute of Technology
Pasadena, CA 91125

Prof. Keiiti Aki
Center for Earth Sciences
University of Southern California
University Park
Los Angeles, CA 90089-0741

Prof. Shelton Alexander
Geosciences Department
403 Deike Building
The Pennsylvania State University
University Park, PA 16802

Prof. Charles B. Archambeau
CIRES
University of Colorado
Boulder, CO 80309

Dr. Thomas C. Bache, Jr.
Science Applications Int'l Corp.
10260 Campus Point Drive
San Diego, CA 92121 (2 copies)

Prof. Muawia Barazangi
Institute for the Study of the Continent
Cornell University
Ithaca, NY 14853

Dr. Jeff Barker
Department of Geological Sciences
State University of New York
at Binghamton
Vestal, NY 13901

Dr. Douglas R. Baumgardt
ENSCO, Inc
5400 Port Royal Road
Springfield, VA 22151-2388

Dr. Susan Beck
Department of Geosciences
Building #77
University of Arizona
Tucson, AZ 85721

Dr. T.J. Bennett
S-CUBED
A Division of Maxwell Laboratories
11800 Sunrise Valley Drive, Suite 1212
Reston, VA 22091

Dr. Robert Blandford
AFTAC/TT, Center for Seismic Studies
1300 North 17th Street
Suite 1450
Arlington, VA 22209-2308

Dr. Stephen Bratt
ARPA/NMRO
3701 North Fairfax Drive
Arlington, VA 22203-1714

Dr. Lawrence Burdick
IGPP, A-025
Scripps Institute of Oceanography
University of California, San Diego
La Jolla, CA 92093

Dr. Robert Burridge
Schlumberger-Doll Research Center
Old Quarry Road
Ridgefield, CT 06877

Dr. Jerry Carter
Center for Seismic Studies
1300 North 17th Street
Suite 1450
Arlington, VA 22209-2308

Dr. Eric Chael
Division 9241
Sandia Laboratory
Albuquerque, NM 87185

Dr. Martin Chapman
Department of Geological Sciences
Virginia Polytechnical Institute
21044 Derring Hall
Blacksburg, VA 24061

Mr Robert Cockerham
Arms Control & Disarmament Agency
320 21st Street North West
Room 5741
Washington, DC 20451,

Prof. Vernon F. Cormier
Department of Geology & Geophysics
U-45, Room 207
University of Connecticut
Storrs, CT 06268

Prof. Steven Day
Department of Geological Sciences
San Diego State University
San Diego, CA 92182

Marvin Denny
U.S. Department of Energy
Office of Arms Control
Washington, DC 20585

Dr. Art Frankel
U.S. Geological Survey
922 National Center
Reston, VA 22092

Dr. Zoltan Der
ENSCO, Inc.
5400 Port Royal Road
Springfield, VA 22151-2388

Dr. Cliff Frolich
Institute of Geophysics
8701 North Mopac
Austin, TX 78759

Prof. Adam Dziewonski
Hoffman Laboratory, Harvard University
Dept. of Earth Atmos. & Planetary Sciences
20 Oxford Street
Cambridge, MA 02138

Dr. Holly Given
IGPP, A-025
Scripps Institute of Oceanography
University of California, San Diego
La Jolla, CA 92093

Prof. John Ebel
Department of Geology & Geophysics
Boston College
Chestnut Hill, MA 02167

Dr. Jeffrey W. Given
SAIC
10260 Campus Point Drive
San Diego, CA 92121

Eric Fielding
SNEE Hall
INSTOC
Cornell University
Ithaca, NY 14853

Dr. Dale Glover
Defense Intelligence Agency
ATTN: ODT-1B
Washington, DC 20301

Dr. Petr Firbas
Institute of Physics of the Earth
Masaryk University Brno
Jecna 29a
612 46 Brno, Czech Republic

Dan N. Hagedorn
Pacific Northwest Laboratories
Battelle Boulevard
Richland, WA 99352

Dr. Mark D. Fisk
Mission Research Corporation
735 State Street
P.O. Drawer 719
Santa Barbara, CA 93102

Dr. James Hannon
Lawrence Livermore National Laboratory
P.O. Box 808
L-205
Livermore, CA 94550

Prof Stanley Flatte
Applied Sciences Building
University of California, Santa Cruz
Santa Cruz, CA 95064

Prof. David G. Harkrider
Seismological Laboratory
Division of Geological & Planetary Sciences
California Institute of Technology
Pasadena, CA 91125

Dr. John Foley
NER-Geo Sciences
1100 Crown Colony Drive
Quincy, MA 02169

Prof. Danny Harvey
CIRES
University of Colorado
Boulder, CO 80309

Prof. Donald Forsyth
Department of Geological Sciences
Brown University
Providence, RI 02912

Prof. Donald V. Helmberger
Seismological Laboratory
Division of Geological & Planetary Sciences
California Institute of Technology
Pasadena, CA 91125

Prof. Eugene Herrin
Institute for the Study of Earth and Man
Geophysical Laboratory
Southern Methodist University
Dallas, TX 75275

Prof. Robert B. Herrmann
Department of Earth & Atmospheric Sciences
St. Louis University
St. Louis, MO 63156

Prof. Lane R. Johnson
Seismographic Station
University of California
Berkeley, CA 94720

Prof. Thomas H. Jordan
Department of Earth, Atmospheric &
Planetary Sciences
Massachusetts Institute of Technology
Cambridge, MA 02139

Prof. Alan Kafka
Department of Geology & Geophysics
Boston College
Chestnut Hill, MA 02167

Robert C. Kemerait
ENSCO, Inc.
445 Pineda Court
Melbourne, FL 32940

Dr. Karl Koch
Institute for the Study of Earth and Man
Geophysical Laboratory
Southern Methodist University
Dallas, Tx 75275

Dr. Max Koontz
U.S. Dept. of Energy/DP 5
Forrestal Building
1000 Independence Avenue
Washington, DC 20585

Dr. Richard LaCoss
MIT Lincoln Laboratory, M-200B
P.O. Box 73
Lexington, MA 02173-0073

Dr. Fred K. Lamb
University of Illinois at Urbana-Champaign
Department of Physics
1110 West Green Street
Urbana, IL 61801

Prof. Charles A. Langston
Geosciences Department
403 Deike Building
The Pennsylvania State University
University Park, PA 16802

Jim Lawson, Chief Geophysicist
Oklahoma Geological Survey
Oklahoma Geophysical Observatory
P.O. Box 8
Leonard, OK 74043-0008

Prof. Thorne Lay
Institute of Tectonics
Earth Science Board
University of California, Santa Cruz
Santa Cruz, CA 95064

Dr. William Leith
U.S. Geological Survey
Mail Stop 928
Reston, VA 22092

Mr. James F. Lewkowicz
Phillips Laboratory/GPEH
29 Randolph Road
Hanscom AFB, MA 01731-3010(2 copies)

Mr. Alfred Lieberman
ACDA/VI-OA State Department Building
Room 5726
320-21st Street, NW
Washington, DC 20451

Prof. L. Timothy Long
School of Geophysical Sciences
Georgia Institute of Technology
Atlanta, GA 30332

Dr. Randolph Martin, III
New England Research, Inc.
76 Olcott Drive
White River Junction, VT 05001

Dr. Robert Masse
Denver Federal Building
Box 25046, Mail Stop 967
Denver, CO 80225

Dr. Gary McCartor
Department of Physics
Southern Methodist University
Dallas, TX 75275

Prof. Thomas V. McEvilly
Seismographic Station
University of California
Berkeley, CA 94720

Dr. Art McGarr
U.S. Geological Survey
Mail Stop 977
U.S. Geological Survey
Menlo Park, CA 94025

Dr. Keith L. McLaughlin
S-CUBED
A Division of Maxwell Laboratory
P.O. Box 1620
La Jolla, CA 92038-1620

Stephen Miller & Dr. Alexander Florence
SRI International
333 Ravenswood Avenue
Box AF 116
Menlo Park, CA 94025-3493

Prof. Bernard Minster
IGPP, A-025
Scripps Institute of Oceanography
University of California, San Diego
La Jolla, CA 92093

Prof. Brian J. Mitchell
Department of Earth & Atmospheric Sciences
St. Louis University
St. Louis, MO 63156

Mr. Jack Murphy
S-CUBED
A Division of Maxwell Laboratory
11800 Sunrise Valley Drive, Suite 1212
Reston, VA 22091 (2 Copies)

Dr. Keith K. Nakanishi
Lawrence Livermore National Laboratory
L-025
P.O. Box 808
Livermore, CA 94550

Prof. John A. Orcutt
IGPP, A-025
Scripps Institute of Oceanography
University of California, San Diego
La Jolla, CA 92093

Prof. Jeffrey Park
Kline Geology Laboratory
P.O. Box 6666
New Haven, CT 06511-8130

Dr. Howard Patton
Lawrence Livermore National Laboratory
L-025
P.O. Box 808
Livermore, CA 94550

Dr. Frank Pilotte
HQ AFTAC/TT
1030 South Highway A1A
Patrick AFB, FL 32925-3002

Dr. Jay J. Pulli
Radix Systems, Inc.
201 Perry Parkway
Gaithersburg, MD 20877

Dr. Robert Reinke
ATTN: FCTVTD
Field Command
Defense Nuclear Agency
Kirtland AFB, NM 87115

Prof. Paul G. Richards
Lamont-Doherty Geological Observatory
of Columbia University
Palisades, NY 10964

Mr. Wilmer Rivers
Teledyne Geotech
314 Montgomery Street
Alexandria, VA 22314

Dr. Alan S. Ryall, Jr.
ARPA/NMRO
3701 North Fairfax Drive
Arlington, VA 22203-1714

Dr. Richard Sailor
TASC, Inc.
55 Walkers Brook Drive
Reading, MA 01867

Prof. Charles G. Sammis
Center for Earth Sciences
University of Southern California
University Park
Los Angeles, CA 90089-0741

Prof. Christopher H. Scholz
Lamont-Doherty Geological Observatory
of Columbia University
Palisades, NY 10964

Dr. Susan Schwartz
Institute of Tectonics
1156 High Street
Santa Cruz, CA 95064

Secretary of the Air Force
(SAFRD)
Washington, DC 20330

Office of the Secretary of Defense
DDR&E
Washington, DC 20330

Thomas J. Sereno, Jr.
Science Application Int'l Corp.
10260 Campus Point Drive
San Diego, CA 92121

Dr. Michael Shore
Defense Nuclear Agency/SPSS
6801 Telegraph Road
Alexandria, VA 22310

Dr. Robert Shumway
University of California Davis
Division of Statistics
Davis, CA 95616

Dr. Matthew Sibol
Virginia Tech
Seismological Observatory
4044 Derring Hall
Blacksburg, VA 24061-0420

Prof. David G. Simpson
IRIS, Inc.
1616 North Fort Myer Drive
Suite 1050
Arlington, VA 22209

Donald L. Springer
Lawrence Livermore National Laboratory
L-025
P.O. Box 808
Livermore, CA 94550

Dr. Jeffrey Stevens
S-CUBED
A Division of Maxwell Laboratory
P.O. Box 1620
La Jolla, CA 92038-1620

Lt. Col. Jim Stobie
ATTN: AFOSR/NL
110 Duncan Avenue
Bolling AFB
Washington, DC 20332-0001

Prof. Brian Stump
Institute for the Study of Earth & Man
Geophysical Laboratory
Southern Methodist University
Dallas, TX 75275

Prof. Jeremiah Sullivan
University of Illinois at Urbana-Champaign
Department of Physics
1110 West Green Street
Urbana, IL 61801

Prof. L. Sykes
Lamont-Doherty Geological Observatory
of Columbia University
Palisades, NY 10964

Dr. David Taylor
ENSCO, Inc.
445 Pineda Court
Melbourne, FL 32940

Dr. Steven R. Taylor
Los Alamos National Laboratory
P.O. Box 1663
Mail Stop C335
Los Alamos, NM 87545

Prof. Clifford Thurber
University of Wisconsin-Madison
Department of Geology & Geophysics
1215 West Dayton Street
Madison, WI 53706

Prof. M. Nafi Toksoz
Earth Resources Lab
Massachusetts Institute of Technology
42 Carleton Street
Cambridge, MA 02142

Dr. Larry Turnbull
CIA-OSWR/NED
Washington, DC 20505

Dr. Gregory van der Vink
IRIS, Inc.
1616 North Fort Myer Drive
Suite 1050
Arlington, VA 22209

Dr. Karl Veith
EG&G
5211 Auth Road
Suite 240
Suitland, MD 20746

Prof. Terry C. Wallace
Department of Geosciences
Building #77
University of Arizona
Tuscon, AZ 85721

Dr. Thomas Weaver
Los Alamos National Laboratory
P.O. Box 1663
Mail Stop C335
Los Alamos, NM 87545

Dr. William Wortman
Mission Research Corporation
8560 Cinderbed Road
Suite 700
Newington, VA 22122

Prof. Francis T. Wu
Department of Geological Sciences
State University of New York
at Binghamton
Vestal, NY 13901

ARPA, OASB/Library
3701 North Fairfax Drive
Arlington, VA 22203-1714

HQ DNA
ATTN: Technical Library
Washington, DC 20305

Defense Intelligence Agency
Directorate for Scientific & Technical Intelligence
ATTN: DTIB
Washington, DC 20340-6158

Defense Technical Information Center
Cameron Station
Alexandria, VA 22314 (2 Copies)

TACTEC
Battelle Memorial Institute
505 King Avenue
Columbus, OH 43201 (Final Report)

Phillips Laboratory
ATTN: XPG
29 Randolph Road
Hanscom AFB, MA 01731-3010

Phillips Laboratory
ATTN: GPE
29 Randolph Road
Hanscom AFB, MA 01731-3010

Phillips Laboratory
ATTN: TSML
5 Wright Street
Hanscom AFB, MA 01731-3004

Phillips Laboratory
ATTN: PL/SUL
3550 Aberdeen Ave SE
Kirtland, NM 87117-5776 (2 copies)

Dr. Michel Bouchon
I.R.I.G.M.-B.P. 68
38402 St. Martin D'Heres
Cedex, FRANCE

Dr. Michel Campillo
Observatoire de Grenoble
I.R.I.G.M.-B.P. 53
38041 Grenoble, FRANCE

Dr. Kin Yip Chun
Geophysics Division
Physics Department
University of Toronto
Ontario, CANADA

Prof. Hans-Peter Harjes
Institute for Geophysic
Ruhr University/Bochum
P.O. Box 102148
4630 Bochum 1, GERMANY

Prof. Eystein Husebye
NTNF/NORSAR
P.O. Box 51
N-2007 Kjeller, NORWAY

David Jepsen
Acting Head, Nuclear Monitoring Section
Bureau of Mineral Resources
Geology and Geophysics
G.P.O. Box 378, Canberra, AUSTRALIA

Ms. Eva Johannisson
Senior Research Officer
FOA
S-172 90 Sundbyberg, SWEDEN

Dr. Peter Marshall
Procurement Executive
Ministry of Defense
Blacknest, Brimpton
Reading FG7-FRS, UNITED KINGDOM

Dr. Bernard Massinon, Dr. Pierre Mechler
Societe Radiomana
27 rue Claude Bernard
75005 Paris, FRANCE (2 Copies)

Dr. Svein Mykkeltveit
NTNT/NORSAR
P.O. Box 51
N-2007 Kjeller, NORWAY (3 Copies)

Prof. Keith Priestley
University of Cambridge
Bullard Labs, Dept. of Earth Sciences
Madingley Rise, Madingley Road
Cambridge CB3 0EZ, ENGLAND

Dr. Jorg Schlittenhardt
Federal Institute for Geosciences & Nat'l Res.
Postfach 510153
D-30631 Hannover, GERMANY

Dr. Johannes Schweitzer
Institute of Geophysics
Ruhr University/Bochum
P.O. Box 1102148
4360 Bochum 1, GERMANY

Trust & Verify
VERTIC
Carrara House
20 Embankment Place
London WC2N 6NN, ENGLAND